A PRECISE MEASUREMENT OF THE TOP QUARK MASS IN DILEPTON FINAL STATES USING 9.7 FB^{-1} OF DØ RUN II DATA

Approved by:

Dr. Robert Kehoe

Dr. Pavel Nadolsky

Dr. Stephen Sekula

Dr. David Son

A PRECISE MEASUREMENT OF THE TOP QUARK MASS IN DILEPTON FINAL STATES USING 9.7 FB^{-1} OF DØ RUN II DATA

A Dissertation Presented to the Graduate Faculty of the
Dedman College
Southern Methodist University
in
Partial Fulfillment of the Requirements
for the degree of
Doctor of Philosophy
with a
Major in Experimental Particle Physics
by

Huanzhao Liu

(B.S., University of Science and Technology of China, 2008)

May 16, 2015

Liu , Huanzhao B.S., University of Science and Technology of China, 2008

A Precise Measurement of the Top Quark Mass in Dilepton
Final States Using 9.7 fb^{-1} of DØ Run II data

Advisor: Professor Robert Kehoe
Doctor of Philosophy degree conferred May 16, 2015
Dissertation completed May 6, 2015

The top quark is a very special fundamental particle in the Standard Model (SM) mainly due to its heavy mass. The top quark has extremely short lifetime and decays before hadronization. This reduces the complexity for the measurement of its mass. The top quark couples very strongly to the Higgs boson since the fermion-Higgs Yukawa coupling linearly depends on the fermion's mass. Therefore, the top quark is also heavily involved in Higgs production and related study. A precise measurement of the top quark mass is very important, as it allows for self-consistency check of the SM, and also gives a insight about the stability of our universe in the SM context. This dissertation presents my work on the measurement of the top quark mass in dilepton final states of $t\bar{t}$ events in $p\bar{p}$ collisions at $\sqrt{s} = 1.96$ TeV, using the full DØ Run II data corresponding to an integrated luminosity of 9.7 fb^{-1} at the Fermilab Tevatron. I extracted the top quark mass by reconstructing event kinematics, and integrating over expected neutrino rapidity distributions to obtain solutions over a scanned range of top quark mass hypotheses. The analysis features a comprehensive optimization that I made to minimize the expected statistical uncertainty. I also improve the calibration of jets in dilepton events by using the calibration determined in $t\bar{t} \rightarrow$ lepton+jets events, which reduces the otherwise limiting systematic uncertainty from the jet energy scale. The measured mass is $173.11 \pm 1.34(\text{stat})^{+0.83}_{-0.72}(\text{sys})$ GeV .

TABLE OF CONTENTS

CHAPTER

APPENDIX

LIST OF FIGURES

LIST OF TABLES

Dedicated to my beloved family and friends.

Chapter 1

INTRODUCTION AND THEORY

The understanding of “mass” has seen quite remarkable progress in human and science history, dating all the way from Newton’s enlightenment to Einstein’s revolutionary breakthrough and now the newly authenticated Higgs mechanism. In modern physics, the kinematics and interactions of fundamental particles are successfully described by the Standard Model (SM), which classifies fundamental particles into two categories: gauge bosons, and leptons and quarks. The top quark is the last found in the quark familiy. After its discovery in 1995 [1] [2], the top quark is then involved in the study of the Higgs boson since it is very massive and couples very strongly to the Higgs boson. Since the top quark and the Higgs boson enter the radiative corrections to the W boson mass, improving the precision of the top quark mass and W boson mass was used to help the prediction of the Higgs boson prior to July 2012, and continues to facilitate tests of the SM. The Higgs boson couples to the top quark through a Yukawa coupling that linearly depends on the top quark mass. The indirect determination of this coupling is very close to unity, and hence suggest that the top quark may have special roles in the electroweak symmetry breaking (EWSB). A precise knowledge of the top quark and its mass therefore do not only refines the parameters in the SM, but also serves as a stepping stone to a better understanding of Higgs physics. This chapter describes the SM with an emphasis on the properties of the top quark.

1.1. The Standard Model

The SM was formulated by S.Weinberg (1967) [3] and A.Salam (1969) [4] and has been successful in four decades' experimental tests. The newly discovered Higgs boson (2012) [5] [6] provides one last significant credence to the SM. In the SM, fundamental particles are classified into two categories - fermions and bosons. Fermions are particles with half-integer spins and follow Fermi-Dirac statistics, while bosons have integer spins (including zero spin for the Higgs boson) and follow Bose-Einstein statistics. There are three generations of fermions observed so far (see Fig. 1.1). The first generation includes the electron, electron neutrino, up and down quarks. The other two generations are duplicates of the first generation except the masses are larger in higher generations. In addition, each generation involves different 'flavors' for the fermions. Fermions can also be classified as leptons and quarks. Table 1.1 and 1.2 show the charge, spin and mass of all three generations of quarks and leptons.

There are four known fundamental forces: gravity, electromagnetic, weak and strong interactions. Gravity has not been integrated with the other three forces by a consistent theory. Since its magnitude is $\gg 25$ orders smaller than other forces, gravity is neglected in the SM and does not affect most conclusions in particle physics. The properties of different forces and their carriers are listed in table 1.3.

In SM, the unification of strong, weak and electromagnetic forces is described by the $SU(3)_C \times SU(2)_L \times U(1)_Y$ group theory, where C, L and Y refer to color, weak isospin and hypercharge. The $SU(3)_C$ subgroup describes strong interactions between quarks and gluons. The electroweak interactions are described by the combination of $SU(2)_L \times U(1)_Y$.

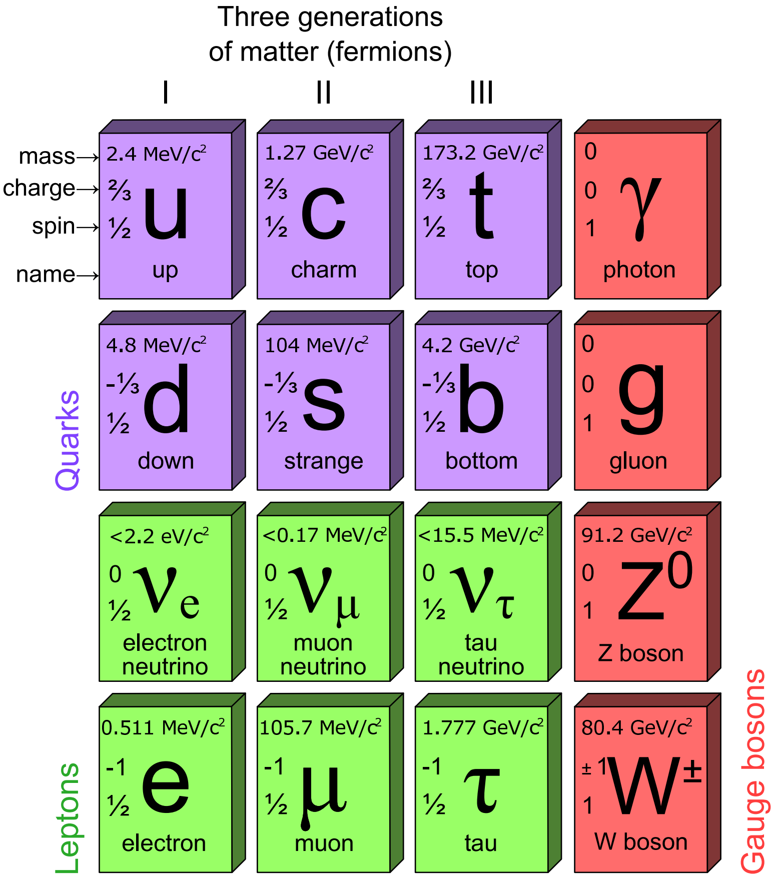

Figure 1.1. Fundamental particles of the Standard Model.

Table 1.1: Three generations of leptons.

Generation	Flavor	Charge (e)	Mass (MeV)	Spin	Lepton number (L_l)	Baryon number (B)
1	e	-1	0.511	1/2	1	0
	ν_e	0	$< 2.2 \times 10^{-6}$	1/2	1	0
2	μ	-1	105.7	1/2	1	0
	ν_μ	0	< 0.17	1/2	1	0
3	τ	-1	1777	1/2	1	0
	ν_τ	0	< 15.5	1/2	1	0

Table 1.2: Three generations of quarks.

Generation	Flavors	Charge (e)	Mass (MeV)	Spin	Lepton number (L_l)	Baryon number (B)
1	u	+2/3	2.3	1/2	0	1/3
	d	-1/3	4.8	1/2	0	1/3
2	c	+2/3	1.3×10^3	1/2	0	1/3
	s	-1/3	95	1/2	0	1/3
3	t	+2/3	173.1×10^3	1/2	0	1/3
	b	-1/3	4.2×10^3	1/2	0	1/3

Table 1.3: Fundamental interactions and gauge bosons.

Interaction	Gauge Boson	Charge (e)	Mass (GeV)	Spin	Range
Strong	Gluon (g)	0	0	1	10^{-15}m
Electromagnetic	Photon (γ)	0	0	1	∞
Weak	$W^{\pm}$	±1	80.4	1	10^{-18}m
	Z^0	0	91.2	1	
Gravity	Graviton (G)	0	0	2	∞

1.1.1. Strong Interaction

The strong interaction is described by Quantum Chromodynamics (QCD). QCD is a $SU(3)_C$-based non-abelian gauge theory [7]. Only color charged particles, namely quarks and gluons, interact via strong force. There are three kinds of color charges: red, green, blue and their corresponding anti-colors. The mediators of strong interactions are eight massless gluons that come from the local gauge invariance under color phase transformation. In QED, photons are massless and the electromagnetic interaction follows inverse square law, resulting in a long range force that decreases while distance increases. However, in QCD the fact that gluons carry color charges leads to gluon self-coupling. If the number of quark flavors does not exceed 16, the strong force is correlated with distance positively and becomes stronger/weaker when distance increases/decreases. Therefore quarks and gluons are bound in color-singlets and can-not appear as free particles. This behavior is called color confinement. We observe two types of color-singlets: baryons and mesons. Baryons are composites of three quarks/antiquarks, and mesons are formed by quark-antiquark pairs. On the other hand, color charged particles become quasi-free while distance decreases. This feature is called asymptotic freedom. The perturbative calculations are only valid for large energy scales which corresponds to small distances. At small energy scale, non-perturbative models are required to fully understand the processes.

1.1.2. Electroweak Interaction

Quantum Electrodynamics (QED) is the first gauge theory formulated for particles and their interactions. QED is based on $U(1)$ and describes the electromagnetic interactions with the photon as the only gauge boson. To formulate the weak interaction, electromagnetic and weak interactions must be unified into the same frame $SU(2)_L \times U(1)_Y$. Photons are massless particles. However the three mediators for the weak interaction are massive gauge bosons, which requires the Higgs mechanism to explain the source of their masses.

In QED, free fermions are described by the Dirac equation. Photons come from the invariance under local gauge transformation of $U(1)$ and are coupled to the electrically charged particles. The QED coupling constant is on the order of 1/137 at very small energy scales and increases very slowly with Q^2, therefore perturbative descriptions can be employed for a very wide energy scale.

The gauge bosons of the weak interactions are electrically charged $W^{\pm}$ and electrically neutral Z bosons. Similar to the fact that the strong interaction is related to color charge and the electromagnetic interaction is related to electric charge, the weak interaction is found to be associated with the chirality of particles and acts on the weak isospin. $W^{\pm}$ and Z bosons can interact with fermions that have a non-zero weak isospin, and they interact with each other. Unlike photons and gluons, $W^{\pm}$ and Z bosons are massive particles (80.4 GeV [8] and 91.2 GeV [9]) with a short lifetime. Therefore, $W^{\pm}$ and Z bosons can only be directly observed through their daughter particles.

Both QCD and QED can be well described by an independent gauge group. However, the weak interaction contradicts with observations if using $SU(2)$ only. The standalone $SU(2)_L$ predicts a third neutral W and requires all gauge bosons to be massless, which are not consistent with observations. To solve this issue, a path is found by unifying the electromagnetic and the weak interactions via the $SU(2)_L \times U(1)_Y$ symmetry group. The gauge invariance in this group leads to four gauge bosons: $W^{1,2,3}$ from $SU(2)_L$ and B from $U(1)_Y$. Photons and Z bosons can be defined as a linear combination of W^3 and B:

$$A = \sin\theta_W W^3 + \cos\theta_W B, \tag{1.1}$$

$$Z = \cos\theta_W W^3 - \sin\theta_W B, \tag{1.2}$$

where θ_W is the weak mixing angle that is determined by the coupling constants g_W of $SU(2)_L$ and g'_W of $U(1)_Y$:

$$\sin\theta_W = \frac{g'_W}{\sqrt{g_W^2 + g'^2_W}}, \tag{1.3}$$

$W^\pm$ are defined by the gauge bosons W^1 and W^2:

$$W^\pm = \frac{1}{\sqrt{2}}(W^1 \mp iW^2). \tag{1.4}$$

1.1.3. Higgs Mechanism

The $SU(2)_L \times U(1)_Y$ symmetry group predicts massless gauge bosons, while $W^\pm$ and Z bosons are observed to be massive. In order to give masses to $W^\pm$ and Z bosons while still keep photon massless, the Higgs mechanism is formulated with spontaneous symmetry breaking.

A complex scalar isospin doublet is introduced:

$$\phi = \begin{pmatrix} \phi^+ \\ \phi^0 \end{pmatrix}, \tag{1.5}$$

where ϕ^+ and ϕ^0 are the charged and neutral scalar. ϕ has a non-zero vacuum expectation value. The Lagrangian L can be expressed as:

$$\mathcal{L} = (D_\mu \phi)^\dagger D^\mu \phi + \mu^2 \phi^\dagger \phi - \lambda(\phi^\dagger \phi)^2, \tag{1.6}$$

where $D_\mu = (\partial_\mu + i\frac{g}{2}\sigma_i W^i_\mu + i\frac{g'}{2}B_\mu)$, and σ_i are the Pauli matrices. The parameters μ and λ satisfy $\mu^2 > 0$, and $\lambda > 0$. L reaches the minimum at the vacuum expectation value v (vev):

$$< \phi >= \frac{v}{\sqrt{2}} = \sqrt{\frac{\mu^2}{2\lambda}}. \tag{1.7}$$

The ground state breaks the $SU(2)_L \times U(1)_Y$ symmetry, making photons massless. After adding a scalar field h to the ground state and inserting it back into Eq. 1.6, the Higgs boson appears as h and EW gauge bosons gain mass terms.

The Higgs mechanism also give masses to fermions through their Yukawa couplings y_f to the Higgs field:

$$m_f = \frac{y_f}{\sqrt{2}} v. \tag{1.8}$$

And the mass of the Higgs boson is determined by an unknown factor λ:

$$M_H = \lambda v. \tag{1.9}$$

Both $m_f(y_f)$ and $M_H(\lambda)$ are free parameters of SM and have to be measured experimentally.

The top quark mass and Higgs boson mass are connected to the W boson mass via radiative corrections [11]:

$$M_W^2 = \frac{\pi\alpha/\sqrt{2}G_F}{\sin^2\theta_W(1-\Delta r)}, \tag{1.10}$$

where Δr is the radiative correction and G_F is the W boson EW coupling [10]. This correction can be expressed as the following for the top quark:

$$(\Delta r)_{top} \approx -\frac{3G_F m_t^2}{8\sqrt{2}\pi^2}\frac{1}{\tan^2\theta_W}, \tag{1.11}$$

and the following for the Higgs boson:

$$(\Delta r)_{Higgs} \approx \frac{3G_F M_W^2}{24\sqrt{2}\pi^2}(ln\frac{M_H^2}{M_Z^2} - \frac{5}{6}). \tag{1.12}$$

1.2. The Top Quark

In 1995, the top quark, which is the last missing memember of the family of quarks in the SM, was discovered by the CDF and DØ experiments at the Tevatron [1] [2], a proton-antiproton collider at Fermilab. The top quark is by far the most massive of all observed fundamental particles in the SM. It has a spin of 1/2 and an electric charge of +2/3 e [12]. The mean lifetime of the top quark is about 10^{-25} s [13], which is approximately 20 times shorter than the timescale of the strong interaction. Therefore, the top quark does not form hadrons but decays immediately after production. This makes the direct observation of a quark possible through detecting the top quark's decay daughters.

1.2.1. The Top Quark Mass

In SM, the masses of the fermions are free parameters that have to be determined through experimental measurements. The 2014 Tevatron combination of the top quark mass measurements [14] is:

$$m_t = 174.34 \pm 0.37(\text{stat}) \pm 0.52(\text{syst})\text{GeV}. \tag{1.13}$$

The heavy mass of top quark is about the same as an atom of tungsten, and it is the only quark mass that is comparable to the EWSB scale. The Yukawa coupling of the top quark to the Higgs boson can be derived inversely from Eq. 1.8. Its value is found to be very close to unity $y_t = 1.0023 \pm 0.0037$. This implies that the top quark may play a special role in the EWSB.

1.2.2. The Top Quark Production

In hadronic collisions, the top quark can be produced in pairs through strong interaction [15] [16], or singly through the electroweak interaction [18]. At the Tevatron, the single top quark production is very weak. The top production is dominated by the $t\bar{t}$ pair production, which is the event topology for the discovery by CDF and DØ in 1995. Figure 1.2 shows the main LO Feynman diagrams for the $t\bar{t}$ pair production through strong interaction. The top left diagram shows the quark-antiquark annihilation. The other three diagrams show the production via gluon-gluon fusion. The LO Feynman diagrams for the single top production are shown in Figure 1.3.

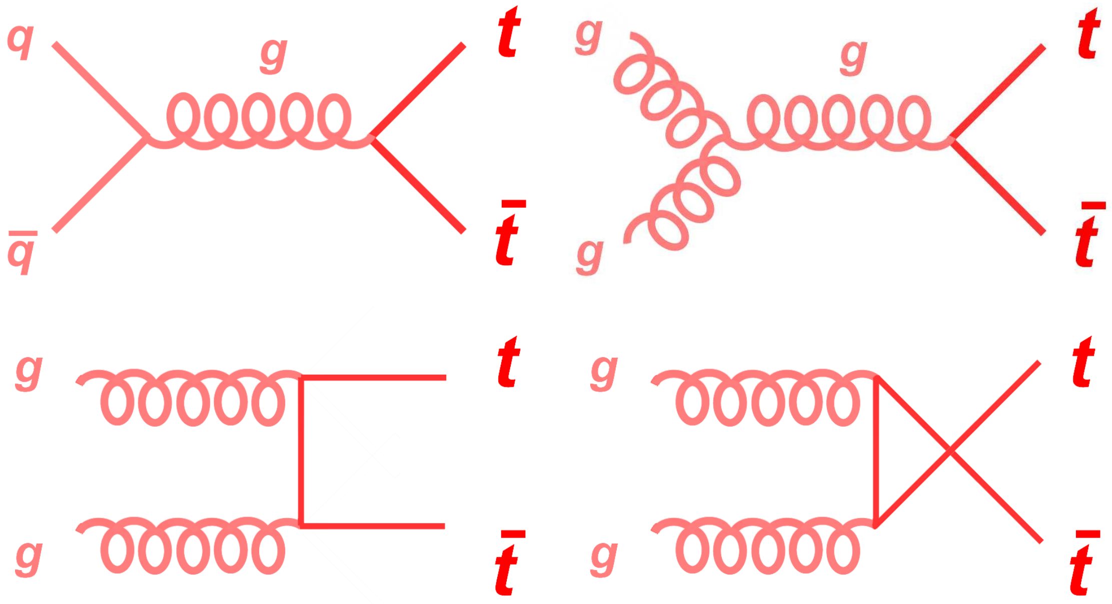

Figure 1.2. Leading order Feynman diagrams for the $t\bar{t}$ pair production: quark-antiquark annihilation (top left), gluon-gluon fusion (top right, bottom).

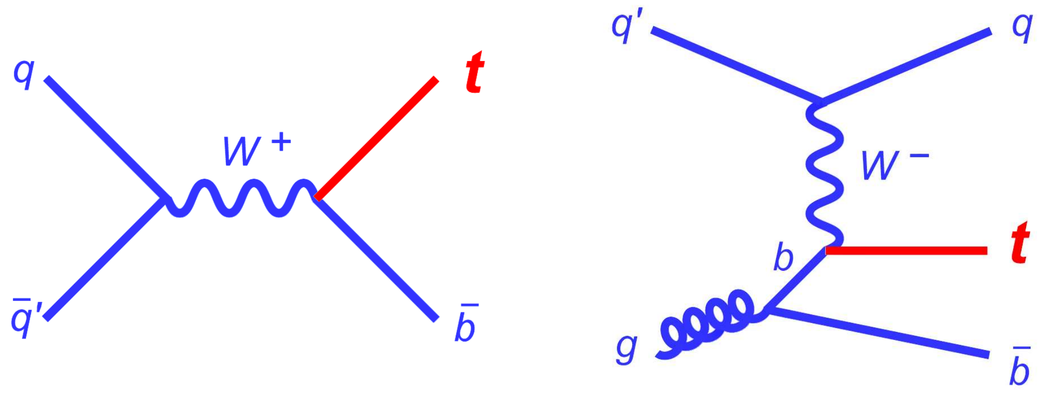

Figure 1.3. Leading order Feynman diagrams for the single top quark: s-channel (left), t-channel (right).

For a different center-of-mass energy, the quark-to-gluon parton-distribution-function (PDF) ratio can be different, which will result in different composition of quark-antiquark annihilation and gluon-gluon fusion. At Tevatron with $\sqrt{s}$ =1.96 GeV, quark-antiquark pair production takes 85% of the $t\bar{t}$ pair production and gluon-gluon fusion is about 15%. At the LHC, production is dominated by gluon-gluon fusion with a proportion of 90% [17].

Single top quark production occurs in the s-channel via virtual W boson decay to the top and bottom quarks, or in the t-channel via exchanging virtual W boson between a light quark and a bottom quark. The first evidence for single top production is reported by DØ in 2006 [18]. The combined cross section was measured to be $\sigma = 4.7 \pm 1.3$ pb [18] with a standard deviation of 3.6 sigma from a cross section of zero. Altough this cross section is just two times smaller than the one for pair production, its background rate is extremely large so that only $t\bar{t}$ pair production has been utilized for the measurement of top quark mass. In this thesis, the top quark mass measurement is performed on $t\bar{t}$ events.

1.2.3. The Top Quark Decay

Due to the large mass, the top quark has a short lifetime and decays immediately after production. In the SM, the top quark is expected to decay to a W boson and a down-type quark (d, s, b) via the electroweak interaction. The decay mode to a W boson and a b quark has a decay rate of 99.8% [19]. Thus the top quark decay is simply dominated by the $t \to W^+b$ process. Hypothesized quarks of a fourth generation do not offset this decay rate as the mass limits on the fourth generation quarks are larger than the top quark mass.

Since W bosons are massive particles and decay through the electroweak interaction, we are not able to observe W bosons in the final states of $t\bar{t}$ decay. A W boson can decay leptonically to a lepton and its corresponding neutrino, or hadronically to $u + \bar{d}$ $(\bar{u} + d)$ or $c + \bar{s}$ $(\bar{c} + s)$. As a result, the $t\bar{t}$ decay channels are defined by the decays of the two W bosons and are classified into three types: all hadronic, ℓ+jets and dilepton. Figure 1.4 shows the branching ratio chart for each $t\bar{t}$ decay channels.

- **all hadronic:** In the all hadronic channel, both W bosons decay to two light quarks with a high branching ratio of 46%. However, this channel suffers from very large QCD multijet backgrounds. Besides, there are four energetic jets in the final states and each jet has a large uncertainty on its reconstructed energy.

- **ℓ+jets:** In the ℓ+jets channel, one W boson decays hadronically to two light quarks while the other one decays leptonically to an electron/muon and its corresponding neutrino. Since τ is also massive and has a short lifetime, the decay to a leptonically decaying τ is also included in this channel. As about 2/3 of the τ decay hadronically, the ℓ+jets channel has an experimental branching ratio of approximately 35%. The signal events in this channel have large statistics with

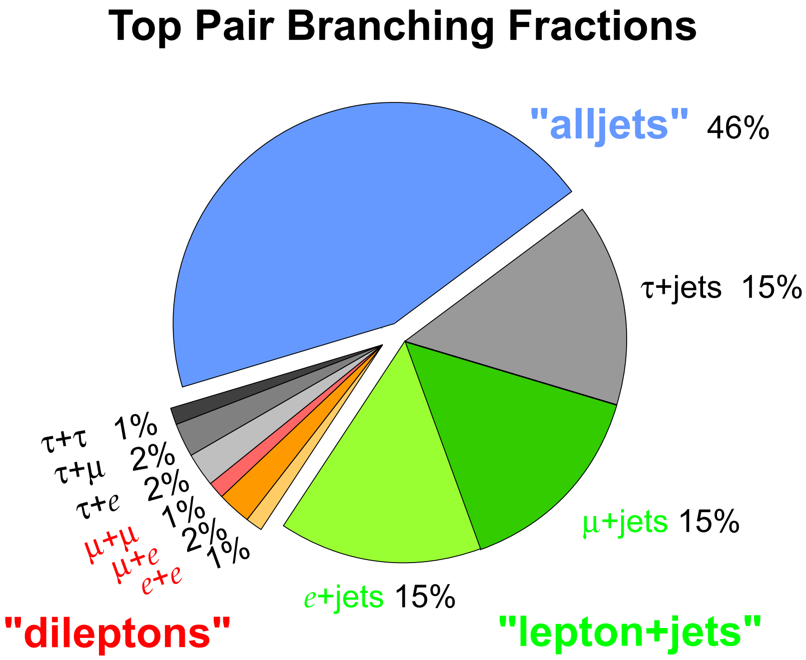

Figure 1.4. The $t\bar{t}$ decay modes and their respective branching ratios.

modest backgrounds mainly from W+jets and QCD multijet backgrounds. The neutrino from one W boson decay can be reconstructed with a quadratic ambiguity. The ℓ+jets channel is involved in the work of this thesis by supplying the absolute energy scale for jets as described in Ch. 5

- **dilepton:** In the dilepton channel, both W bosons decay leptonically to electrons or muons (ee, $e\mu$ and $\mu\mu$) and corresponding neutrinos. The leptonic decay from τ is also included. Although this channel has low branching fractions, there are very limited contamination of backgrounds. Besides, there is one more isolated high energy lepton that is precisely reconstructed than the ℓ+jets channel.

1.2.4. Kinematic Properties of top pair event particles

In dilepton events, the b quarks, leptons and neutrinos all come from the decay of the top and anti-top quarks. Therefore, the energy of these final-state particles is dependent on the mass of the top quark. As shown in Fig. 1.5 using leading jet p_T as an example, for simulated $t\bar{t}$ events with input top quark mass $m_t = 160$, 170, and 180 GeV, the mean of the leading jet p_T distribution is estimated to be 74.62, 80.58 and 85.88 GeV, respectively. This shows that the top quark mass is positively correlated with jet energy with a high sensitivity. In a hadron collider, energy of jets is measured with much larger uncertainty than the electrons and photons, resulting in the fact that lots of jet related analyses have their precision determined by that of the measured jet energy. The general jet energy scale determination at DØ and a specific analysis dependent jet energy calibration are discussed in Chapter 5.

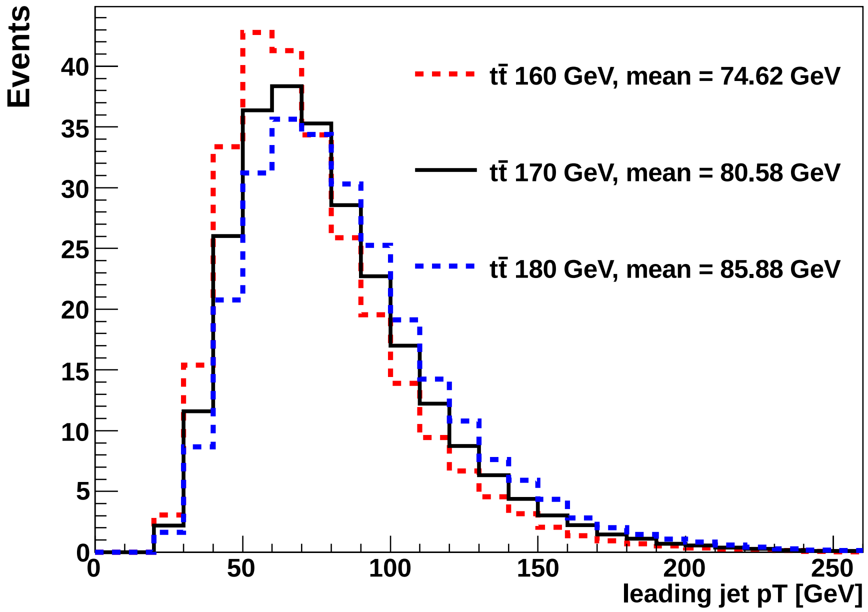

Figure 1.5. Distribution in leading jet p_T for $t\bar{t}$ samples with m_t = 160, 170, and 180 GeV. All samples are normalized to the event number in m_t = 170 GeV.

Chapter 2

EXPERIMENTAL APPARATUS

The analysis presented in this thesis utilizes data collected at the DØ detector located in the Tevatron collision ring. An overview of the Tevatron collider and the DØ detector is given in this chapter.

2.1. The Tevatron Collider

The Tevatron [20] is a circular proton-antiproton collider located at Fermi National Accelerator Laboratory (Fermilab), Batavia, Illinois. Protons and antiprotons are boosted to a center of mass energy of 1.96 TeV and each beam carries about 1 TeV energy circling in the 6.3 km storage ring, hence the accelerator's name. Two multi-purpose detectors, DØ and CDF, are constructed at two collision points to measure outgoing particles from $p\bar{p}$ interactions. Since the start of its operation in 1983, Tevatron has made various remarkable achievements before its shutdown in September, 2011. The first run period of Run II from 2002 to 2006 is called Run II-A, and the second half after upgrades is Run II-B.

Protons and antiprotons go through several stages before interacting within the Tevatron ring as shown in Figure 2.1. In the initial stage, the production of protons and antiprotons are initated from ionizing hydrogen gas into H^- ions in the magnetron chamber [21]. H^- ions are pre-accelerated in the Cockcroft-Walton generator to the energy of 750 keV through static electric field. The pre-accelerated H^- ions are further accelerated to 400 MeV through a series segmented alternating electric fields in the Linac [22], which is a 150-meter-long linear accelerator that consists of

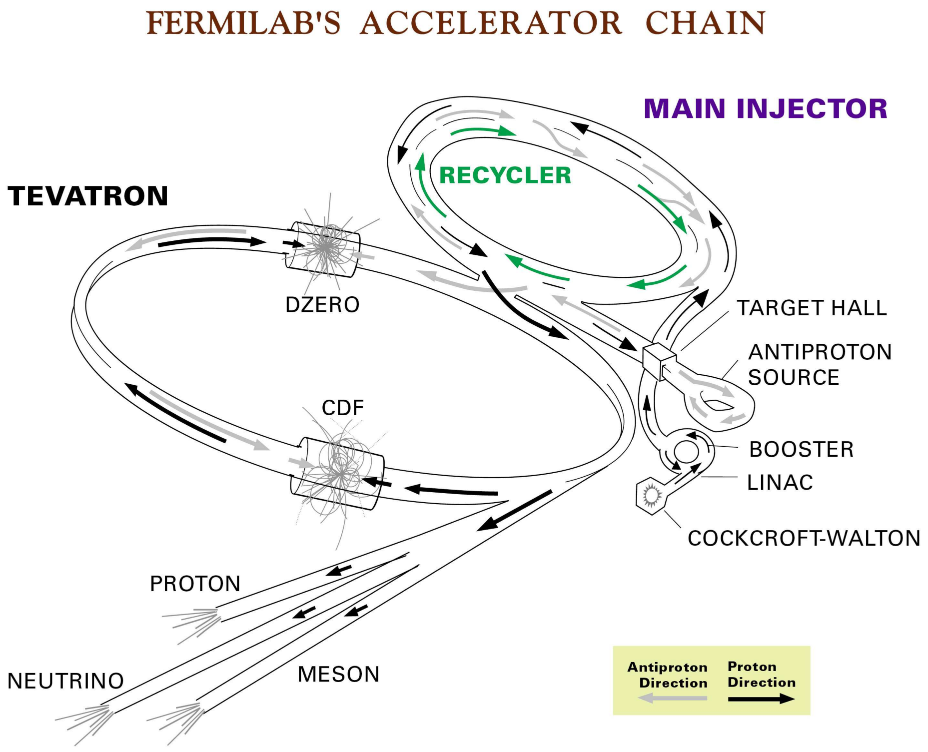

Figure 2.1. The Tevatron Accelerator Chain. DØ and CDF are two multipurpose particle detectors located at the interaction points.

a few sequentially positioned radio-frequency (RF) cavities. The third stage happens at the Booster [23], where H^- ions are filtered with a thin carbon foil to strip off electrons and produce protons (H^+). The Booster Synchrotron, with a 151-meter-long diameter, boosts the incoming protons from the Linac repeatedly in each revolution. The protons will be accelerated to 8 GeV after about 20,000 revolutions and then sent to Main Injector. Main Injector (MI) [24] is the second synchrotron in the accelerator chain that accelerates protons (antiprotons) to 150 GeV. It also delivers 120 GeV protons for target hitting in antiproton production. 120 GeV protons are steered onto a nickel target every 1.47 seconds to produce antiprotons. Many secondary particles are also produced alongside the antiprotons. A Lithium lens is used to remove negative secondary particles and focus the antiprotons into a beam line with velocity spreads of 3% around the average. The beam line is injected into Debuncher [25] to cool down the antiprotons [26], and then into Accumulator [27] to get further cooled and stacked [28]. Once sufficient antiprotons are derived, the beam moves on into the Recycler [29], an 8 GeV storage ring that accumulates the antiprotons from the source and recycles the remaining antiprotons after each Tevatron storage. After being accelerated to 150 GeV in the MI, protons and antiprotons beams are steered into the last and also the largest sychrotron in the accelerator chain, the Tevatron [30]. A series of 240 Niobium-Titanium quadruple magnets narrow down the beams into a small transverse area of $5 \times 10^{-5}\text{cm}^2$ for head-on collisions. Each proton/antiproton beam contains 36 bunches of particles with about 10^{11} protons/antiprotons inside. Both protons and antiprotons are accelerated to 980 GeV within the 2 km diameter Tevatron storage ring in a 4.2 Telsa magnetic field generated by 774 niobium-titanium superconducting dipole magnets. The 2 beams collide every 396 ns with a center-of-mass energy 1.96 TeV.

2.2. DØ Detector

A high-energy $p\bar{p}$ collision involves multiple types of interactions that happen in a very limited time and space; some are well understood and some may not be discovered yet. To comprehend the micro-world, it is essential to seek out interesting events from sea of interactions and measure the final states of collisions as precisely as possible. The DØ detector [31] [32] is a multi-purpose detector built to study high energy $p\bar{p}$ collisions with measurements of electrons, muons, jets, as well as missing transverse energy. The DØ detector is about 20 meters in length and 13 meters in height, and it weighs 5,500 tons. The 3 major physical components of the detector are the central tracking system, uranium/liquid-argon calorimeters and a muon spectrometer, which will be overviewed in the following subsections. After the successful discovery of top quark during its first run at a center-of-mass energy of 1.8 TeV (Run I, 1992 - 1996), the DØ detecter passed through a series of upgrades and raised the center-of-mass energy to 1.96 TeV, aiming for the search of the Higgs boson and precise measurements of fundamental electroweak parameters (Run IIa, 2001 - 2006; Run IIb 2006 - 2011). A schematic view of the DØ detector is shown in Figure 2.2.

2.2.1. Coordinate System

The DØ detector employs a right-handed Cartesian coordinate system. The z-axis points out of the geometric center of the detector into the direction of the proton beam. The x-axis points toward the center of the Tevatron ring and y-axis vertically upward. In practical use, cylindrical coordinate system (ρ, ϕ, z) and spherical coordinate (r, θ, ϕ) system are more often used. Generally, it is more covenient to use

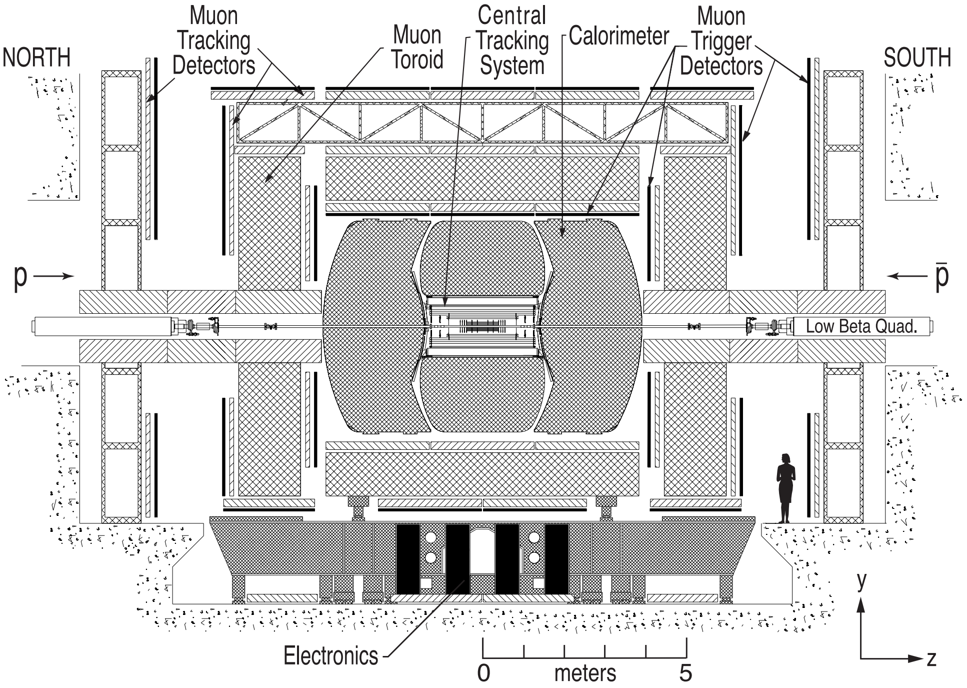

Figure 2.2. Schematic view of the DØ detector.

pseudo-rapidity η instead of azimuthal angle θ directly,

$$\eta = -\ln\left(\tan\frac{\theta}{2}\right), \tag{2.1}$$

where for massless particles η is equivalent to rapidity,

$$y = \frac{1}{2}\ln\left(\frac{E + p_z}{E - p_z}\right). \tag{2.2}$$

The $p/\bar{p}$ beam has a distribution along the beam line which shifts the collision vertex by as much as 30 cm at DØ. Therefore, two definitions of $\eta's$ are required to describe the position of particles accordingly. The η with respect to the event reconstructed vertex is denoted as η_{phys} (or simply η) where the subscript "phys" refers to corresponding physical objects. The detector η (η_{det}) is defined as the rapidity originating from the geometric center of the detector.

2.2.2. Tracking System

The momentum, electric charge and vertex origin of an outgoing charged particle are first detected and measured according to its curved trajectory in the central tracking system. DØ central tracking instruments are comprised of 3 components: a Silicon Microstrip Tracker (SMT), a Central Fiber Tracker (CFT) and a surrounding solenoidal magnet [33]. The magnet is 2.73 m in length and 1.42 m in diameter. It submergs the whole trackers in a homogeneous, 2 T magnetic field. It is cooled with liquid helium to maintain superconductivity at an operating current of 4749 A. The thickness of the magnet is designed to be about 1 radiation length to balance optimal momentum resolution with tracking pattern recognition. The SMT and CFT are able to locate the primary vertex with about 35 μm resolution along the beam line and help identifying jets originated from b quarks. Figure 2.3 shows the schematic view of the DØ central tracking system.

2.2.2.1. Silicon Microstrip Tracker (SMT)

Located in the innermost region of the detector and nearest to the collision point, the Silicon Microstrip Tracker (SMT) operates in tracking and reconstruction of the primary vertex and secondary vertex with high precision. The distribution of particles within each bunch results in a 60 cm long parallel interaction region along the beam line. As for the need to measure tracks perpenticular to the detector surface for full angle, the SMT consists of 6 barrels and 12 F-disks in the central region and 4 H-disks in forward regions, all deployed concentric along the beam pipe. The interspersed barrel modules concentrate on the measurements of $r - \phi$ coordinates and the third dimension z is provided by the disk detectors alongside $r - \phi$. Each

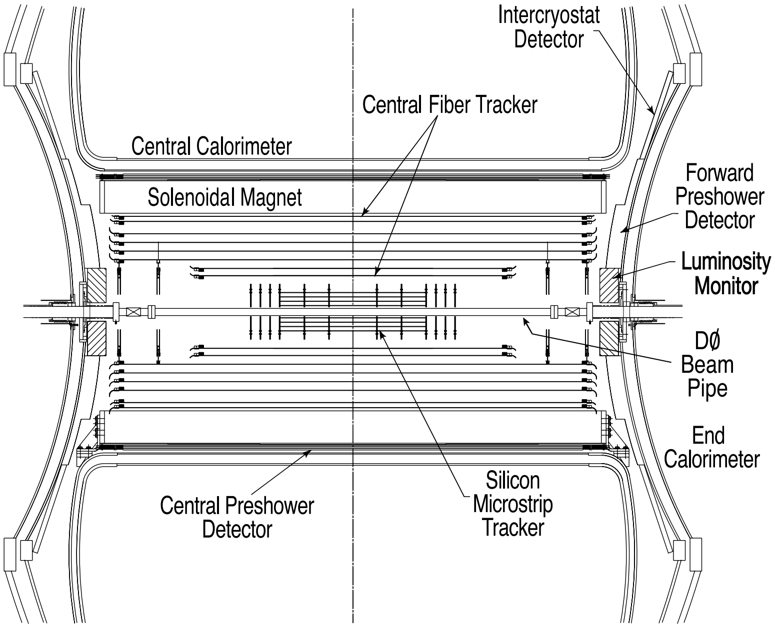

Figure 2.3. Schematic view of the DØ central tracking system.

barrel is composed of 4 silicon readout layers. The first and second layers contain 12 silicon modules while the third and fourth contain 24. The F-disks consist of 12 double-sided wedge-detectors and in the forward region the H-disks are consisted of 24 pairs of back-to-back single-sided wedges. The central coverage is provided by barrel detectors and F-disk detectors, as well as CFT; the large angle is mostly covered up to $|\eta| = 3$ by the H-disk detectors. The schematic view of SMT is shown in Figure 2.4.

2.2.2.2. Central Fiber Tracker (CFT)

Residing between the SMT and solenoid is the Central Fiber Tracker (CFT) with various radii from 20 to 52 cm. It contains 76800 scintillating fibers mounted on 8 concentric fiber cylinders and covers the pseudo-rapidity up to $|\eta| = 1.7$. The

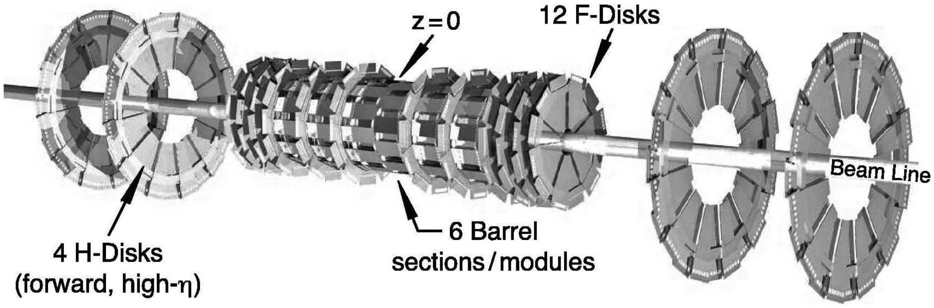

Figure 2.4. Schematic view of the DØ Silicon Microstrip Tracker.

innermost two cylinders are 1.66 m long and the outer six are 2.52 m long. Each cylinder consists of double layers of fibers in the axial direction and a doublet layer of fibers with a stereo angle ϕ oriented at $+3°$ for odd-numbered layers (1,3,5,7) and $-3°$ for even-numbered layers (2,4,6,8). The schematic view of CFT is shown in Figure 2.5. Both of the $r - \phi$ and $r - z$ coordinates are measured in the CFT with a resolution of about 100 μm, or 2×10^{-4} in ϕ and 1 cm in z direction. When charged particles passes through, the scintillating light travels within the 835 μm thick fiber in both directions to the ends. On one side, the fiber end is coated with an aluminum mirror to reflect the light back; on the other end, the light is conducted into a wavelength shifting waveguide and transmitted to Visible Light Photon Counter (VLPC) where light signals are converted into electric signals and read out. The aluminum mirror has a reflection efficiency about 90%.

2.2.3. Preshowering System

The preshowering system is a level between Tracking and Calorimetry systems that features a Central Preshower Detector (CPS) and two Forward Preshowering Detectors covering $|\eta_{det}| < 1.3$ and $1.5 < |\eta_{det}| < 2.5$ pseudo-rapidity ranges respectively.

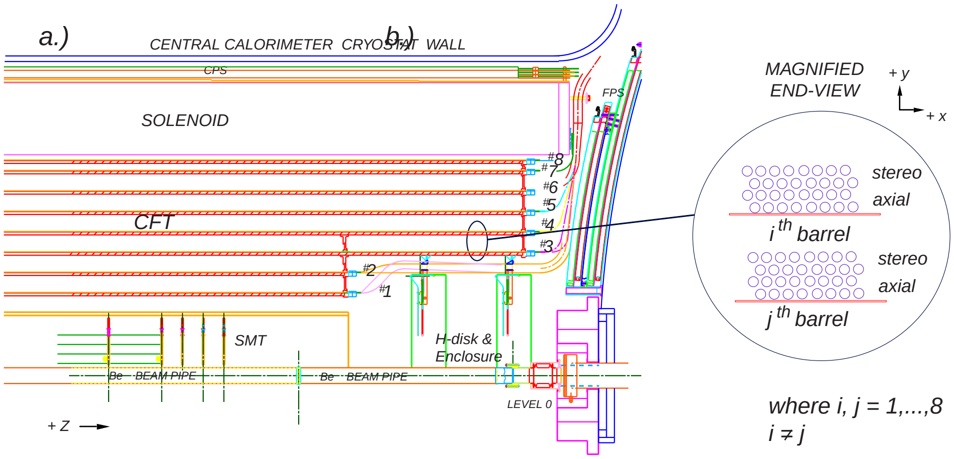

Figure 2.5. Schematic view of the DØ Central Fiber Tracker.

It is built to improve the electron and photon identification as well as background rejection during both online and offline reconstruction. The fast energy sampling of the particles before entering calorimeter and position measuring capability make the preshowering system aid in both the calorimetry system and tracking system.

Both CPS and FPS are constructed of triangular scintillator strips. In the center of each strip, a wavelength-shifting fiber is embedded to collect and carry scintillation light to the end of the detector. The light is then transmitted to an attached VLPC for readout. As shown in Figure 2.6, the CPS consists of three layers of triangular scintillator strips and each layer is comprised of 1280 strips. The innermost layer is axial while the other two layers are positioned at stereo angles of +24° and −24° to the innermost layer. The two FPSs are mounted on the surfaces of the south and north calorimeter cryostats. Each of them consists of two layers of scintillators, and a 11 mm ($2X_0$) thick lead-stainless-steel absorber is plugged in between the two FPSs. The innermost scintillator layer of each FPS (closer to the collision point), which covers a pseudo-rapidity range of $1.65 < |\eta_{det}| < 2.5$ together with the absorber, detects particles through ionization and is therefore called *minimum ionization particle* (MIP) layer. The outermost layer covers $1.5 < |\eta_{det}| < 2.5$ and is named as *showering layer* based on its EM shower detecting function. In the MIP layer, passing charged particles leave minimum ionization for position measurements. Hadronic particles do not necessarily shower in the absorber but will generate a secondary MIP signal once it is electrically charged.

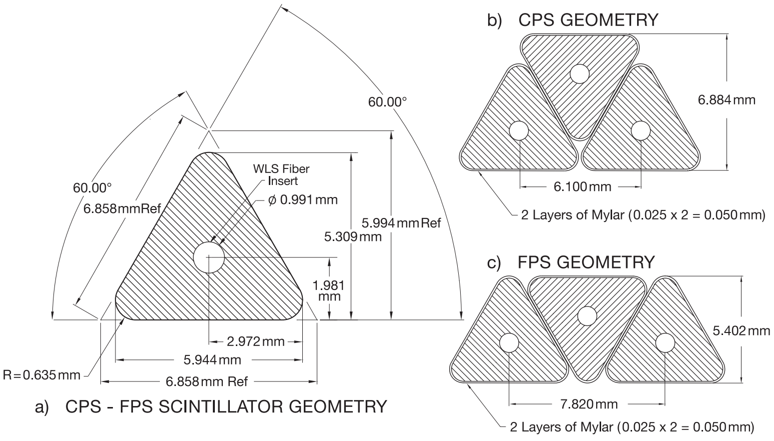

Figure 2.6. Cross section view of the CPS and FPS scintillator strips.

2.2.4. Luminosity System

Two luminosity moniters (LM) are installed at $z = +140$ cm and $z = -140$ cm along the beam pipe, as shown in Figure 2.7, to measure the Tevatron luminosity from inelastic $p\bar{p}$ collisions. They also serve to measure the beam halo rates and the z coordinate of the interaction vertex. Each of the LM detectors consists of two arrays of 24 plastic scintillation counters with Photomultiplier Tube (PMT) readout. Each counter is 15 cm in length and covers the range $2.7 < |\eta_{det}| < 4.4$. The timing resolution of the scintillators is around 0.3 ns, which provides capability in discriminating particles from the interaction region and the beam halos.

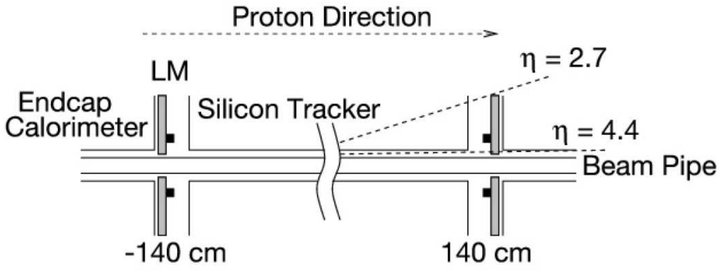

Figure 2.7. Location of the luminosity monitors on the z-axis.

2.2.5. Calorimetry System

2.2.5.1. Uranium/Liquid-Argon Calorimeter

The DØ calorimeter is located outside of the tracking system and is designed to measure the energy of electrons, photons and jets, as well as determination of event missing transverse momentum ($\not{E}_T$). It also aids in identification of electrons, muons, photons and jets. As shown in Figure 2.8, the calorimeter is mainly comprised of three pieces: a barrel-shaped central calorimeter (CC) covers the pseudo-rapidity range $|\eta_{det}| < 1.1$; two end calorimeters (EC) cap the CC on the south (ECS) side and north (ECN) side and extends the coverage to $|\eta_{det}| \approx 4.5$. Each CC and EC container is filled with liquid-argon (LAr) as active medium and is built-in with two different layers of segmented absorber plates. The innermost is four electromagnetic absorber layers (EM), sequentially followed by 3∼4 fine (FH) and 1∼3 coarse hadronic (CH) layers, respectively. The enviroment temperature is maintained at 90K by surrounding cryostats to keep argon in the liquid phase. The segmentation pattern of the calorimeter is shown in Figure 2.9.

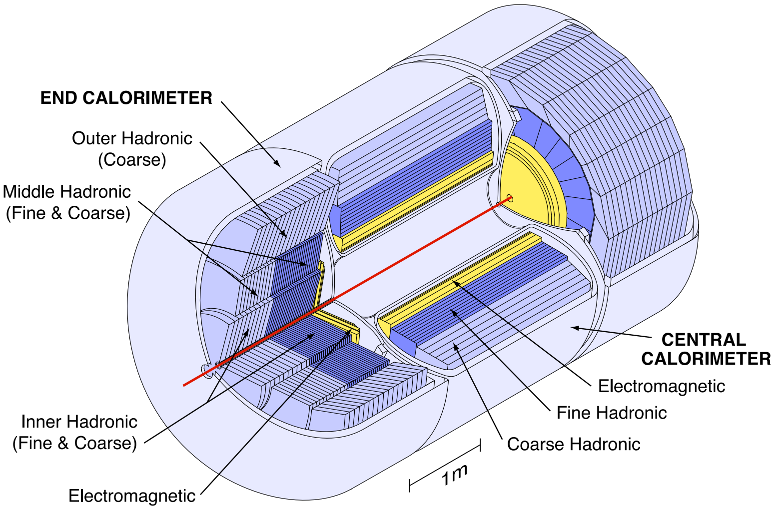

Figure 2.8. Schematic view of the DØ Liquid Argon Calorimeter.

The absorber layers in the EM and FH/CH are all geometrically and materially different: the EM thin plates are 3 mm thick in CC and 4 mm thick in the ECs, all made from nearly pure depleted Uranium; The FH layer uses 6 mm thick Uranium-Niobium alloy plates while CH layer uses thick (46.5 mm) copper plates in the CC and stainless steel plates in the EC. All three calorimeter components are segmented radially as towers from inside out. The segmentation in $\eta - \phi$ space for the first, second and fourth layer of the EM and both of FH and CH is $\Delta\eta \times \Delta\phi = 0.1 \times 0.1$. The third layer of the EM is designed to be closest to the shower development maximum for absorbtion of all electromagnetic particles and is therefore doubled in η and ϕ granularity for more precise measurement of EM shower position. Due to aging of the calorimeter, this shower development maximum has shifted in Run II. The

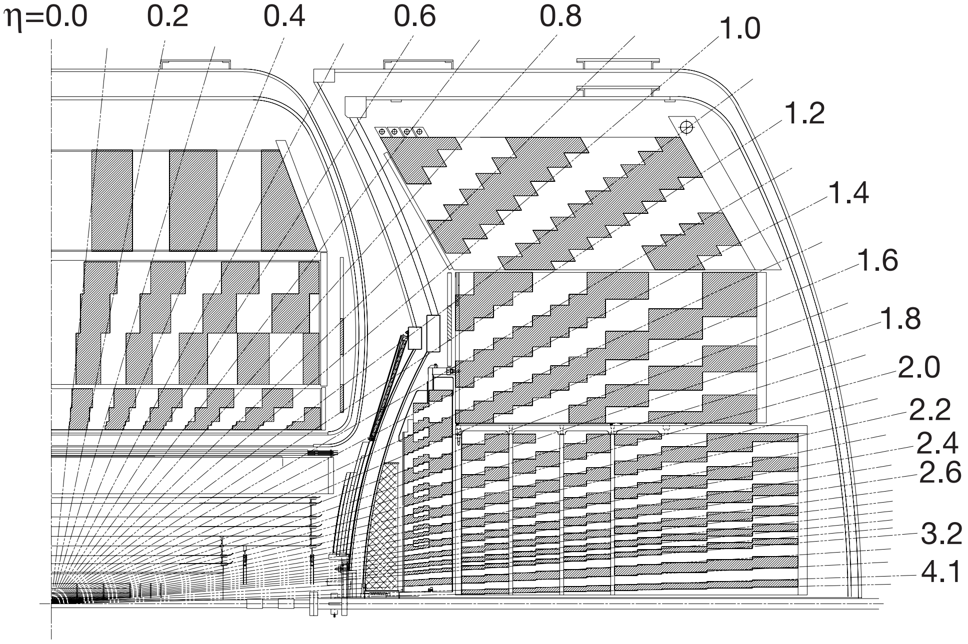

Figure 2.9. Schematic view of the DØ detector with transverse and longitudinal segmentation pattern.

fact that hadronic jets shower less (60%) in the EM calorimeter and primarily in the hadronic calorimeter is very useful in distinguishing electromagnetic objects and hadronic objects as EM showers never reach the hadronic layer, in addition to the EM and hadronic shower shapes.

Each calorimeter cell is filled with liquid-argon and interiorly arrayed with absorber plates and read-out coppers pads. Passing-through charged particles deposit energy in the abosorber plates through ionization and bremsstrahlung, ionizing liquid-argon atoms. A 2 kV homogeneous electric field drifts ionized electrons to copper pads and read out charges proportional to the deposited energy. The typical electron drift time is about 450 ns. This inevitably causes energy pile-up since collision of proton and antiproton beams occurs every 396 ns so Tevatron runs with a 50ns shorter bunch crossing time. This issue is regulated by a baseline subtraction in the readout and removing signal from previous crossings. A typical calorimeter cell of the U/LAr is shown in Figure 2.10.

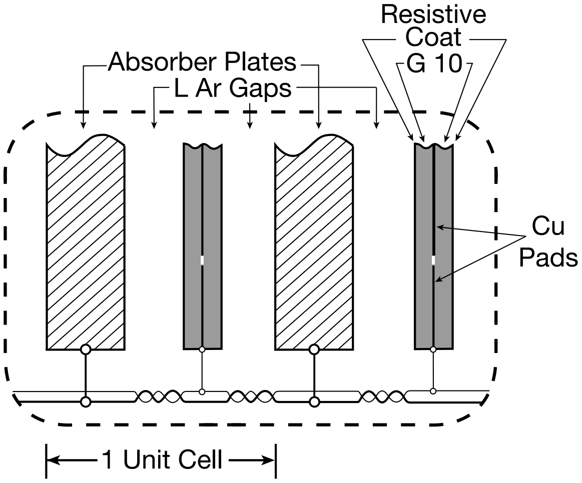

Figure 2.10. Schematic view of the Liquid-Argon cell of the calorimeter.

2.2.5.2. Inter-Cryostat Detector (ICD)

The incomplete pseudo-rapidity coverage of the three independent calorimeters and substantial unsampled materials in the region $0.8 < |\eta_{det}| < 1.4$ degrades the energy resolution. To address the issue, the Inter-cryostat detector (ICD) is mounted on the exterior surface of the ECs. The ICD covers $1.1 < |\eta_{det}| < 1.4$ and is made of small scintillating tiles, each of which provides the same coverage as the calorimeter cells, $\Delta\eta \times \Delta\phi \approx 0.1 \times 0.1$. Readout cells called massless gaps (MG) are also added inside the CC and EC cryostats to supply information lost due to unsamples materials.

2.2.6. Muon System

The bremsstrahlung probablity goes as squared mass of the incident particle, so muons can escape calorimeters with only a little energy deposited due to their comparatively larger mass than electrons. To identify and measure muons properly, the muon system is built surrounding the calorimeter as the outermost part of the detector. The whole muon system can be divided into two components: the *central muon system* or the Wide Angle MUon System (WAMUS) and the Forward Muon System (FAMUS). WAMUS covers the central region up to $|\eta| = 1$, and FAMUS extends the coverage to $|\eta| = 2$. Both WAMUS and FAMUS consist of A, B and C three layers. The A layer is right around the calorimeter and surrounded by 1.8 T toroidal magnets, then B layer and C layer follows and finishes the lineup. The toroidal magnet is installed to bend muons and provide an independent measurement of muon momentum. This helps with better matching of muons with CFT tracks, allowing low p_T cutoffs in Level 1 muon trigger, better π and K rejection and momentum resolution improvements to high-momentum muons.

All three layers in the muon system are comprised of drift tubes and scintillation counters. The WAMUS employs Proportional Drift Tube (PDTs) while Mini Drift Tubes (MDTs) are used in FAMUS. The PDT layers are shown in Figure 2.11. The central drift tubes is typically constructed to be 2.8×5.6 m^2 out of Aluminium tube. Each of the PDTs contains three decks of drift cells except the top A layer which has four. Each drift cell is 10.1 cm long and 5.5 cm wide and groups in 24 for every single deck in a staight array. The MDTs consist of four decks of cells in A layer and three decks in B and C layer. Each MDT cell is 9.4 mm by 9.4 mm in dimension. These drift tubes particularly function in recording of electron drifting time and signal arrival time from hit cell to readout, as well as charge deposition.

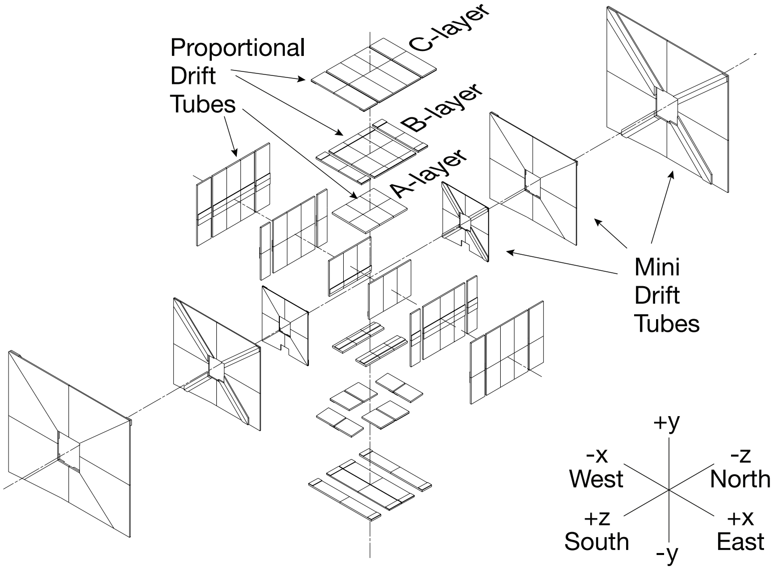

Figure 2.11. Schematic view of the muon wire chambers.

Precise timing is important in muon triggering, identification and trajectory reconstruction. To acquire these with precision, several layers of scintillation counters are installed into the muon system. Located on the top, sides and bottom of the PDTs in C layer are Cosmic Caps [34] [35] and Cosmic Bottom Counters. These counters are operated with fast timing signals to discriminate muons generated from $p\bar{p}$ collisions against cosmic rays. Another kind of counter in WAMUS is the $A\phi$ scintillation counter which is in the A layer of central muon system. Primarily, $A\phi$ counters match the tracks detected in CFT with a timing resolution of 2 ns. In the forward muon system, trigger scintillation counters are installed on each of the layer. All these counters provide good time resolution and help locate muon positions with high precision, particularly in the ϕ coordinates. The layers of the scintillators are schematically shown in Figure 2.12.

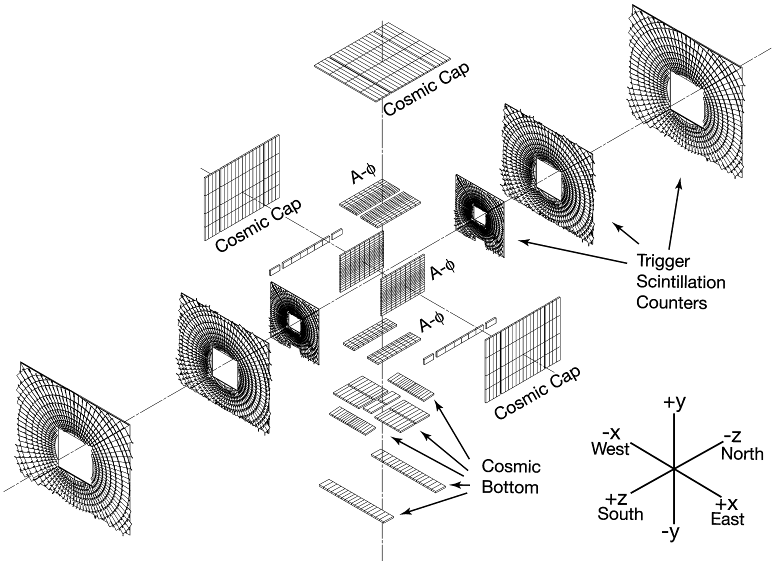

Figure 2.12. Schematic view of the muon scintillation detectors.

2.2.7. Trigger System

Collision of proton and antiproton beams occurs every 396 ns at each collision point, generating $p\bar{p}$ events with a rate of 2.5 million per second. Most of the events are of less interest for physical analyse and has to be picked off consequently. Additionally, the physical limit on storage space and the processing rate of electronical systems demand a fast and efficient event filtering system. The triggering framework is therefore designed and installed per the request. The DØ trigger system consists of three sequential levels and each following level explores events with more detailed patterns and sophisticated algorithms. The first in the chain is Level 1 (L1) trigger which is comprised of pure hardware with an accept rate of 2 kHz. L1 utilizes electronic signals from multiple detectors to execute initial selection of events. Level 2 (L2) trigger is a mixture of hardware and software that use individual reconstructed objects and their correlations for trigger decisions. L2 provides an accept rate of 1kHz. Events passed L1 and L2 are sent to the pure software based Level 3 (L3) trigger for final decision making. The L3 accept rate is reduced to 50 Hz due to sophisticated algorithms. The software package COOR is installed on an online host to coordinate and control DØ triggering. An overview of the DØ trigger and data acquisition system can be seen in Figure 2.13.

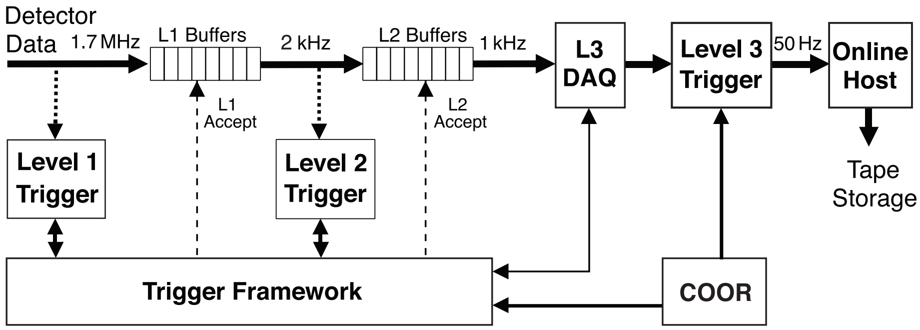

Figure 2.13. Overview of the DØ trigger and data acquisition systems.

2.2.7.1. *Level 1 trigger*

As the first stage, L1 trigger faces a pool of numerous events and needs to make very fast decisions for each bunch crossing. It consists of calorimeter trigger (L1Cal), central track trigger (L1CTT), muon system trigger (L1Muon) and forward proton detector trigger (L1FPD). The Level 1 trigger framework coordinates timing of L1 detector triggers. Each subsystem looks at their detector readout and sets detector-specific trigger terms, e.g. electrons, photons, jets and $\not{E}_{\mathrm{T}}$, for L1Cal. These terms are taken up by the trigger framework to make trigger decisions. Accepted events are passed on to L2.

The L1Cal triggers on events that pass through preset transverse momentum threshold using fast readout of energy depositions in the calorimeter towers. Events with high-pT electrons, photons, jets, taus decaying into hadrons, as well as events with large imbalance of momentum are triggered. The L1CTT makes use of the scintillators in the CFT and the preshower detectors to make fast track reconstruction and momentum estimation. The L1Muon searches for predefined patterns of hits consistent with central detector muons using hits from muon wire chambers, muon scintillation counters and L1CTT tracks. Cosmic muons are rejected by the trigger if they are identified as not originating from the center of the detector or they do not match the time difference between the beam crossing and muon tracking. The L1 trigger decision time is $3.5\mu s$ or less.

2.2.7.2. Level 2 trigger

The L2 trigger system consists of two stages: the preprocessor (hardware) stage and the global (software) stage. The preprocessor stage includes the Level 2 calorimeter trigger (L2Cal), the preshower detector trigger (L2PS), the muon system trigger (L2Muon), the SMT trigger (L2STT) and the Level 2 central track trigger (L2CTT). In this stage, the L2 preprocessors collect information from the front-ends and L1 trigger system to analyze and form physics objects. L2Cal construct primitive electrons, photons and jets with clustering algorithms. Event missing transverse momentum ($\not{E}_T$) is also determined based on the imbalance of trigger tower energies. L1CTT tracks are further processed in L2CTT using the transverse momentum. The L2Muon imports L1Muon candidates to improve muon quality using timing data. In the global stage, a global processor (L2Global) selects events based on the identified objects formed in previous stage and certain selectrion criteria to make a decision.

2.2.7.3. Level 3 trigger

The L3 trigger is a fully programmable software based trigger system running in a farm of parallel computers to further select L2 events based on the reconstructed physics objects and their correlation. The L2 objects receive a more sophisticated reconstruction and more complicated algorithms are applied for event filtering. This results in the data rate reducing from 1 kHz to 50 Hz which synchronize with the pace of tap recording. The objects passing L3 trigger get quality in their definition and reconstruction and is finally recorded on the tape for offline analysis.

Chapter 3

DATA SAMPLE AND SIMULATION

The measurement of the top quark mass utilizes both data and simulated $t\bar{t}$ and background events at DØ. For data sample, several requirements are needed to be fulfilled to ensure data quality. Monte Carlo (MC) simulation is indispensible to link theory to observations. For better comparability to data, MC events have to be integrated with a detector simulation. This chapter mainly describes the above techniques as well as data and Monte Carlo samples.

3.1. Data Sample

The data sample used for this analysis is the full Run II data set that was collected from April 2002 to February 2006 (Run II-A) and June 2006 to September 2011 (Run II-B) with integrated luminosity of 10.6 fb^{-1} (see Fig. 3.1). At DØ a reconstruction software called D0reco [36] [37] is employed to analyze tracker hits, energy depostion and trigger information as discussed in chapter 4.

3.1.1. Data Quality

In the data taking process, data quality can be severely jeopardized by any subsystem compromise. To ensure the quality of collected data, a set of criteria is designed to monitor and identify instrumental issues occured during the subsystem operation. Timewise, the data taking procedure can be separated into fundamental units called *luminosity blocks* which usually last for a few minutes. The instantaneous luminosity in the block is assumed to be equal to the average luminosity of that period. The cal-

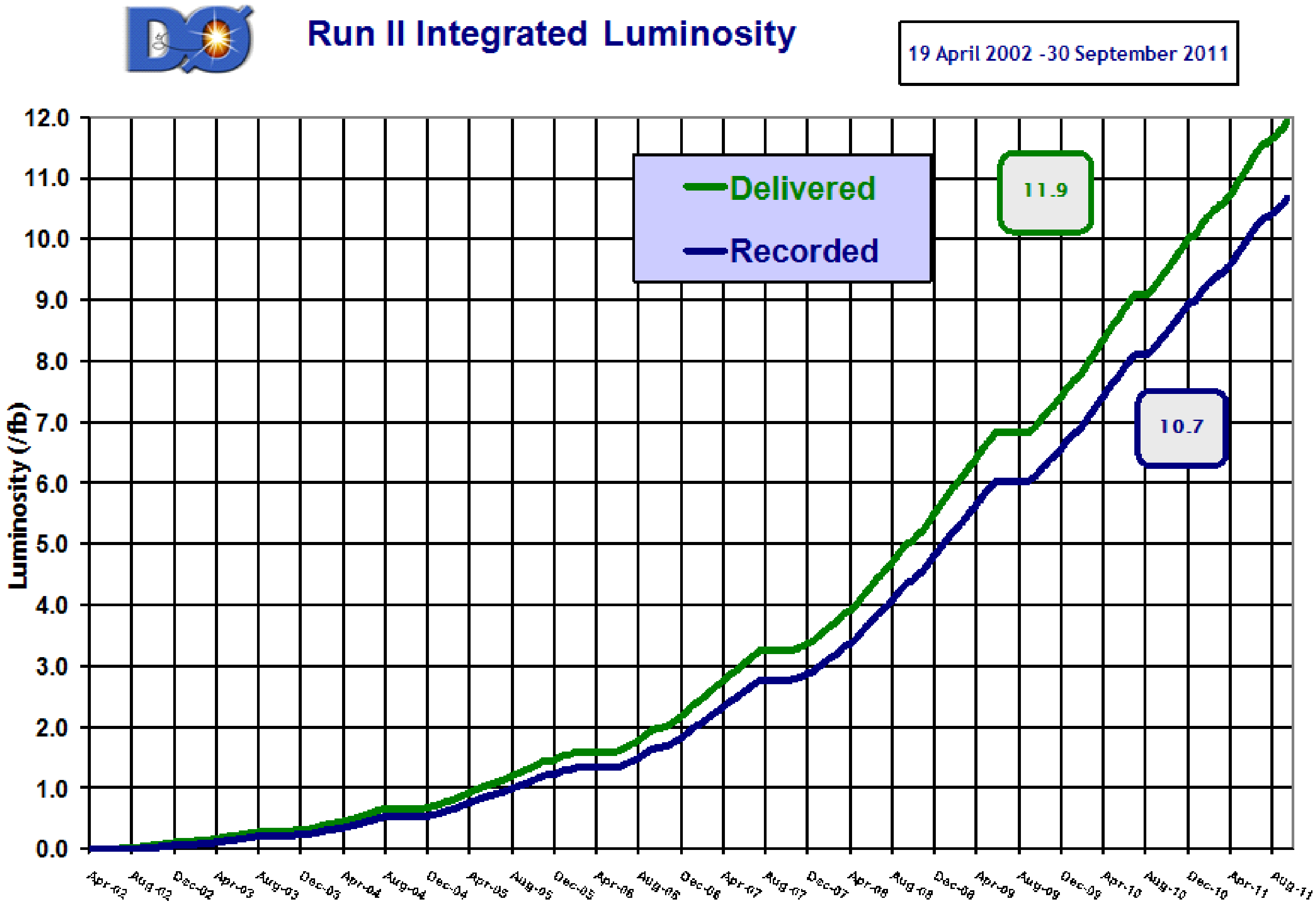

Figure 3.1. The Run II integrated luminosity from April 2002 to September 2011.

culation of total integrated luminosity is done by summing up all qualified luminosity blocks that pass data quality requirements.

A luminosity block or even a whole run will be considered to be *bad* and abandoned if any subdetector system is found to be malfunctioning. For example, inadequate operation of the calorimeter may cause abnormally large signal outputs in certain cells or the entire tower of calorimeter cells. On the other hand, a signal may not even be registered if calorimeter calibration is not properly done, e.g. incorrect pedestal subtraction. Therefore, as the first stage of data quality control, the online data quality monitoring is of significant importance. Besides the online data quality monitoring process, offline data quality reprocessing is also enabled by recording the status of all detector subsystems into each of the luminosity blocks and stored in the *Offline Run Quality Database*. All qualified runs must be assured to be free of *bad* subsystems.

Based on the triggers required for the analysis a list of bad luminosity blocks is generated. Luminosity blocks are segmented periods of time for data recording, which usually last for about 2 mins. Luminosity blocks can be declared as bad if, for example, the average missing transverse energy in a series of luminosity blocks is significantly different from zero. All bad blocks will be finally abandoned as a result.

Single event disposal will be executed for calorimeter noise patterns. For example, an energy calorimeter ring in ϕ indicates electronic problems like grounding issues etc. Events removed from an event-by-event basis pattern will not be able to be excluded from the luminosity calculation. Therefore a data quality efficiency correction should be applied to the Monte Carlo events in this case.

3.1.2. Triggers Requirements

For the dilepton final state analyses, channel dependent trigger requirement [38] [39] needs to be fulfilled to pick out dilepton events. For the *ee* channel, events are required to pass single electron "OR" triggers, where an EM calorimeter tower needs be above a certain E_T threshold at L1 and has to match with the hits in the tracking system. In the $\mu\mu$ channel, events needs to pass single muon "OR" triggers, where a track has to be matched at L1. Track isolation and tight wire conditions are required at the highest luminosity. The efficiencies of single ee and $\mu\mu$ triggers are measured with $Z \to ee$ and $Z \to \mu\mu$ events, respectively. The efficiency calculation uses a method called *tag-and-probe*. One lepton is required to pass L1 single electron triggers and chosen as tag. The second lepton is probe without any trigger requirement and is considered an unbiased object for efficiency calculation. The total trigger efficiency is estimated to be ~99% for the ee channel and ~80% for $\mu\mu$. In the $e\mu$ channel, no explicit trigger requirement is applied to maximize the trigger efficiency, which is nearly 100%. In MC, the ee and $\mu\mu$ events are weighted according to the calculated trigger efficiency measured in data, and we assume an efficiency of 100% for the $e\mu$ events.

3.1.3. Final Data Sample

The luminosity for each run period after data quality control is shown in Table 3.1. The calculation of the luminosity use the luminosity database with an unprescaled trigger. The systematic uncertainty associtated is 4.3%.

Table 3.1: Integrated luminosity for each run period of DØ Run II.

Run II-A	Run II-B1	Run II-B2	Run II-B3	Run II-B4	Total Run II
1081 pb^{-1}	1223 pb^{-1}	3034 pb^{-1}	1994 pb^{-1}	2404 pb^{-1}	9737 pb^{-1}

3.2. Monte Carlo Simulation

To understand the composition of the data sample, signal and background events are simulated based on theoretical predictions and must be compared to data. The simulation is carried out by Monte Carlo (MC) event generators that combine fundamental perturbative theoretical calculations with phenomonological models for a thorough simulation of the physics of an event.

3.2.1. Event Simulation

A complete hard-scattering event goes through several stages that can be simulated separately from matrix element to parton showering and hadronization. Fig. 3.2 shows the scheme of an event in $p\bar{p}$ interaction.

- **Matrix Element**

  The hard scattering is the starting point of the whole simulation chain. The interaction between the two colliding constituents are calculated with perturbative QCD. Unlike l^+l^- collisions where initial states are clean and well defined by two leptons, parton radiation adds complexity to the intial state of $p\bar{p}$ collision, for instance, gluon radiation from quarks or gluon self-couplings. As indicated in Fig. 3.2, the complexity of the event structure is multiplied by the radiation of gluons and color flow in $p\bar{p}$ events. We use ALPGEN [40] as the event generator for this analysis. ALPGEN has exact LO matrix element calclulations for multiparton fianl states in hadronic collision. It features weighted or unweighted parton-level generation. ALPGEN can be interfaced with PYTHIA [41] and HERWIG [42] to simulate the parton shower and hadronization processes in the evolution of the parton level state.

- **Parton Showering**

  Partons in the hard scattering process can radiate gluons in addition to pho-

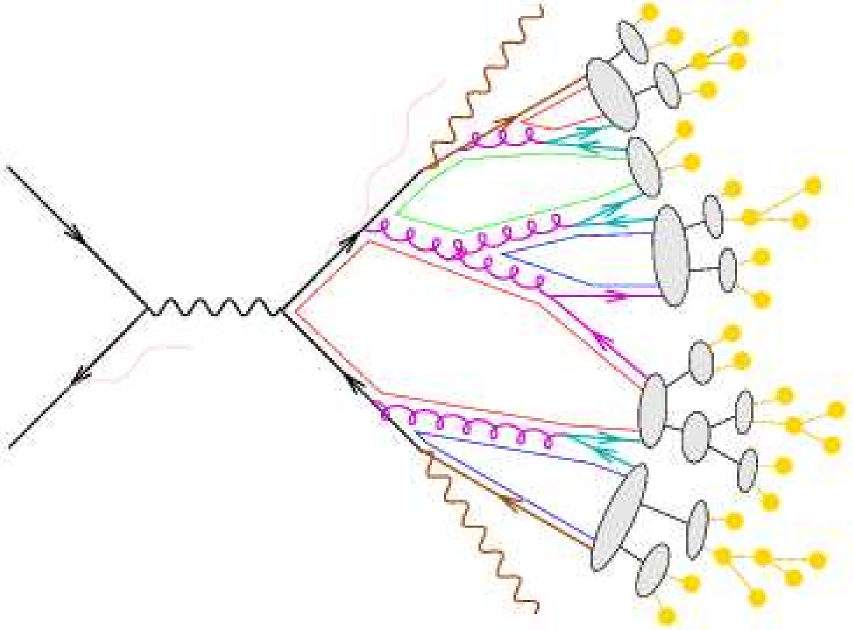

Figure 3.2. Schematic view of hard scattering process with subsequent parton showering and hadronization.

ton emission since they carry color charges. Due to the fact that gluons can also emit additional gluons or produce quark-antiquark pairs, partons can easily multiply and form showers of outgoing particles. This phenomenon is called *parton showering*. Radiation from different states of partons are discriminated according to their emitting source. The radiation of gluons and photons originated from the incoming partons is defined as *Initial State Radiation* (ISR), while the radiation from the outgoing partons is called *Final State Radiation* (FSR).

Both ISR and FSR are calculable perturbatively for large energy radiation. The nature of parton shower evolution requires higher order corrections on top of the leading order (LO) calculations. To reduce the work for the complicated higher order calculations, two methods are contrived with simplifications assumed. The *parton shower algorithm* creates the showers by adding one or more partons gradually to the final state parton emission chain where low momentum transfer can be of 1 GeV scale. The *color dipole ansatz* is based on consecutive emissions from colored dipoles, which are formed by parton pairs. The *parton shower algorithm* is employed by both PYTHIA and HERWIG, which are both used in this analysis for parton showering modeling and hadronization that is discussed below.

- **Hadronization**

  Beyond O(1) GeV energy scale, hadrons can be formed from parton fragmentation. Since QCD theory becomes non-perturbative at low energy scale, phenomenological models are required to describe hadronization at this stage. Two major models used across high energy physics field are *string fragmentation* and *cluster fragmentation*. Both models require experimental inputs to calibrate their free parameters. The string fragmentation model [43] illustrated in Fig. 3.3 is used in PYTHIA. This model is based on the fact that hadronization will eventually form color-neutral final state particles through color flows. Each string is an abstract color neutral unit with one color and its matching anticolor stretched at its ends. With new quark-antiquark pairs inserted, strings can be broken into pieces. In the end all broken pieces are regrouped to form final state hadrons. As an interaction mediating gauge boson, gluons act as kinks of the string. This process iterates until energy is too low to hadronize. HERWIG generator uses the cluster framentation model [44]. Every two quarks are grouped in a cluster as a fundamental unit for hadronization. Color singlet clusters are merged with adjacent clusters to form a color neutral shower branch. Color neutral clusters are then added to massive clusters, which are capable of generating quark-antiquarks pairs.

- **Parton Matching** Since ALPGEN only handles the hard scattering process and PYTHIA takes care of parton showering and hadronization, a double-counting issue arises when combining ALPGEN with PYTHIA for Monte Carlo simulation. ALPGEN simulate events with high jet multiplicity by producing extra partons (gluons). PYTHIA also generate extra jets in the showering and hadronization processes. To resolve this interfacing issue, a mechanism called MLM matching [45] is brought into ALPGEN. Separate ALPGEN samples are generated for different parton multiplicities. Jets in the final states are matched to the partons from the matrix element and events are rejected if the jet and parton multiplicity does not match. A weight is assigned to the events to compensate the loss of rejected events and amend the calculated cross section.

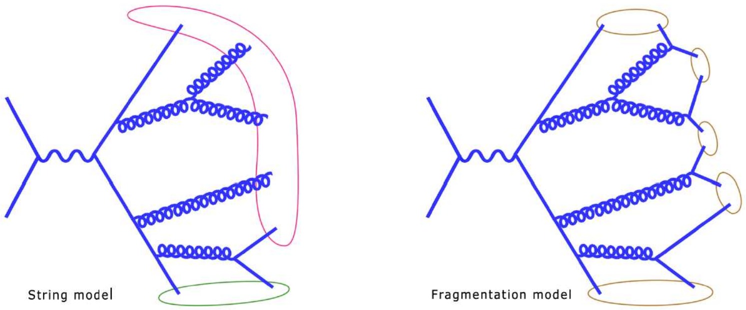

Figure 3.3. Diagram for string fragmentation model (Left) and cluster fragmentation model (Right). On the left diagram, the pink contour represents a string between two quarks kinked by gluons and the green contour is a string built directly between two quarks. The Brown contours on the right represent clusters formed by quark pairs.

3.2.2. Monte Carlo Samples

3.2.2.1. Signal samples

The $t\bar{t}$ samples are generated using ALPGEN and PYTHIA generators with a list of discrete top quark mass values from 130 GeV to 200 GeV: 130, 135, 140, 145, 150, 155, 160, 165, 170, 175, 180, 185, 190, 195, 200 GeV. An auxiliary sample is also generated with top quark mass as 172.5 GeV which helps populate the region nearest current measurements. The cross section calculation is up to leading order for quark-antiquark pair or gluon fusion input. The momenta of the partons of the incoming proton/anti-proton are randomly generated by ALPGEN with probabilities described by leading order parton distribution functions CTEQ6L1 [46] via the LHAPDF package. Inital/final state radiation (ISR/FSR) and hadronization are modeled by PYTHIA through parton showering and string fragmentation, respectively.

3.2.2.2. Background samples

For $t\bar{t}$ events in the dilepton channel, major backgrounds are Z boson and diboson ($WW/WZ/ZZ$) events where the two leptons originate from boson decays and jets are produced from ISR/FSR. $Z \rightarrow 2\ell$+jets background is generated similarly as $t\bar{t}$ events using ALPGEN and PYTHIA, while the production of $WW/WZ/ZZ \rightarrow 2l$+jets backgrounds involves PYTHIA only. Since both of the two backgrounds share a similar signature to the signal events, they are therefore classified as *physical backgrounds.*

Backgrounds caused by misidentifying electrons and muons due to instrumental effects are classified as *instrumental backgrounds.* The instrumental background is estimated from data for fake electrons and muons separately. For fake electrons, background contribution is estimated from events where the jets are misidentified as electrons. No EM ID requirement is applied in this process, with the exception that one electron in the ee channel has to fulfill. Then probabilities are estimated for events with a true electron pass the EM ID cut in the ee sample in data (ϵ_e) and for events with a misidentified jet pass the EM ID cut (f_e). The $\not\!\!E_{\mathrm{T}}$ is required to be < 15 GeV to avoid contribution from $W \rightarrow e\nu$+jets events. The number of events with misidentified electrons (N_{bkg}) is estimated as:

$$N_{loose} = N_{sig}/\epsilon_e + N_{bkg}/f_e, \tag{3.1}$$

$$N_{tight} = N_{sig} + N_{bkg}, \tag{3.2}$$

where N_{loose} is the number of events in the sample without applying EM ID cut, N_{tight} is the number after the selection, and N_{sig} is the number of events with true electrons in the sample. The number of events with muons from jets are estimated similarly.

3.2.3. Detector Simulation

In reality, particles can not be directly observed and identified but must go through comprehensive stages by means of detecting and analyzing their characteristics. A simulated event is an approximation of what nature sees but not what a human sees until it is represented to perception. To compare generated events with data, interactions between particles and detectors as well as readout signals also need to be properly simulated.

Two software packages are employed at DØ to simulate material interactions and electronic signals separately. A GEANT-based [47] software package, D0gstar, is used to simulate the interaction of partilces with the DØ detector and determine the energy deposition, scintillation, or ionization signals. The D0gstar output is then loaded to D0SIM, which simulate electronic signals and the pile-up of additional minimum bias interactions from data. The pile-up is included such that a random sample of a given MC event will reflect the luminosity profile of the data sample analyzed. The output of D0SIM is formatted the same way as data and then goes through regular reconstruciton and identification processes. The trigger is not simulated but parameterized with data in terms of lepton and jet observables and then applied to the MC samples. The probability for an event to pass trigger requirements is calculated out of the trigger efficiency of all leptons and jets. These single-object trigger efficiencies are obtained from data [38] [39].

Chapter 4

RECONSTRUCTION AND PARTICLE IDENTIFICATION

The initial form of data collected by the DØ detector is a collection of electronic signals and requires reconstruction and identification to form physical objects like electrons, muons and jets, etc. Details of a set of algorithms and criteria used in reconstruction and identification are described in this chapter.

4.1. Tracks

When charged particles pass within the solenoid their trajectories are bent by the magnetic field and hits are left in the SMT or CFT. Two algorithms are applied sequentially to reconstruct track trajectories from these hits.

- **The AA algorithm**. The Alternative Algorithm (AA) [48] starts with a combination of three or more hits to preselect the initial track candidates. Each track candidate is extrapolated and associated with additional hits found in the next SMT or CFT layer once they satisfy certain requirements, e.g. the χ^2 should be maintained within a specified threshold level as each hit is added. Once the criteria is not fulfilled with new hits, the original track hypothesis is split and new tracks are formed.
- **The HTF algorithm**. The Histogram Track Finding algorithm (HTF) [49] divides the detector into slices that are perpendicular to the magnetic field. Three parameters are employed to characterize each track in the transverse plane: the track curvature ρ, the distance of the closest approach (DCA) to the origin d_0 and the azimuthal angle to the center of the track projection ϕ.

> Each pair of hits from track candidates produce a 2-D histogram with respect to a point in the (ρ, ϕ) space. All pairs of hits on the same track trajectory reside at the same point of (ρ, ϕ), while hits from different tracks distribute randomly in the histogram as background. Each hit can be passed through by a circle centered at arbitrary point. These circles correspond to a straight line in the (ρ, ϕ) parameter space. Therefore, a single hit can also be described by a straight line in the (ρ, ϕ) space. Each intersection of the lines corresponds to a track candidate.

The AA algorithm is more efficient and has lower background for low p_T and high impact parameter tracks. The HTF algorithm has a higher fake rate than the AA algorithm but treats high p_T tracks more efficiently [50].

4.2. Vertex Reconstruction

4.2.1. Primary Vertex

The location of the hard interaction in a $p\bar{p}$ collision is described by a geometrical point known as the *primary vertex* (PV). All the particles coming out of the hard scattering interaction emanate from this point. A precise measurement of the PV is important as it can be used to distinguish the objects from those out of underlying events as well as identify $\not{E}_T$. It also allows the identification of long-lived particles such as B hadrons.

At DØ, primary vertices are reconstructed using an *adaptive primary vertex algorithm* [51]. The first step of the vertex reconstruction starts with selecting tracks with $p_T > 0.5$ GeV and two or more SMT hits within the SMT fiducial region. A so-called *z-clustering algorithm* is applied to collect tracks that are within 2 cm from each other 2 cm along the beam axis to form clusters. These clusters are fitted separately in the last fitting stage. A special parameter *impact parameter significance* which is defined as the impact parameter divided by its uncertainty ($d_0/\sigma(d_0)$) is introduced to pre-select the tracks. The impact parameter significance is required to be smaller than 5.

After pre-selection is done, the vertex reconstruction starts with the adaptive vertex fitting algorithm. This algorithm is based on Kalman filter [52] with an extension that the errors of the contributing tracks are weighted by a sigmoidal function, which is defined as:

$$w_i = \frac{1}{1 + e^{(\chi_i^2 - \chi_{cutoff}^2)/2T}}, \tag{4.1}$$

where χ_i^2 is the χ^2 contribution from the i-th track, χ_{cutoff}^2 is a cutoff constant where the weight function drops to 0.5, T is the parameter that controls the sharpness of the function.

The Kalman filter is used iteratively and tracks with weights $w_i < 1 \times 10^{-6}$ are excluded from the fitting iteration. The fitting process is repeated until the weights meet the stable requirement ($|w_i - w_{i-1}| < 1 \times 10^{-4}$) within 100 iterations.

After the initial stage of reconstructing event vertices, the next step is to distinguish hard-scattering vertices from minimum bias vertices. A probabilistic approach [53] is applied to assign each track a probability of originating from a minimum bias vertex. This approach takes the fact that minimum bias tracks have smaller $p_T's$ in contrast to hard-scattering tracks. Then the vertex minimum bias probability is calculated by multiplying the minimum bias probability from all contributing tracks. The vertex with lowest minimum bias probability will be selected as the primary vertex.

4.2.2. Secondary Vertex

Due to the fact that heavy hadrons can travel up to several millimeters in the detector, a secondary vertex can be reconstructed and used in tagging b jets and identifying heavy hadrons. The reconstruction procedure involves track jet reconstruction, track selection, vertex finding and final vertex selection [54] [55] [56].

Track jets [57] are independent of jets from calorimeter noise and are not affected by tracker-calorimeter misalignment. Therefore, the secondary vertex reconstructed from track jets is independent from the calorimeter reconstruction. The track clustering starts by adding tracks in decreasing order of p_T to z-pre-clusters [54] if the distance in z is smaller than 2 cm between the track and pre-cluster. Then track selection is performed for each of the clusters. The requirement includes > 1 SMT hits, $p_T > 0.5$ GeV, the distance of the closest approach to the nearest vertex $DCA < 0.2$ cm and $Z_{dca} < 0.4$ cm. In each cluster, $\mathcal{R}_{\text{cone}} = 0.5$ cone algorithm is used to form track jets. Tracks with $DCA/\sigma_{DCA} > 3$ are selected, where σ_{DCA} is the uncertainty of DCA. Unlike primary vertex, Kalman Filter algorithm is employed to reconstruct secondary vertex for track jets with at least two tracking selected by the DCA/σ_{DCA} requirement. It starts by fitting all combinations of track pairs in the track jet to reconstruct a seed vertex. Each seed vertex is added with additional tracks until χ^2 is beyond a certain threshold or no more tracks are available. Sharing tracks are allowed between reconstructed vertices, while for b-tagging it is avoided by algorithms in the Neural Network b-tagger [58].

4.3. Electrons and Photons

Because electrons and photons deposit almost all of their energy in the EM calorimeter in the form of showers, they are often grouped together as “EM objects”. Only electrons leave tracks in the central tracking system since photons are electrically neutral. Therefore, the identification of electrons utilizes both tracks and energy deposition whereas photons do not have a matching track to the clustered energies. In addition, the shower development in the calorimeter are also different for electrons and photons. Electrons shower via bremsstrahlung first while photon showers initially via electron pair production. After subsequent interactions, particles multiply to a maximum at some depth in the calorimeter. Thereafter, electron showers develop through ionization and photons through compton scattering.

The reconstruction of EM objects starts with finding seed clusters in the calorimeter. A cluster contains all the towers within a 0.1×0.1 cone in $\eta \times \phi$ space around a seed tower that has $p_T > 500$ MeV. The p_T of the cluster is required to be above 1.5 GeV. The energy fraction (f_{EM}) in the EM calorimeter over the total energy deposition (E_{tot}) in the calorimeter must be high and is therefore required to be:

$$f_{EM} = \frac{E_{EM}}{E_{tot}} > 0.9, \tag{4.2}$$

A bigger concentric cone with $\Delta R < 0.4$ is constructed around the seed tower to isolate EM objects from surrounding clusters. The EM energy within the $\Delta R < 0.2$ cone is also required to be at a high fraction comparing to the total energy within the $\Delta R < 0.4$ cone:

$$f_{iso} = \frac{E_{tot}(\Delta R < 0.4) - E_{EM}(\Delta R < 0.2)}{E_{EM}(\Delta R < 0.2)}. \tag{4.3}$$

The longitudinal showers also develop differently between EM objects and hadronic objects. The similarity to an EM shower is quantified by a 7×7 covariance matrix (H-matrix) [59] which is parameterized by seven correlated variables: energy deposited in the four EM layers, the shower energy in the EM calorimeter, the z position of the primary vertex divided by its uncertainty, and the width of the shower in $r - \phi$ plane in the third EM layer. For clusters to be identified as EM objects, the χ^2 of the H-matrix (χ^2_{H7}) should satisfy:

$$\chi^2_{H7} < 50. \tag{4.4}$$

Electrons are charged particles so they leave tracks in the tracking system. Each electron cluster must match to at least one reconstructed track within a small cone $\Delta\eta \times \Delta\phi < 0.05 \times 0.05$ around the center of the third EM layer cells of the cluster. The track matching $\chi^2_{\textit{EM-track}}$ is calculated as follows:

$$\chi^2_{\textit{EM-track}} = \left(\frac{\Delta\phi}{\sigma_{\Delta\phi}}\right)^2 + \left(\frac{\Delta z}{\sigma_{\Delta z}}\right)^2 + \left(\frac{E_T/p_T - 1}{\sigma_{E_T/p_T}}\right)^2, \tag{4.5}$$

where $\Delta\phi$ and Δz are the differences between the positions of the third layer EM cluster and track, E_T/p_T is the transverse energy of the EM cluster divided by the transverse momentum of the track and σ_x is the experimental resolution of variable x.

The probability of a track matched to a EM cluster $Prob(\chi^2_{\textit{EM-track}})$ is calculated and the track with the highest probability is picked as the electron track. EM Objects without a matching track are more likely photons.

The electrons selected with the above criteria are so-called “loose isolated electrons”. To become “tight isolated electrons”, “Loose isolated electrons” have to pass additional cuts. In the analyses prior to 4.3 fb^{-1}, the tight requirement is to pass a electron likelihood cut ($L_e > 0.85$). The electron likelihood [60] is constructed based on seven tracking and calorimeter parameters, including χ^2_{H7}, DCA, and track isolation calculated in an annulus of $0.05 < \Delta R < 0.4$ around the electron. In current 9.7 fb^{-1} analysis, the tight requirement is replaced by Boosted Decision Trees (BDT) [61], which uses a great number of variables that are significantly different for signal and background for strong discrimination. These variables include those used for electron likelihood construction, L_e itself, hits in SMT and CFT, and also information in CC, EC, all layers of EM and the first layer of FH. The BDT is trained separately for the CC and EC, and for high and low luminosities. The BDT working points are channel dependent and different cuts are used, respectively.

4.4. Muons

At DØ, an independent muon detector system is constructed to help identify muons. The muon system unambiguously identifies muon candidates, and the tracking systems provide precise measurements on muon tracks and momenta [62]. Each of A, B and C layers have 3 or 4 layers of drift tubes, so that segments are able to be found in A (before the toroid) and B+C (after the toroid). These segments are used to find tracks in the muon system. The layer wire and scintillator hits in A, B and C layers of the muon system are matched together to a central track. By looking at the signatures from *minimum ionizing particles* (MIP) in the calorimeter, a so-called "Muon Tracking in the Calorimeter" (MTC) algorithm is also developed to improve identification of muons.

The muon types (*nseg*), quality parameters and their meanings are summerized in Table 4.1. The sign of *nseg* represents if the muon candidate is successfully matched to a central track. The muon quality is classified as *loose*, *medium* or *tight* according to *nseg* and the hit patterns in the three layers of muon system.

- **tight muon:** Only $|nseg| = 3$ muons can be tight muons. Additionally, it also requires:
  - at least two A layer wire hits
  - an A layer scintillator hit
  - at least three BC layer wire hits

Table 4.1: The muon type and quality definitions.

nseg	*segment*	*central track match*	*MTC match criteria*
3	A+BC	muon to central or central to muon	$\Delta\eta, \Delta\phi$ between MTC and central track extrapolated to CAL
2	BC only	central to muon	as above
1	A only	central to muon	as above
0	muon hit or MTC	central to muon and CAL	as above
-1	A only	no match	$\Delta\eta, \Delta\phi$ between MTC and A layer segment
-2	BC only	no match	$\Delta\eta, \Delta\phi$ between MTC and BC layer segment
-3	A+BC	no match	$\Delta\eta, \Delta\phi$ between MTC and local muon track at A layer if fit converged, otherwise A segment position

  - at least one BC scintillator hit
  - a converged fit within the muon system ($\chi^2_{loc} > 0$)
- **medium muon:**
  - $|nseg| = 3$
  - at least two A layer wire hits
  - an A layer scintillator hit
  - at least two BC layer wire hits
  - at least one BC layer scintillator hit except for central muons with less than four BC wire hits

  or

  - $|nseg| = 2$
  - at least two BC layer wire hits
  - at least one BC layer scintillator hit
  - located in the octant 5 and octant 6 with $|\eta_{det}| < 1.6$

  or

  - $|nseg| = 1$
  - at least two A layer wire hits
  - an A layer scintillator hit
  - located in the octant 5 and octant 6 with $|\eta_{det}| < 1.6$
- **Loose muon:**
  - A $|nseg| = 3$ loose muon is defined the same as medium muon with the exception that one of the above tests may fail. The A wire and scintillator

requirement is combined as one test and at least one scintillator is always essential.

  - A $|nseg| = 2$ or $|nseg| = 1$ loose muon is defined the same as the corresponding medium muon with the exception that it is not required to be located in the octant 5 and octant 6 with $|\eta_{det}| < 1.6$.

Similar to the muon quality categorization, track quality is also classified as three types: *loose*, *medium* or *tight*.

- *loose track*. $|DCA| < 0.2$ cm. If track has SMT hits DCA cut is changed to $|DCA| < 0.02$ cm.

- *medium track*. In addition to fulfilling the loose track requirements, medium track should also satisfy $\chi^2_{dof} < 4$.

- *tight track*. In addition to the requirement of being a medium track, a tight track should have SMT hits.

A cosmic veto cut is applied by requiring that the muon flight time between the hard scattering point and the A layer (t_A) and the BC layer (t_{BC}) to be less than 10 ns. Muons with $t_A > 10$ ns or $t_{BC} > 10$ ns are categorized as cosmic rays and rejected.

Muons passing the above criteria within $\Delta R > 0.5$ are called *loose isolated muons. Tight isolated muons* are loose isolated muons with two additional requirements.

- $Rat11 = Halo(0.1, 0.4)/p_T^{\mu} < 0.08$

- $Rattrack = TrkCone(0.5)/p_T^{\mu} < 0.06$

where p_T^{μ} is the transverse momentum of the muon. *Halo(0.1, 0.4)* is the sum of the transverse energies from all calorimeter clusters in a hollow cone with the inner radius as 0.1 and outer radius as 0.4 around the muon. Only fine hadronic and EM calorimeters are considered. *Trkcone(0.5)* is the sum of the transverse momenta from all tracks within a cone of radius as 0.5 around the muon. The transverse momentum of the muon itself is excluded from the sum.

4.5. Jets

Unlike electrons or photons which can be detected as a single particle, hadrons are more "active" and usually exist in the form of particle bunches due to color confinement. The initial parton evolves around the original flight direction with particles produced by parton hadronization and gluon soft radiation. To model these bunches of particles, a cone-based algorithm is designed with the name *jet algorithm* [63]. There is no unique definition of jet but in general it is described as " large amount of hadronic energy in a small angular region".

The content of a jet is not essentially restricted to hadrons, there could be electrons, muons and photons as well from particle decay. Jet contents vary widely and jet shower shapes differ significantly. Jets deposit energy not only in hadronic layers of the calorimeter but also in the electromagnetic layers. The jets in $p\bar{p}$ collisions originate from hard-scattering partons, initial/final state radiation (ISR/FSR) partons and beam remnants (beam jets).

4.5.1. Jet Reconstruction

An efficient jet reconstruction algorithm has to satisfy certain theoretical and experimental criteria. The main theoretical requirements are: (1) seed particles for the jet algorithm should be independent of soft radiations, e.g. gluon soft radiation, (2) the solution of the jet algorithm should be insensitive to collinear radiations, and (3) the longitudinal momenta of the interacting partons in hadron collisions has a spectrum provided by parton distribution functions (PDF). Therefore the center-of-mass of the parton collision system moves with unknown velocity along the beam axis. Lorentz-invariance for boosts along the beam axis is required for all observables and reconstruction steps of the jet algorithm.

There are also experimental criteria for an ideal jet algorithm that requires: (1) the jet finding technique should be insensitive to multiple hard scattering processes at high luminosity, (2) all primary jets of an event must be identified by the algorithm, (3) the effects of energy and angular resolution, and systematic angle biases should not be amplified by the algorithm, and (4) the performance of the algorithm should be independent of the detector ideally.

At DØ, the "Improved Legacy Cone Algorithm" (ILCA, or RunII Cone Algorithm) [64] is employed for the reconstruction of jets. The cone algorithm is designed with the idea of enclosing the particle shower within a radius $\Delta R = \sqrt{(\Delta\eta)^2 + (\Delta\phi)^2}$. The noisy cells in the calorimeter are rejected using T42 algorithm [65] to improve jet energy scale and missing transverse energy resolution.

The cone algorithm consists of three stages: In the first stage calorimeter towers are preclustered by Simple Cone Algorithm. All towers with $p_T^{tower} > 0.5$ GeV are selected as seeds and sorted and listed in a decreasing p_T^{tower} order. Seeds with the highest p_T^{tower} in the list are grouped with surrounding towers in a cone of radius $\Delta R = 0.3$ and all clustered towers are removed from the list. This procedure iterates with the next leading tower on the list until all towers are preclustered. The preclusters with $p_T^{precluster} > 1$ GeV and at least two towers are passed on to the next stage.

At second stage, preclusters serve as the seed for the construction of *proto-jets*. The proto-jet is built from the preclusters with the highest $p_T^{precluster}$ from the list with a cone of radius $\Delta R = 0.5$. The cone center is recalculated iteratively with each add-on of a precluster within the cone until all the jet centers are found and stable

($\Delta R < 0.001$). The stable jet candidates are termed proto-jets.

The final stage of the algorithm is merging and splitting proto-jets. Each pair of the proto-jets with distance in R larger than the cone size but smaller than twice of the cone size are processed. If the energy shared by two adjacent proto-jets is more than 50% then the two jets are merged to form a new proto-jet. If the overlapping energy is less than 50% the two jets are split by assigning the preclusters to the closest of the two proto-jets in $\eta \times \phi$ space. The merging/splitting process repeats until all jets are stable and do not overlap with each other. Finally all jets with $p_T > 6$ GeV are qualified for identification in the next step and the disqualified ones are considered unphysical and discarded.

4.5.2. Jet Identification

The jet reconstruction algorithm could sometimes misreconstruct large noise fluctuations in the calorimeter as a jet. To distinguish real physical jets from fake jets, a set of requirements [66] are compiled to test the quality of jet candidates:

- To discriminate EM objects and jets, the electromagnetic fraction f_{EM} is required to be less than 0.95. Furthermore, minimum cuts on f_{EM} are applied with a dependence on η_{det} to suppres noise.
- To remove jets dominated by high level calorimeter noise, η_{det} dependent cuts are also applied to the coarse hadronic fraction (f_{CH}) which is defined as the energy deposited in the coarse hadronic layer over the total energy ($f_{CH} = E_{CH}/E_{tot}$):
    - $|\eta_{det}| < 0.8$: $f_{CH} < 0.44$
    - $0.8 < |\eta_{det}| < 1.5$: $f_{CH} < 0.6$ for narrow jets, and $f_{CH} < 0.4$ for wide jets
    - $1.5 < |\eta_{det}| < 2.5$: $f_{CH} < 0.46$

- A portion of the jet energy should be measured in the independent readout of the Level 1 trigger [67]. The Level 1 ratio is defined as:

  $$L1_{ratio} = \frac{p_T^{L1readout}}{p_T^{reco}(1 - f_{CH})}, \tag{4.6}$$

  where $p_T^{L1readout}$ is the scalar sum of trigger tower $p_T s$ in a cone of $\Delta R = 0.5$. p_T^{reco} is the transverse momentum of the reconstructed jet. The sum of the energies of Level 1 trigger involves only the 100 hottest calorimeter towers and the coarse hadronic layers are excluded.

  - $L1_{ratio} > 0.5$
  - $L1_{ratio} > 0.35$, jet $p_T < 15$ GeV in $|\eta_{det}| > 1.4$
  - $L1_{ratio} > 0.1$, jet $p_T < 15$ GeV in $|\eta_{det}| > 3.0$
  - $L1_{ratio} > 0.2$, jet $p_T \geq 15$ GeV in $|\eta_{det}| > 3.0$

4.6. Missing Transverse Energy

Neutrinos barely interact with other particles and they can penetrate the whole detector sector without triggering a single pulse of signal. Although a direct identification of neutrinos is not executable at DØ, they can still be inferred in terms of missing transverse energy ($\not{E}_T$). The four-momentum conservation in the transverse plane requires the vector sum of transverse momentum to be zero [68]. If all observables are perfectly reconstructed, the contribution from neutrinos can be calculated as the negative sum of all observed particles' transverse momenta:

$$\vec{\not{E}}_T = -\sum_i \vec{p}_{Ti}. \tag{4.7}$$

The sum is performed over all the cells in electromagnetic and fine hadronic layers of the calorimeter, ICD and massless gap with T42 algorithm applied to remove noise. The coarse hadronic caorimeter is not included due to its large noise background.

Since EM objects, muons and jets undergo offline reconstruction and correction, $\not{E}_T$ meeds to be corrected as well with respect to any changes made to the object energy. Muons deposit a small portion of energy in the calorimeter when they pass through, which needs to be subtracted from the raw $\not{E}_T$. The jet energy scale corrects the energy of all jets in a events, which could contribute major changes to the transverse balance of momenta. The corrected $\not{E}_T$ is given by:

$$\vec{\not{E}}_T{}^{corr} = \vec{\not{E}}_T{}^{uncorr} - \sum_{i=1}^{N_{muons}} \vec{p}_{T_i}^{\,calorimeter} - \sum_{j=1}^{N_{objects}} \left(\vec{p}_{T_j}^{\,corr} - \vec{p}_{T_j}^{\,uncorr}\right), \tag{4.8}$$

where i runs over all the muons with energy deposition in the calorimeter and j runs over all other objects. $\vec{p}_{T_j}^{\,corr}$ and $\vec{p}_{T_j}^{\,uncorr}$ are the corrected and uncorrected momenta of each corresponding object.

4.7. Identification of b jets

The ability to identify jets originated from b quarks is important for the analyses at DØ experiment and is crucial for studies of the top quark and the Higgs boson.

4.7.1. Taggability

b jet identification involves only tracking and vertex information, so it is important to have reconstructed jets matched with tracks in the tracking system. This "taggability" is separated from the requirements in the b jet identification algorithm to make the identification procedure less dependent on possible variations of the tracking system efficiency. A *taggable* jet reconstructed in the calorimeter is required to have at least two tracks matched within a $\mathcal{R}_{\text{cone}} = 0.5$ cone.

4.7.2. V^0 rejection

Neutral hadrons that contains strange quarks have similar decay signatures to those of b hadrons. To suppress this background, secondary vertices with two oppositely charged tracks are rejected with the following criteria: (1) the z projection of each track has $DCA < 1$ cm, (2) $DCA/\sigma_{DCA} > 3$, (3) the tracks associated with the V^0 candidate must have $DCA < 200$ μm, and (4) the invariant mass of the two tracks must be outside the mass range expected from K_S or Λ.

4.7.3. MVA$_{bl}$ Algorithm

Prior to 2010, DØ used three algorithms to identify b jets: Counting Signed Impact Parameters (CSIP), Jet Lifetime Impact Parameter (JLIP) and Secondary Vertex Tagger (SVT) [69]. The input variables from these tools were combined using a neural network (NN) to construct the DØ NN-algorithm (D0-NN), which has significant improvements over the first-level algorithms. A new algorithm called MVA$_{bl}$ (multivariate analysis that discriminates between b quarks and light quark jets) algorithm [69] is developed using extended set of input variables, and both BDT and neutral network. The MVA$_{bl}$ algorithm uses simulated di-b jet signal events and di-light jet background events. In total, 9 variables from the impact parameter and 29 secondary vertex variables are used to train six random forests (RF) using the ROOT TMVA [70] framework. One of the RF is trained using the impact parameter from the CSIP and JLIP algorithms. The other five RFs use each set of secondary vertex variables from the five different SVT algorithms configurations. The combination of the six RFs is performed using a NN implementation, the TMULTILAYERPERCEPTRON (MLP), and the ROOT framework. This NN produces the MVA$_{bl}$ output using non-linear correlations between inputs to improve discrimination over the D0-NN by the inclusion of an order of magnitude more variables.

Chapter 5

JET ENERGY CALIBRATION

The measured energy of a jet can be distorted relative to an initial parton by several effects. These effects can be grouped into those due to the experimental configuration, and those due to physics (see Fig. 5.1). The latter include soft gluon radiation (ISR/FSR), fragmentation, and color reconnection effects. These are not corrected for and are taken up in the analysis discussed in Chapters 6 - 8. This chapter focuses on the effects due to experimental configuration, which can be corrected for, and have uncertainties determined. These include the response due to detector non-linearity, uninstrumented regions, energy deposition in the liquid argon from Uranium decays, reconstruction and resolution effects. To get an accurate determination of jet energy, a set of corrections are employed which is globally termed as Jet Energy Scale (JES). The goal of this correction is to obtain a corrected jet energy that on average is equal to the energy of a "particle jet", which is defined as the particles produced inside a jet cone by the primary $p\bar{p}$ interaction. Therefore, particles before entering the calorimeter are often referred to as the "particle level", and particles identified and measured in the detector are called the "reconstructed level" or "detector level". The DØ jet energy calibration is built to get data and MC onto the same footing, so the data/MC ratio is aimed to corrected to 1 after all calibrations. This chapter describes the methods employed by the DØ Collaboration to determine the JES for jets reconstructed with the Run II Cone Algorithm [64]. This is an effort in which I contributed several components.

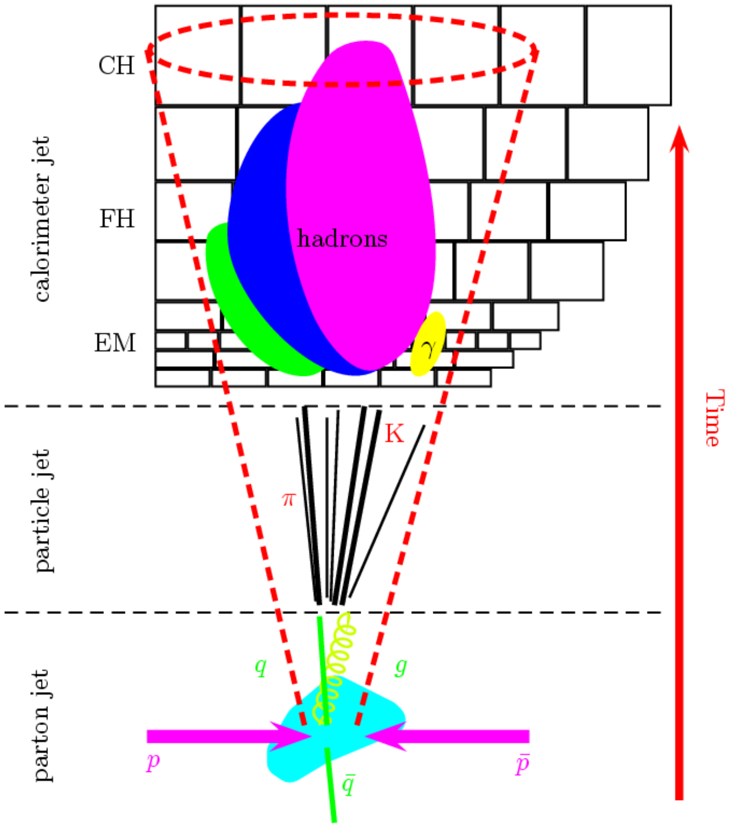

Figure 5.1. Sketch of the evolution of a parton from the hard-scattering to a jet in the calometer.

5.1. Standard Jet Energy Scale Correction

The calibration of jet energy involves a number of corrections with respect to different distortions [71]. The corrected jet energy is defined as:

$$E_{\mathrm{jet}}^{\mathrm{corr}} = \frac{E_{\mathrm{jet}}^{\mathrm{meas}} - E_0}{R_{\mathrm{jet}} k_R S_{\mathrm{jet}}} k_0 F^{corr}. \tag{5.1}$$

- $E_{\mathrm{jet}}^{\mathrm{corr}}$ is the corrected jet energy.
- $E_{\mathrm{jet}}^{\mathrm{meas}}$ is the measured jet energy.
- E_0 is an energy offset that arises from energy deposits associated with noise and pile-up (additional $p\bar{p}$ collisions within the same bunch crossing) [71].
- R_{jet} is the calorimeter response to the energy deposited by the particles that make up the jet. It is dependent on the jet energy, rapidity, and detector run period. It is also dependent on jet flavors to bring data and MC into agreement. The determination of R_{jet} uses the missing E_T projection fraction (MPF) method (see Sec. 5.1.1).
- F^{corr} is the single particle correction that applied to each particle composition in a jet to bring data and MC into agreement (see Sec. 5.1.5).
- S_{jet} is the showering correction that corrects for migration of energy in and out of the cone because of the finite size of the energy deposition patterns in the calorimeter.
- The factors k_0 and k_R are corrections for biases in the determination of the offset energy E_0 and the detector response R_{jet}.

Of these factors, the response is the only term that results in energy being missed by the calorimeter, and this effect alone must be used to correct the event $\not{E}_{\mathrm{T}}$.

5.1.1. Missing E_T Projection Fraction Method

The "Missing E_T Projection Fraction Method" (MPF method) [72] utilizes the two-body process X+jets to measure the response of jets, where $X(=\gamma$, Z or jet) is a well-measured object referred to as the "tag object", and the jet is called the "probe object".

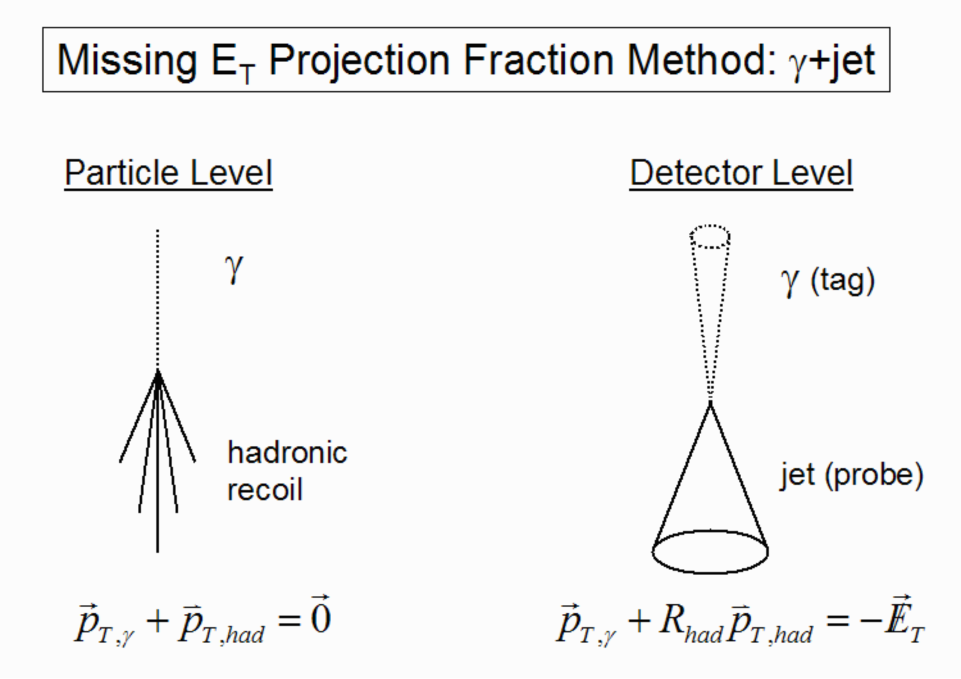

Figure 5.2. Illustration of MPF correction in γ+jet events at the particle level and detector level.

In the transverse plane, momentum conservation at the particle level requires $\vec{p}_{\mathrm{T,tag}}$ and of the hadronic recoil, $\vec{p}_{\mathrm{T,recoil}}$, to be balanced,

$$\vec{p}_{\mathrm{T,tag}} + \vec{p}_{\mathrm{T,recoil}} = 0. \tag{5.2}$$

Since the response of the tag object (R_{tag}) and of the hadronic recoil (R_{recoil}) might be different due to experimental effects, there can be an imbalance in their measured transverse momenta (see Fig. 5.2):

$$\vec{p}_{\text{T,tag}}^{\,\text{meas}} + \vec{p}_{\text{T,recoil}}^{\,\text{meas}} = -\vec{\not{E}}_{\text{T}}^{\text{meas}}, \tag{5.3}$$

where $\vec{p}_{\text{T,tag}}^{\,\text{meas}} = R_{\text{tag}}\vec{p}_{\text{T,tag}}$ is the measured transverse momentum of the tag object, $\vec{p}_{\text{T,recoil}}^{\,\text{meas}} = R_{\text{recoil}}\vec{p}_{\text{T,recoil}}$ is the measured transverse momentum of the hadronic recoil, and $\vec{\not{E}}_{\text{T}}^{\text{meas}}$ is the measured $\not{E}_{\text{T}}$ in the event.

Combine Eqs. 5.2 and 5.3, and we get:

$$\frac{R_{\text{recoil}}}{R_{\text{tag}}} = 1 + \frac{\vec{\not{E}}_{\text{T}}^{\text{meas}} \cdot \vec{n}_{\text{T,tag}}}{p_{\text{T,tag}}^{\text{meas}}}, \tag{5.4}$$

which shows that the ratio of responses between the hadronic recoil and the tag object can be estimated from the projection of $\vec{\not{E}}_{\text{T}}$ onto the tag object direction in the transverse plane ($\vec{n}_{\text{T,tag}}$) and $p_{\text{T,tag}}^{\text{meas}}$. Ideally, when the probe jet and the hadronic recoil are identical, $R_{recoil} = R_{jet}$. This relation can be affected by the presence of additional jets in events. To improve the approximation, exactly two back-to-back objects are required. Residual effects are at the percent level and are corrected as described in Sec. 5.1.4.5.

Since photons are well-measured and their response can be considered unitary after correcting to particle level, by using γ+jet events, we can measure the response to jets to be:

$$R_{\text{MPF}}^{\gamma^{\text{meas}}+\text{jet}} = 1 + \frac{\vec{\not{E}}_{\text{T}}^{\text{meas}} \cdot \vec{n}_{\text{T}\gamma}}{p_{\text{T}\gamma}^{\text{meas}}}. \tag{5.5}$$

Eq. 5.5 shows that the jet response is dependent on both jet energy and η. To minimize effects from poor jet energy resolution, which can cause a bias in the estimated jet response when binning as the measured probe jet energy [73], we instead use E', which is defined as:

$$E' = p_{\text{T}\gamma}^{\text{meas}} \cosh(\eta_{\text{jet}}), \tag{5.6}$$

where $\eta_{\rm jet}$ is the jet pseudorapidity with respect to the reconstructed event primary vertex. Since photon energy and jet η are more precisely measured quantities than the jet energy, E' is a more precise estimator of the particle level jet.

Due to the inhomogeneity of the detector (e.g. gaps between CC and EC), the jet response is first determined in a more homogeneous central region ($|\eta^{det}|$ <0.4) (see Sec. 5.1.2 and 5.1.3). The extrapolation of central response to all the detector regions is performed with η-dependent correction, which is discussed in Sec. 5.1.4.

The energy dependence of the calorimeter response to hadrons is nearly logarithmic as a result of the slow rise of the fraction of π^0's as a function of the incident hadron energy during the hadronic shower development [74], in combination with the non-compensating nature of the calorimeter. In the homogeneous region in CC ($|\eta^{det}| < 0.4$), this dependence for jets can be parameterized by a quadratic logarithmic function:

$$R(E') = p_0 + p_1 \log(E'/E_0) + p_2 \log^2(E'/E_0), \tag{5.7}$$

where $E_0 = 100$ GeV and p_i $(i = 0, 1, 2)$ are free parameters to be determined in a fit.

5.1.2. Absolute response in data

The determination of absolute jet response is performed with γ+jet events (see Fig. 5.3) in the CC. Both photon and the probe jet are required to be back-to-back ($|\Delta\phi| > 3.0$), and in the region $|\eta^{det}| < 0.4$.

The absolute MPF responses measured in data as a function of E' are shown in Fig. 5.4 for $\mathcal{R}_{\rm cone} = 0.7$ jets and $\mathcal{R}_{\rm cone} = 0.5$ jets for all Run II-B periods. Each jet algorithm identifies a unique set of jets that needs to be calibrated per algorithm. The $\mathcal{R}_{\rm cone} = 0.5$ jets and corresponding calibrations are employed by the top quark mass measurement in both the dilepton and ℓ+jets channels. As can be seen, only very slight systematic variations for run range are measured in data.

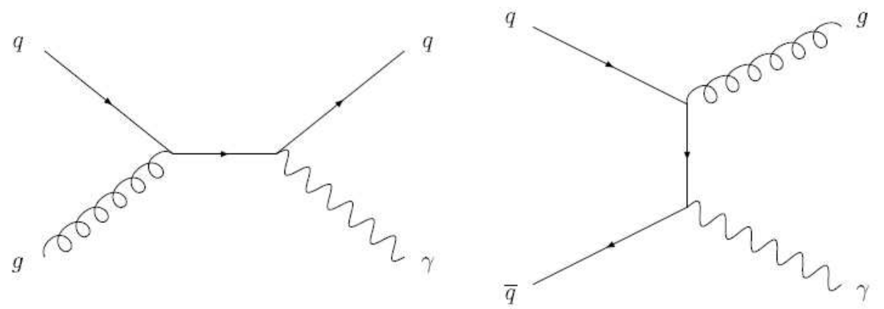

a. Compton scattering b. Quark–anti quark annilation

Figure 5.3. The main Feynman diagrams of the direct photon production in γ+jet events.

5.1.3. Absolute response in MC

The data and MC jet response can be different due to difficulties in accurate modeling of some instrumental effects (e.g. the calorimeter response to hadrons). Therefore, separate determinations of data and MC jet response are required. The MPF method was first used successfully to measure the calorimeter response in data [75]. Since MC samples have particle level information, which is absent in data, the MC MPF response can be used to study the biases of the method and develop potential correction procedures for data. The variable $p_{\mathrm{T}\gamma}^{\mathrm{meas}}$ is an approximation of the particle level photon energy, which in MC is not needed and replaced by the matched true photon $p_{\mathrm{T}\gamma}$. The $\not{E}_{\mathrm{T}}$ is also corrected accordingly in MC.

As in data, the derivation of MC MPF response uses γ+jet samples. The event selection is made identical for Run II-A and all Run II-B periods. Events with no reconstructed primary vertex or with more than two primary vertices are rejected. Exactly one photon candidate with measured transverse momentum $p_{\mathrm{T}\gamma}^{\mathrm{meas}} > 7$ GeV

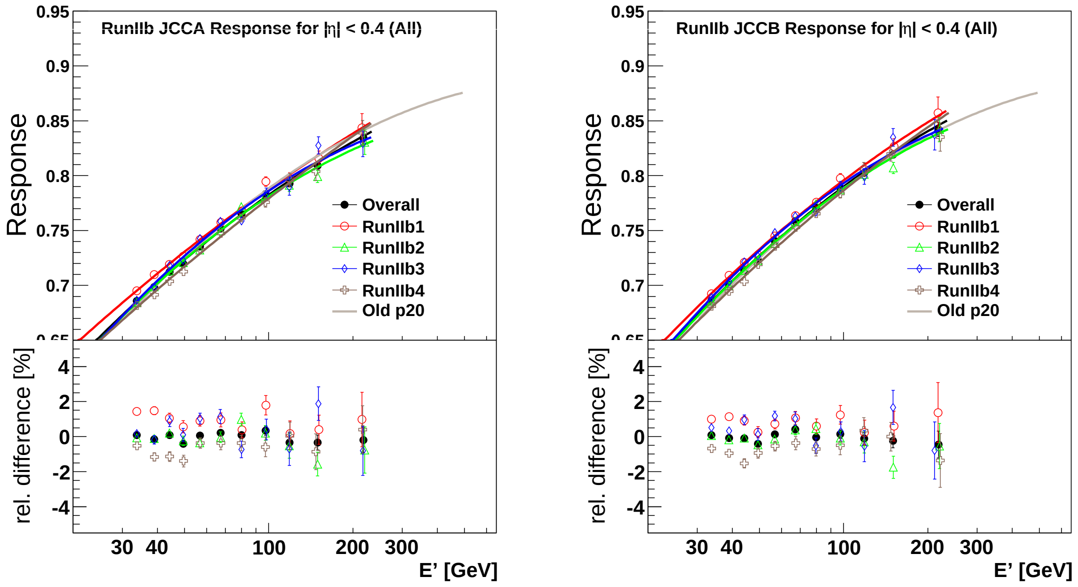

Figure 5.4. Absolute MPF response in data for $\mathcal{R}_{\text{cone}} = 0.7$ jets (left) and for $\mathcal{R}_{\text{cone}} = 0.5$ jets (right) as a function of E'. The solid lines indicate the fit to the function in Eq. 5.7. The bottom plots show the relative difference of the points with respect to the fitted function of the overall Run II-B data. The JCCB jet corresponds to a jet with the cone size $\mathcal{R}_{\text{cone}} = 0.5$, and the jets with $\mathcal{R}_{\text{cone}} = 0.7$ is called JCCA.

satisfying the tight photon identification criteria is required. In addition, this photon must be in the central calorimeter with $|\eta^{det}| < 1$. Exactly one reconstructed jet (with $\mathcal{R}_{\text{cone}} = 0.7$ or 0.5) satisfying the jet selection criteria within $|\eta^{det}| < 0.4$ is also required. No additional jet is allowed (except if it matches the photon candidate within $\Delta R < 0.2$ since the photon candidate can also be reconstructed as a jet). The photon candidate and jet candidate must be back-to-back to each other with $\Delta\phi > 3.0$.

We estimated the absolute MPF response in MC separately for each run period. The low energy region (< 50 GeV) has relatively less statistics due to the fact that the γ+jet samples are generated with the transverse momentum of the outgoing partons set in-between different thresholds. Run II-B1 and Run II-B2 has additionally generated low p_T samples. Run II-B3 and II-B4 do not have these additional samples since we found that the improvement from increasing low energy region is negligible. In the comparison among all Run II-B MC epochs (Fig. 5.5), the jet responses in different epochs are in good agreement for $\mathcal{R}_{\text{cone}} = 0.5$ jets. For $\mathcal{R}_{\text{cone}} = 0.7$, Run II-B3 and II-B4 exhibit a small deviation of up to $\sim 1\%$ from the other two epochs at low energy, but this is coincident with the statistics. Therefore, we use the same response function for Run II-B1 - II-B4 by accumulating the full MC statistics. The measured MPF response was fitted using the function in Eq. 5.7 with $E_0 = 100$ GeV. The fitted parameters are summarized in Table 5.1. Fig. 5.6 compares responses in Run II-B1 and Run II-A MC samples for the two cone algorithms. As one can see, they are in agreement at high E', but differ at small energies. This difference is caused by the modified jet cone algorithm in Run II-B . My efforts demonstrated to DØ the Run II-B differences with Run II-A and the ability to combine Run II-B subranges. The final JES uses separate response corrections for Run II-A and II-B.

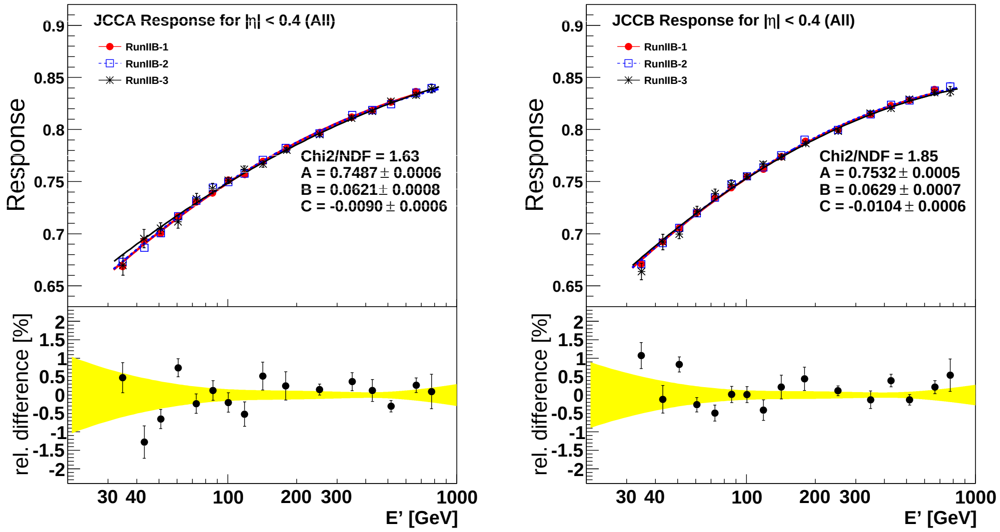

Figure 5.5. Absolute MPF response in MC for $\mathcal{R}_{\text{cone}} = 0.7$ jets (left) and for $\mathcal{R}_{\text{cone}} = 0.5$ jets (right) as a function of E'. The lines indicate the fits to the function in Eq. 5.7. The Run II-B3 and Run II-B4 MC samples are integrated as Run II-B3&4. The red points and solid line is Run II-B1, the blue squares and dashed line is Run II-B2, and the black stars and solid line is Run II-B3&4. The lower plots show the relative difference of the fitted functions between Run II-B2 and Run II-B3&4, along with the statistical uncertainty from the fit (yellow band). The JCCB jet corresponds to a jet with the cone size $\mathcal{R}_{\text{cone}} = 0.5$, and the jets with $\mathcal{R}_{\text{cone}} = 0.7$ is called JCCA.

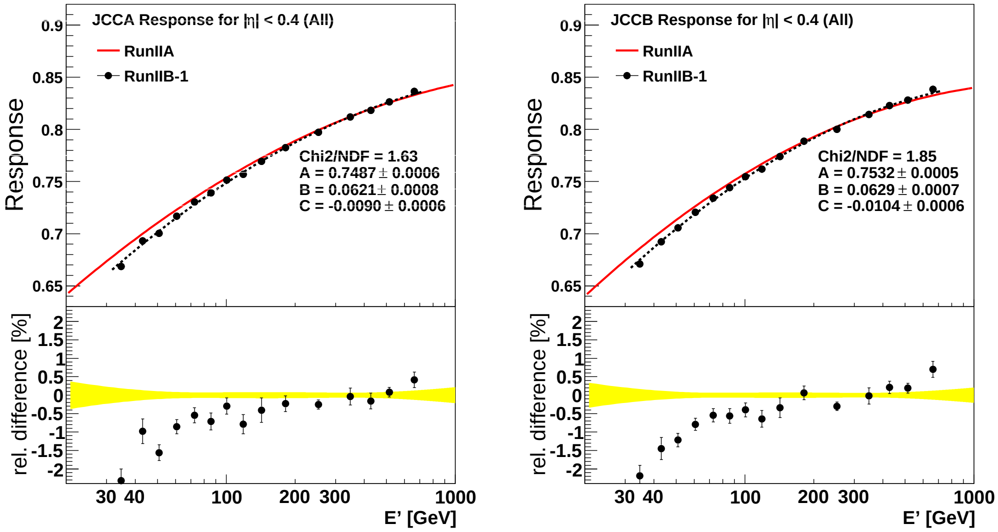

Figure 5.6. Absolute MPF response in MC for $\mathcal{R}_{\rm cone} = 0.7$ jets (left) and for $\mathcal{R}_{\rm cone} = 0.5$ jets (right) as a function of E' in Run II-B1 and Run II-A MC γ+jet samples. The lines indicate the fits to the function in Eq. 5.7. The JCCB jet corresponds to a jet with the cone size $\mathcal{R}_{\rm cone} = 0.5$, and the jets with $\mathcal{R}_{\rm cone} = 0.7$ is called JCCA. The significant discrepancy between Run II-A and II-B is corrected for in the DØ JES.

Table 5.1: Fitted parameters for the MPF response parameterization given in Eq. 5.7. Run II-A parameterization is provided for reference. The Run II-B3 and Run II-B4 MC samples are integrated as Run II-B3&4.

$\mathcal{R}_{\text{cone}}$	Epoch	p_0	p_1	p_2	χ^2/NDF
0.7	Run II-A	0.7534 ± 0.0007	0.0569 ± 0.0011	-0.0078 ± 0.0007	1.59
0.7	Run II-B1	0.7487 ± 0.0006	0.0621 ± 0.0008	-0.0090 ± 0.0006	1.63
0.7	Run II-B2	0.7490 ± 0.0007	0.0618 ± 0.0009	-0.0092 ± 0.0007	1.28
0.7	Run II-B3&4	0.7486 ± 0.0012	0.0579 ± 0.0021	-0.0068 ± 0.0012	0.65
0.5	Run II-A	0.7577 ± 0.0006	0.0580 ± 0.0009	-0.0094 ± 0.0006	1.26
0.5	Run II-B1	0.7532 ± 0.0005	0.0629 ± 0.0007	-0.0104 ± 0.0006	1.85
0.5	Run II-B2	0.7536 ± 0.0006	0.0631 ± 0.0008	-0.0105 ± 0.0006	1.93
0.5	Run II-B3&4	0.7530 ± 0.0010	0.0615 ± 0.0018	-0.0099 ± 0.0011	1.49

5.1.4. Relative MPF Response Correction

The DØ calorimeter has a non-uniform response to jets with respect to η^{det} due to geometrical construction (e.g. CC and EC) and embedded materials. The jet response in the CC cryostat is rather uniform, while in EC it is approximately 15% (10%) lower than the CC response in data (MC). Inside the inter-cryostat region ($0.8 < |\eta^{det}| < 1.6$), the poor instrumentation causes additional non-uniformity. A substantial amount of energy is lost in the solenoid, cryostat walls, module end-plates and support structures in this region. In particular, the $0.8 < |\eta^{det}| < 1.2$ region has the largest deviation in energy dependence of response with respect to CC, due to the limited sampling of the jet energy and significant losses in dead material. The $1.2 < |\eta^{det}| < 1.6$ region is not covered by the electromagnetic calorimeter and the total depth drops below 6 radiation lengths. The goal of relative MPF response correction is to correct for all these effects and calibrate forward jets with respect to the central ones ($|\eta^{det}| < 0.4$), which are already calibrated in the absolute response correction.

The same MPF method was applied as in the case of absolute response. Both γ+jet and dijet samples are used in the determination of relative response correction. The γ+jet sample allows a consistent derivation of the response relative to the central calorimeter, but lacks statistics in high p_T region. The dijet sample can reach higher p_T regions than the γ+jet events. A combination of the two samples is able to reduce both statistical and systematic uncertainties.

5.1.4.1. Event Selection

The γ+jet event selection is identical to the absolute MPF response determination, with the exception that the probe jet is not restricted to the central calorimeter.

The dijet event selection is similar to the γ+jet event selection, with one of the two jets replacing the role of photon but without central correction applied. The primary vertex (PV) requirement is $0 <$ number of PVs ≤ 4. We require exactly two back-to-back ($\Delta\phi > 3.0$) reconstructed jets with $\mathcal{R}_{\rm cone} = 0.7$ or 0.5. At least one of the jets must be in the region $|\eta^{det}| \leq 0.4$ to have its core well contained inside CC. This jet serves as the tag object and the other jet is the probe. The two tag and probe assignments are both considered when both jets are in the $|\eta^{det}| \leq 0.4$ region. The uncorrected p_T of the tag jet is required to be large enough to avoid bias from the triggers, with the efficiency of the trigger for such jets to be above 98%. To remove cosmic-ray muons, we reject events with cosmic ray candidates, or with a ratio of $\not{E}_{\rm T}$ over the p_T of the most energetic jet that is greater than 0.7.

5.1.4.2. Method

To examine the expected $\eta^{\rm det}_{\rm jet}$ dependence at fixed p_T, a (E', $\eta^{\rm det}_{\rm jet}$)-based variable, $p'_{\rm T}$ is introduced, defined as:

$$p'_{\rm T} \equiv \frac{E'}{\cosh(\eta^{\rm det}_{\rm jet})}, \tag{5.8}$$

where, in the case of γ+jet events, E' is given by Eq. 5.6. In terms of p'_{T}, Eq. 5.7 can be rewritten as:

$$R(\eta^{\mathrm{det}}_{\mathrm{jet}}; p'_{\mathrm{T}}) = \hat{p}_0(p'_{\mathrm{T}}) + \hat{p}_1(p'_{\mathrm{T}}) \log\left(\cosh\left(\eta^{\mathrm{det}}_{\mathrm{jet}}\right)\right) + \hat{p}_2(p'_{\mathrm{T}}) \log^2\left(\cosh\left(\eta^{\mathrm{det}}_{\mathrm{jet}}\right)\right), \quad (5.9)$$

where $\hat{p}_0$, $\hat{p}_1$ and $\hat{p}_2$ are fit parameters. The η-dependent correction is derived in 66 η^{det} bins that cover a wide region $|\eta^{\mathrm{det}}| < 3.6$. The bin width is 0.1 in the region $|\eta^{\mathrm{det}}| < 1.0$ and $1.8 < |\eta^{\mathrm{det}}| < 2.0$, refined to 0.05 in $1.0 < |\eta^{\mathrm{det}}| < 1.8$ for better sampling of the ICD region. For the region $2.0 < |\eta^{\mathrm{det}}| < 3.6$, 5 bins are created with bin width of 0.2 for the innermost three bins, and 0.4 for the outermost two bins.

An η-dependent correction factor F_η was measured from the data and MC in each η^{det} bin. For γ+jet events, the relative MPF response in a given $(p'_{\mathrm{T}}, \eta^{\mathrm{det}}_{\mathrm{jet}})$ is given as:

$$F_\eta^{\gamma\,+\,\mathrm{jet}} = \frac{R_{\mathrm{MPF},\eta}|_{p'_{\mathrm{T}}}}{R^{\gamma\mathrm{+jet}}_{\mathrm{MPF,CC}}(\eta^{\mathrm{det}}_{\mathrm{jet}}; p'_{\mathrm{T}})}. \quad (5.10)$$

where the denominator represents the MPF response as measured in CC, extrapolated to η^{det} with Eq. 5.9. In data, due to the contamination by dijet events and the imperfect calibration of the photon energy, even for $|\eta^{\mathrm{det}}| \leq 0.4$, this ratio is slightly smaller than one. The background correction, including photon purity and dijet contamination, is not applied in this stage but eventually accounted for in the global fit (see Sec. 5.1.4.4) to the full set of measurements. Finally, $F_\eta^{\gamma\,+\,\mathrm{jet}}$ measured in $(p'_{\mathrm{T}}, \eta^{\mathrm{det}}_{\mathrm{jet}})$ coordinates is mapped to $(E', \eta^{\mathrm{det}}_{\mathrm{jet}})$ coordinates. I derived $F_\eta^{\gamma\,+\,\mathrm{jet}}$ as a function of E' in two different η^{det} bins as shown in Fig. 5.7 and 5.8 as solid circles.

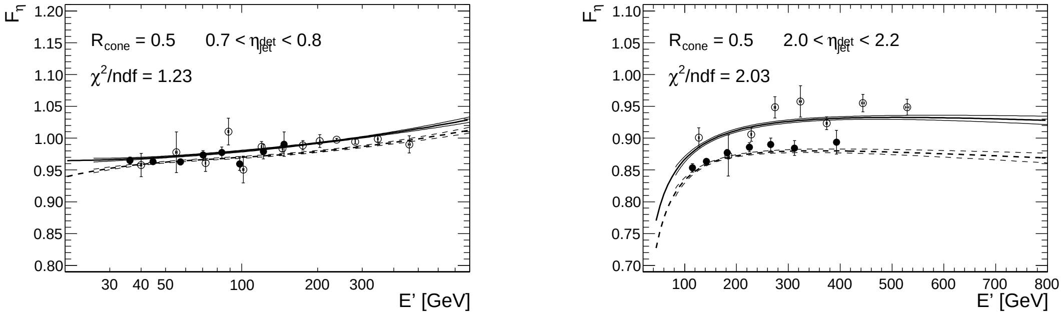

Figure 5.7. Relative MPF response correction for $\mathcal{R}_{\text{cone}} = 0.5$ jets in Run II-B2 data as a function of E' in two $\eta_{\text{jet}}^{\text{det}}$ bins. The solid (open) circles represent the measurements in the $\gamma + \text{jet}$ (dijet) sample. The lines shown represent the global fit function.

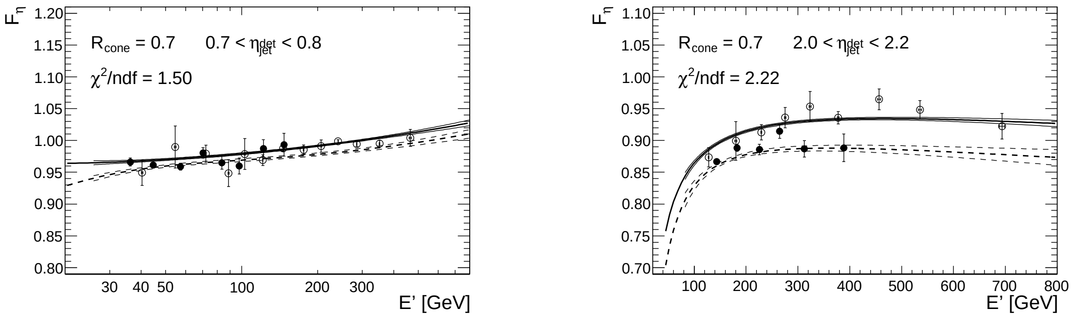

Figure 5.8. Relative MPF response correction for $\mathcal{R}_{\text{cone}} = 0.7$ jets in Run II-B2 data as a function of E' in two $\eta_{\text{jet}}^{\text{det}}$ bins. The solid (open) circles represent the measurements in the $\gamma + \text{jet}$ (dijet) sample. The lines shown represent the global fit function.

Due to the presence of an uncalibrated tag jet, the derivation of F_η from the dijet sample is more complicated. Both the average relative MPF response and E' need to be corrected for the resolution bias. In addition, E' also needs to be corrected by the absolute jet energy extracted in Sec. 5.1.2. The relative MPF response correction in a given $(p'_{\mathrm{T}}, \eta_{\mathrm{jet}}^{\mathrm{det}})$ region is computed similar to Eq. 5.10:

$$F_\eta^{\mathrm{dijet}} = r_{E'} \frac{R_{\mathrm{MPF},\eta}^{\mathrm{dijet}} R_{\mathrm{MPF,CC}}^{\gamma+\mathrm{jet}}(\eta_{\mathrm{jet}}^{\mathrm{det}} = 0;)}{R_{\mathrm{MPF,CC}}^{\gamma+\mathrm{jet}}(\eta_{\mathrm{jet}}^{\mathrm{det}};)}, \tag{5.11}$$

where $r_{E'}$ is a residual factor that corrects for the difference in response between γ+jet and dijet samples. Similar to $F_\eta^{\gamma\,+\,\mathrm{jet}}$, F_η^{dijet} measured in $(p'_{\mathrm{T}}, \eta_{\mathrm{jet}}^{\mathrm{det}})$ coordinates is also mapped to the $(E', \eta_{\mathrm{jet}}^{\mathrm{det}})$ coordinates. The open circles in Fig. 5.7 and 5.8 illustrate the measured F_η^{dijet} as a function of E' in two different η^{det} bins.

5.1.4.3. Sample-dependence of the relative MPF response

As shown in Fig. 5.7 and 5.8, the measured F_η is different between the γ+jet and dijet samples, particularly at large rapidities. The main reason for this discrepancy is the different parton flavor composition of the two samples. The leading jet in γ+jet sample is dominated by quarks at low energy and gluons at high energy, while it is opposite in the dijet sample. Since the fragmentation of gluon jets is softer, the expected response of gluon jets is lower than quark jets, resulting in a larger difference between dijet sample and γ+jet sample for the forward jets.

In a given η^{det} region, the ratio $F_\eta^{\mathrm{dijet}}/F_\eta^{\gamma\,+\,\mathrm{jet}}$ is nearly independent of E'. Therefore, we can define the "dijet-to-γ+jet scale factor" as:

$$SF_\eta \equiv \frac{F_\eta^{\mathrm{dijet}}(E')}{F_\eta^{\gamma+\mathrm{jet}}(E')}, \tag{5.12}$$

which is the key parameter to combine both samples.

5.1.4.4. Global fit

A global fit to all F_η measurements is performed in order to provide a smooth correction in jet energy and pseudorapidity. In every particular bin in detector η, a quadratic logarithmic E' dependence is assumed:

$$F_\eta^{\gamma\,+\,\mathrm{jet}}(E',\eta) = \frac{R^{\gamma+\mathrm{jet}}_{\mathrm{MPF},\eta}(E')}{R^{\gamma+\mathrm{jet}}_{\mathrm{MPF,CC}}(E')} = \frac{p_{0,\eta} + p_{1,\eta}\log(E'/E_0) + p_{2,\eta}\log^2(E'/E_0)}{R^{\gamma+\mathrm{jet}}_{\mathrm{MPF,CC}}(E')}. \tag{5.13}$$

Following Eq. 5.12, the relative MPF response correction in the dijet sample is defined as:

$$F_\eta^{\mathrm{dijet}}(E',\eta,S_\eta) = S_\eta F_\eta^{\gamma\,+\,\mathrm{jet}}(E',\eta). \tag{5.14}$$

In each of the 66 bins in η^{det}, $F_\eta^{\gamma\,+\,\mathrm{jet}}$ and F_η^{dijet} are parameterized as dependent on the four parameters: p_0, p_1, p_2 and S_η. These parameters can be estimated from a simultaneous fit (“global fit”) to all $\gamma+\mathrm{jet}$ and dijet data points (See Fig. 5.9). The scale factor S_η is described by:

$$SF_\eta = 1 + b\log\left(\cosh(\eta^{\mathrm{det}}_{\mathrm{jet}})\right) + c\log^2\left(\cosh(\eta^{\mathrm{det}}_{\mathrm{jet}})\right). \tag{5.15}$$

The results for the η-dependent corrections for $\mathcal{R}_{\mathrm{cone}} = 0.5$ ($\mathcal{R}_{\mathrm{cone}} = 0.7$) are summarized in Figs. 5.10, 5.11, 5.12 and 5.13 for the $\gamma+\mathrm{jet}$ and the dijet samples. As a result of the new ICD calibration, the Run II-B correction is much smoother than the Run II-A correction. The new correction also exhibits less energy dependence which might be caused by using more appropriate sampling weights for the electromagnetic layers of the calorimeter.

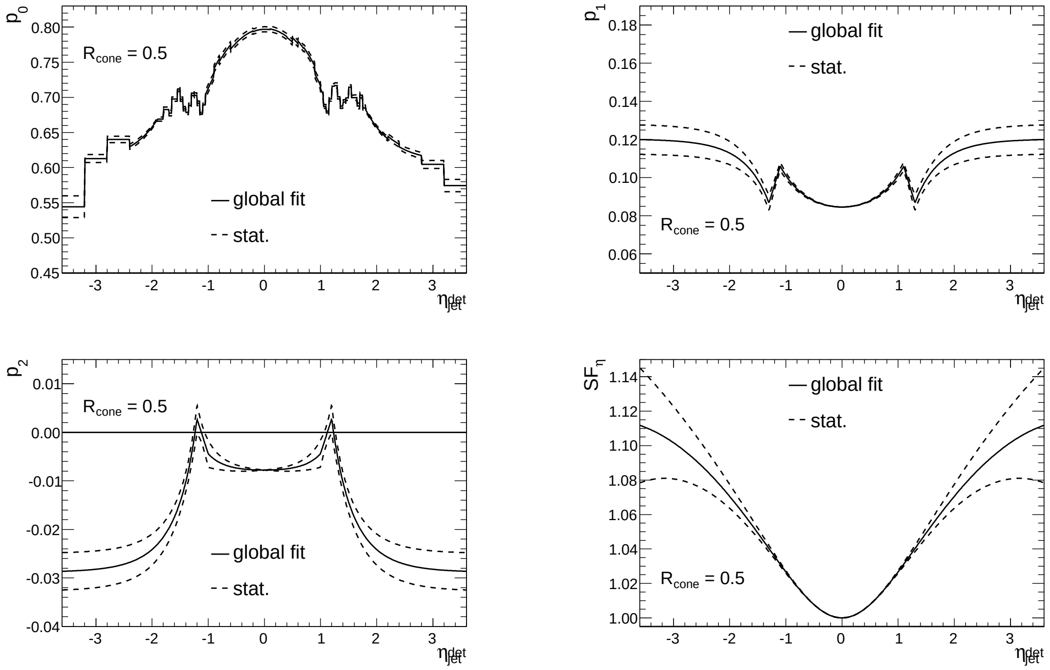

Figure 5.9. F_η parameters (Eqs. 5.13 and 5.14) as function of $\eta^{\rm det}$ for Run II-B1 data and $\mathcal{R}_{\rm cone} = 0.5$; dashed bands represent the statistical uncertainty.

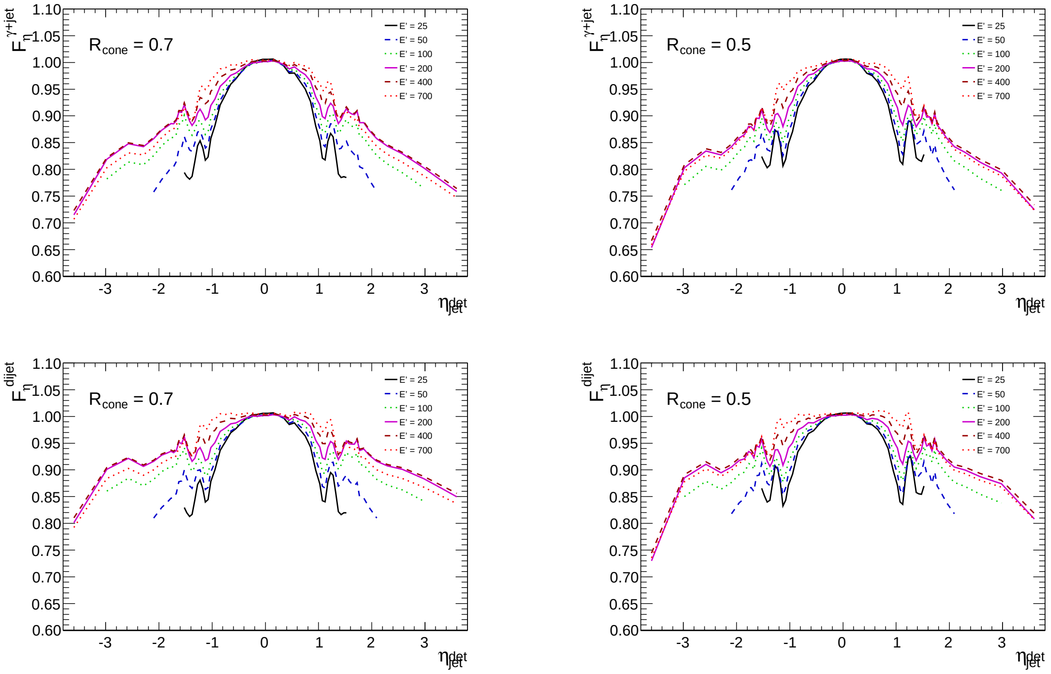

Figure 5.10. Relative MPF response correction in Run II-B1 data for $\mathcal{R}_{\text{cone}} = 0.7$ jets (left) and $\mathcal{R}_{\text{cone}} = 0.5$ jets (right) as a function of $\eta_{\text{jet}}^{\text{det}}$, separately for $\gamma + \text{jet}$ (up) and dijet (down). The different lines correspond to particular E' value.

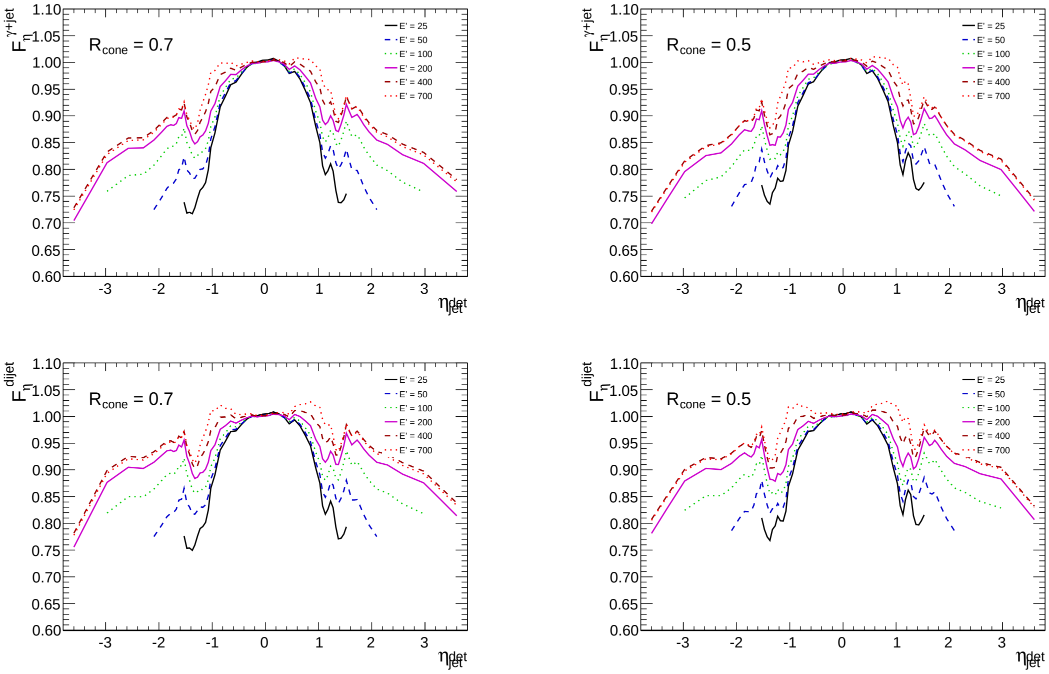

Figure 5.11. Relative MPF response correction in Run II-B2 data for $\mathcal{R}_{\mathrm{cone}} = 0.7$ jets (left) and $\mathcal{R}_{\mathrm{cone}} = 0.5$ jets (right) as a function of $\eta_{\mathrm{jet}}^{\mathrm{det}}$, separately for $\gamma + \mathrm{jet}$ (up) and dijet (down). The different lines correspond to particular E' value.

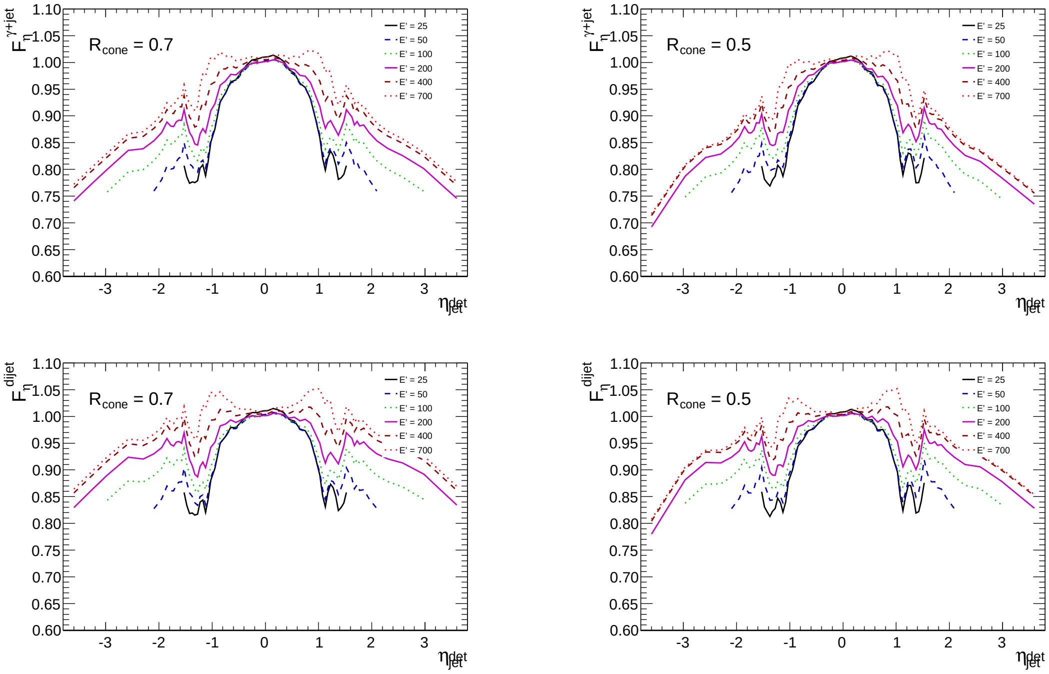

Figure 5.12. Relative MPF response correction in Run II-B3 data for $\mathcal{R}_{\text{cone}} = 0.7$ jets (left) and $\mathcal{R}_{\text{cone}} = 0.5$ jets (right) as a function of $\eta_{\text{jet}}^{\text{det}}$, separately for $\gamma + \text{jet}$ (up) and dijet (down). The different lines correspond to particular E' value.

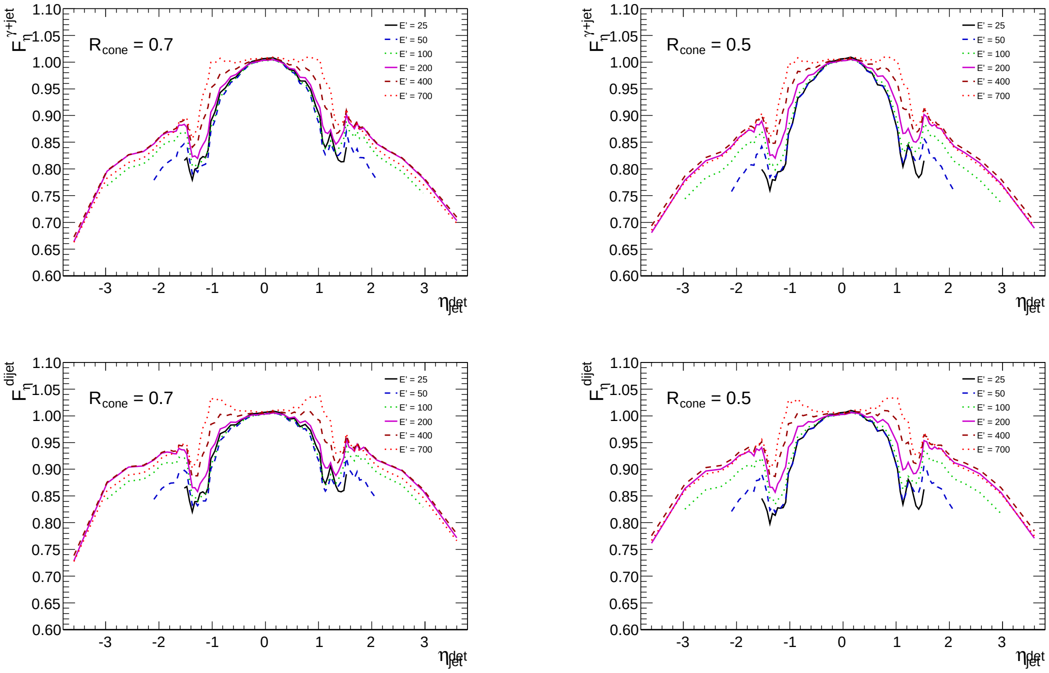

Figure 5.13. Relative MPF response correction in Run II-B4 data for $\mathcal{R}_{\text{cone}} = 0.7$ jets (left) and $\mathcal{R}_{\text{cone}} = 0.5$ jets (right) as a function of $\eta_{\text{jet}}^{\text{det}}$, separately for $\gamma +$ jet (up) and dijet (down). The different lines correspond to particular E' value.

5.1.4.5. Closure

In order to check how well the parametrized jet corrections correct the jet energies, I perform an internal closure test in wider bins spanning 0.4 units in pseudorapidity in order to achieve a higher statistical precision. In the closure test, the $\not{E}_{\text{T}}$ in the data that is used in the MPF formula is firstly corrected according to the relative MPF correction from the global fit, and then the relative MPF correction is remeasured. If our formulation of the MPF correction works well, the residual correction should be consistent with unity.

Fig. 5.14 shows an example for the closure test with $\mathcal{R}_{\text{cone}} = 0.5$ jets. An additional uncertainty (green band in Fig. 5.14) is added to the relative MPF correction to cover the presence of residual F_η.

The residual uncertainty is small in CC where the correction factor is close to 1 and it becomes sizable in the ICD and very forward region where corrections are large. Even in these regions, the test shows that the global fit is controlled with a precision better than 2%.

5.1.4.6. Uncertainties

The overall uncertainty including the contribution from the central response (statistical and photon energy scale) is summarized for $\mathcal{R}_{\text{cone}} = 0.5$ ($\mathcal{R}_{\text{cone}} = 0.7$) in Fig. 5.15 (Fig. 5.16) both for the $\gamma + \text{jet}$ and the dijet samples, for $p'_{\text{T}} = 50\,\text{GeV}$. In the $\gamma + \text{jet}$ sample, the total uncertainty is less than 1.6% for $|\eta^{\text{det}}| < 2.8$ and central response uncertainties dominate the total uncertainty in $2.0 < |\eta^{\text{det}}| < 3.2$. In the dijet sample the total uncertainty is similar to $\gamma + \text{jet}$, which is less than 1.4% for $|\eta^{\text{det}}| < 2.8$ but for $2.0 < |\eta^{\text{det}}| < 3.2$ the central response is not significantly dominating the total uncertainty as in $\gamma + \text{jet}$ sample.

5.1.5. Flavor Dependent Jet Response Correction

As discussed in Sec. 5.1.5, we determine the general JES correction at DØ from the γ+jet sample and extrapolate it to high energy region using dijet sample. Since jets can be initiated from partons of different flavors, and the particle composition can be different for different flavors of jets, the jet response is dependent on these characteristics [76]. For instance, in non-compensating calorimeters, the electromagnetic particles have higher response than the hadronic particles ($e/h > 1$), which will result in different response for b jets and light quark jets as their electromagnetic and

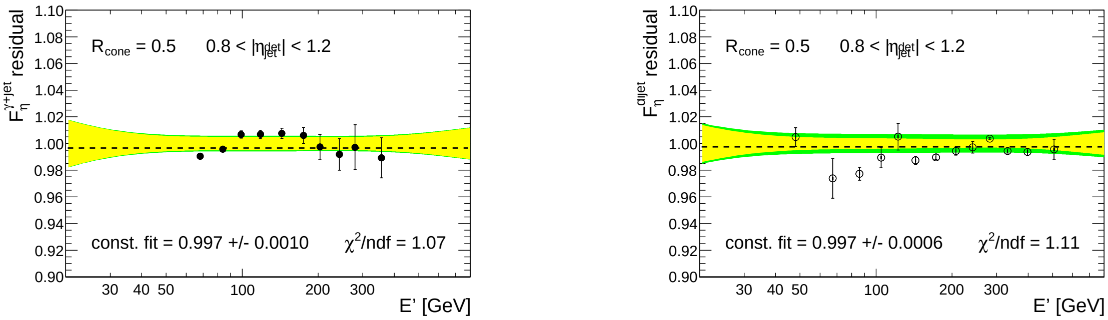

Figure 5.14. Residual F_η for $\mathcal{R}_{\text{cone}} = 0.5$ jets in Run II-B2 data as a function of E' in two $\eta_{\text{jet}}^{\text{det}}$ bins. This closure test is performed separately for (left) $\gamma+\text{jet}$ and (right) dijet samples. The yellow band represents statistical uncertainty and the green band represents residual uncertainty.

hadronic fractions are different. More importantly, their particle multiplicity is also different. These result in a need for a flavor-dependent correction to the jet energies.

The flavor corrections for data and MC are derived separately using single particles responses appropriate to each. The MC single particle responses are derived for γ, $e^{\pm}$, $\mu^{\pm}$, $\pi^{\pm}$, $K^{\pm}$, K_0^S, K_0^L, $p^{\pm}$, n, and Λ from Run II-B single particle MC samples with all the zero suppression, calorimeter noise and zero bias overlay turned off. For data, the photon, electron and muon responses are considered to be identical to corresponding MC single particle responses under the assumption that the single particle MC has a very good simulation of the EM component of the calorimeter and the muon interaction with the detector. For hadrons, parameterizations are introduced to account for the difference between the corrected MC responses and data. A ratio is formed from both corrections and applied to MC to make it agree with data. In MC, each detector-level jet is spatially matched to a particle-level jet

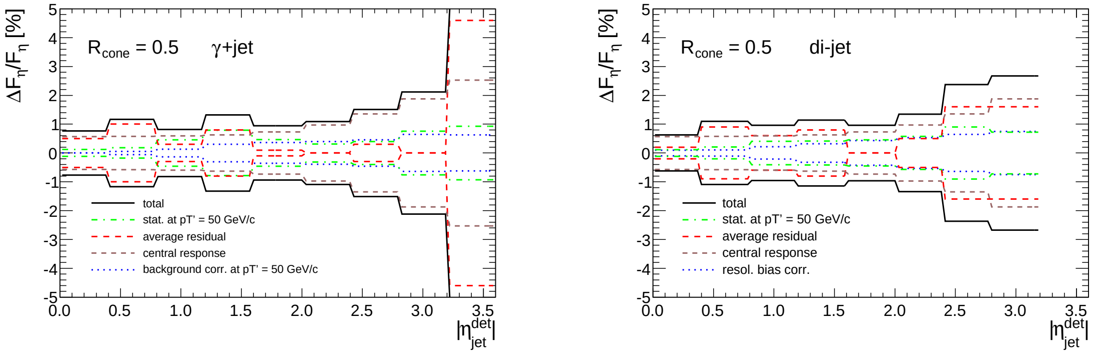

Figure 5.15. Relative uncertainty on relative MPF correction for $\mathcal{R}_{\text{cone}} = 0.5$ jets from $\gamma+$jet (left) and dijet (right) sample in Run II-B2 data.

to calculate a correction factor F [77] [78]:

$$F = \frac{\sum_i E_i \cdot R_i^{Data}}{\sum_i E_i \cdot R_i^{MC}}, \tag{5.16}$$

where the subscript i runs over all the particles in the particle jet, E_i are the energies of the particles, and R_i^{Data} (R_i^{MC}) are the single particle responses in data (MC). To normalize this correction to the absolute energy scale as measured in γ+jet events, the average of this correction in the γ+jet sample is calculated ($\langle F^{\gamma+jet}\rangle$) and a scale factor is constructed as follows:

$$F_{corr} = \frac{\frac{\sum_i E_i \cdot R_i^{data}}{\sum_i E_i \cdot R_i^{MC}}}{\langle F^{\gamma+jet}\rangle}. \tag{5.17}$$

$\langle F^{\gamma+jet}\rangle$ is parameterized without any JES correction applied. As shown in Figures 5.17and 5.18, F_{corr} is derived for 3 categories of jets: light quark jets, gluon jets and b jets. Eq. 5.17 corrects for the MC-data difference in the jet response due to parton flavor and is applied to the jet energy after the offset correction, i.e.:

$$(E_{jet}^{raw} - E_O)F_{corr} = (E_{jet}^{raw} - E_O)\frac{\frac{\sum_i E_i \cdot R_i^{data}}{\sum_i E_i \cdot R_i^{MC}}}{\langle F^{\gamma+jet}\rangle}, \tag{5.18}$$

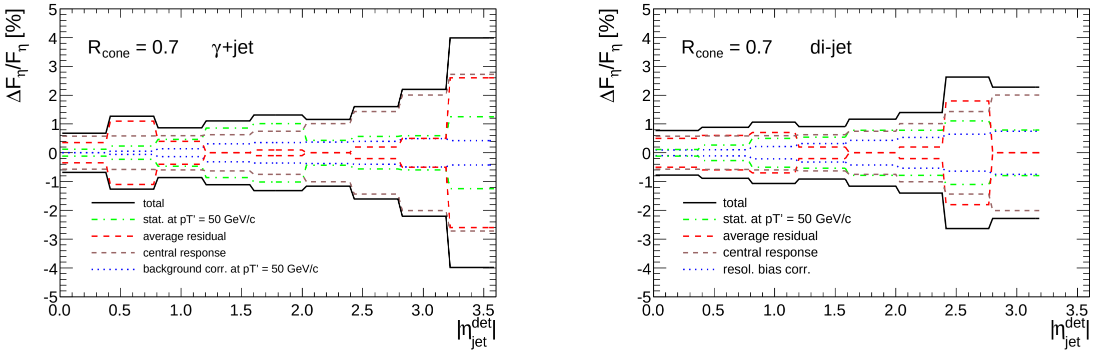

Figure 5.16. Relative uncertainty on relative MPF correction for $\mathcal{R}_{\text{cone}} = 0.7$ jets from $\gamma +$jet (left) and dijet (right) sample in Run II-B2 data.

where E_{jet}^{raw} is the uncorrected jet energy, E_O is the offset correction for noise, pile-up and multiple interactions. This correction is independent of other JES corrections (response, showering, etc), and Eq. 5.17 is integrated into the standard correction procedure by:

$$E_{jet}^{corr} = \frac{(E_{jet}^{raw} - E_O)F_{corr}}{F_\eta RS}, \tag{5.19}$$

5.2. Additional absolute JES from ℓ+jets

The $\gamma + jet$ response sets the floor on the total JES due to irreduciable systematic uncertainties at approximately 1% level. Therefore the dominant source for analyses that rely on the precision of measured jets is usually from the jet energy scale. At DØ, a solution is found by applying additional correction to the jet energy to reduce the JES uncertainty in top quark mass measurement [79].

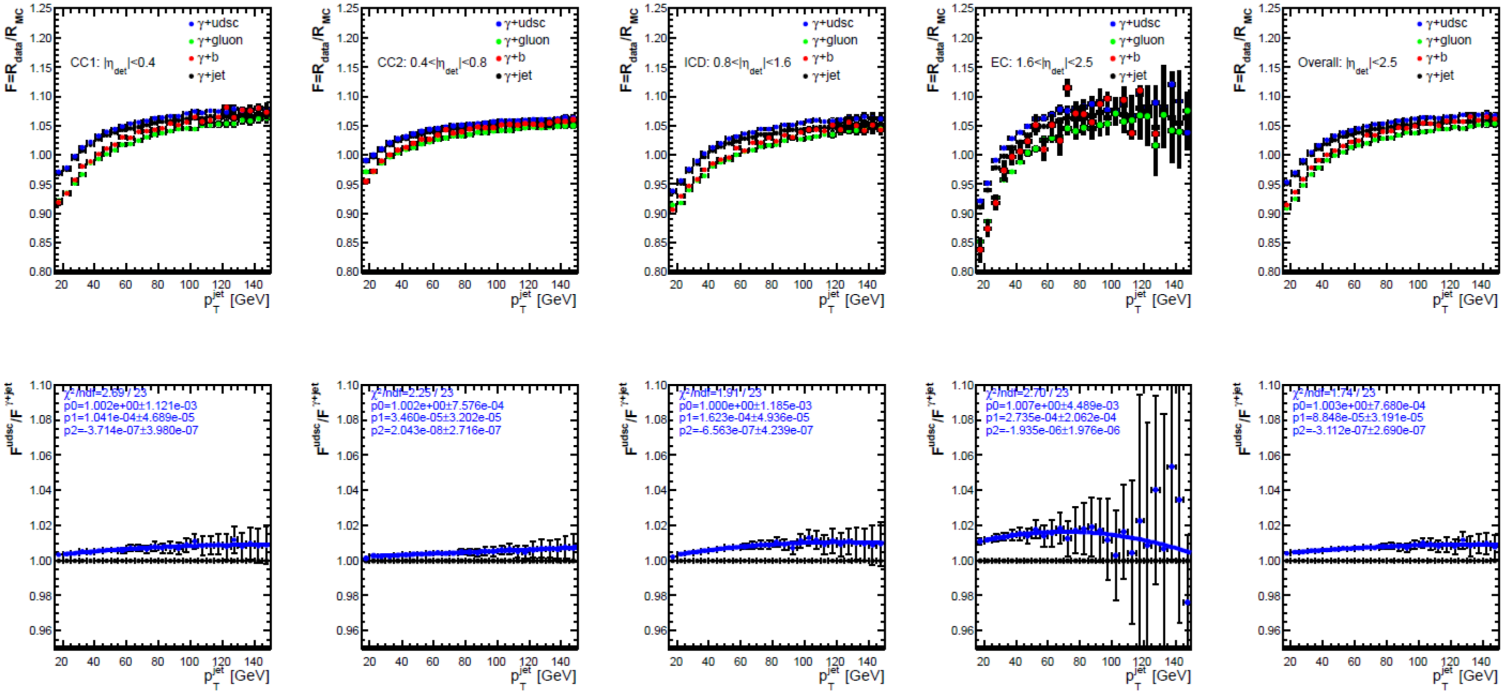

Figure 5.17. MC-data correction factor F estimated for jets with different flavors in γ+jet MC samples. The MC single particle responses used here are extracted from the single particle MC samples with Zero Suppression turned off. Top: the correction factor $F(=R_{data}/R_{MC})$ for light flavor quark jets (blue), gluon jets (green), b quark jets (red) and the averaged F for the γ+jets sample (black). Bottom: the ratio between F for light quark jets and the averaged F for the γ+jets sample.

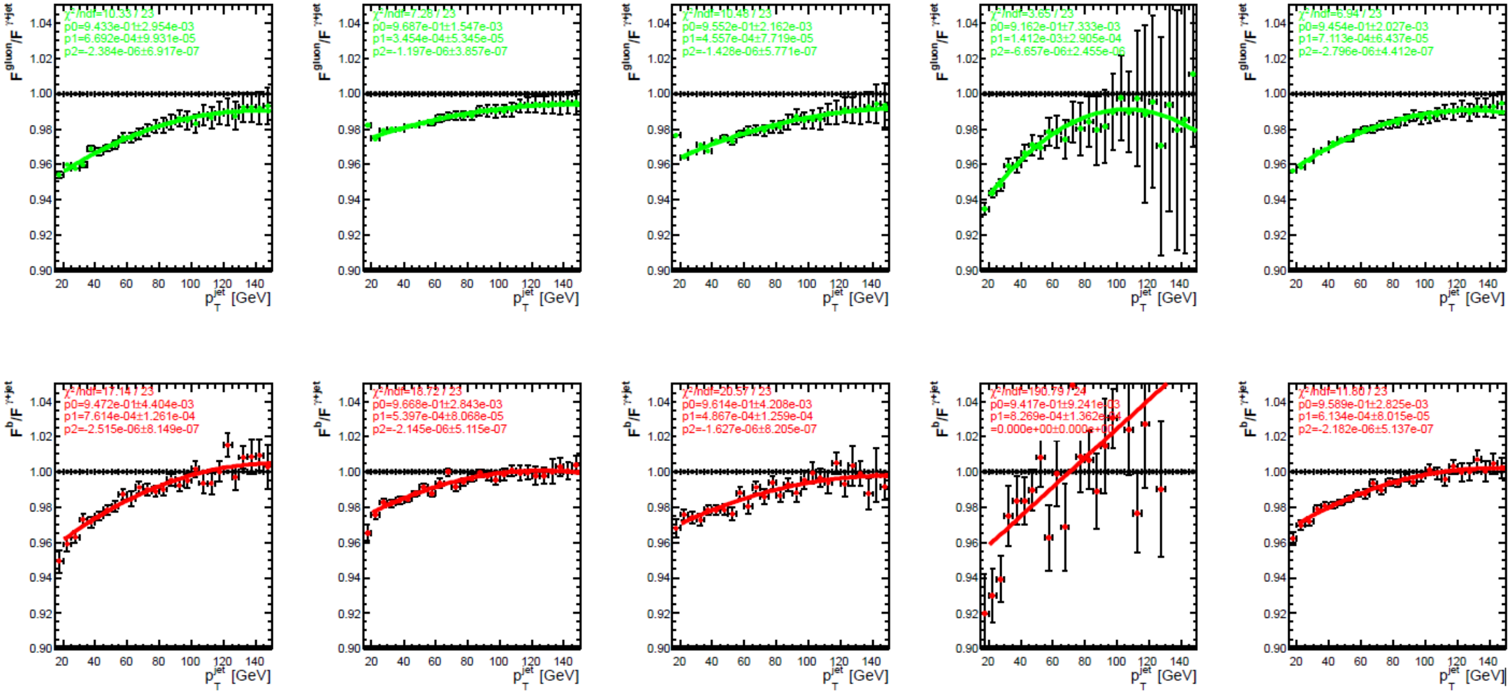

Figure 5.18. MC-data correction factor F estimated for jets with different flavors in γ+jet MC samples. The MC single particle responses used here are extracted from the single particle MC samples with Zero Suppression turned off. Top: the ratio between F for gluon jets and the averaged F for the γ+jets sample. Bottom: the ratio between F for b quark jets and the averaged F for the γ+jets sample.

5.2.1. ℓ+jets Jet Energy Scale Correction

In ℓ+jets top quark mass measurement, an additional adjustment to the jet energy is introduced in-situ during the analysis and is denoted as k_{JES}. This additional JES factor enters the Matrix-Element (ME) calculation through a Transfer Function (TF) $W_{jet}(E_x, E_y; k_{JES})$ [80] that calculates the probability of a partonic level jet E_y to be reconstructed as a jet with energy E_x. The formulation of $W_{jet}(E_x, E_y; k_{JES})$ takes two steps: (i) suppose k_{JES}=1, then TF is parameterized as:

$$\begin{aligned} TF(E_x, E_y) = & \frac{1}{\sqrt{2\pi}(p_2 + p_3 p_5)} \times \\ & \times [exp(-\frac{((E_x - E_y) - p_1)^2}{2p_2^2}) + p_3 exp(-\frac{((E_x - E_y) - p_4)^2}{2p_5^2})], \end{aligned} \tag{5.20}$$

where p_i are parameterized as linear functions of the quark energy:

$$P_i = a_i + E_y b_i. \tag{5.21}$$

Then k_{JES} is imported to correct the reconstructed jet of energy E_x to particle level as follows:

$$W_{jet}(E_x, E_y; k_{JES}) = \frac{TF(\frac{E_x}{k_{JES}}, E_y)}{k_{JES}}, \tag{5.22}$$

where the k_{JES} in the denominator is a normalization factor to make the integral of $W_{jet}(E_x, E_y; k_{JES})$ over E_x as 1. k_{JES} is applied to all the jets in ℓ+jets $t\bar{t}$events where 2 b jets come from top quark decay and 2 light quark jets come from 1 hadronically decayed W boson, $W \to q\bar{q}'$. By constraining the invariant mass of the candidate dijet pair to the world average value of the W boson mass $m_W = 80.385$ GeV, k_{JES} can be determined within very small statistical uncertainty. Both k_{JES} and m_t are derived from a two-dimensional likelihood function [80] as shown in Fig. 5.19. The new k_{JES} from 9.7 fb^{-1} of data is $k_{JES} = 1.0250 \pm 0.0046$ [81].

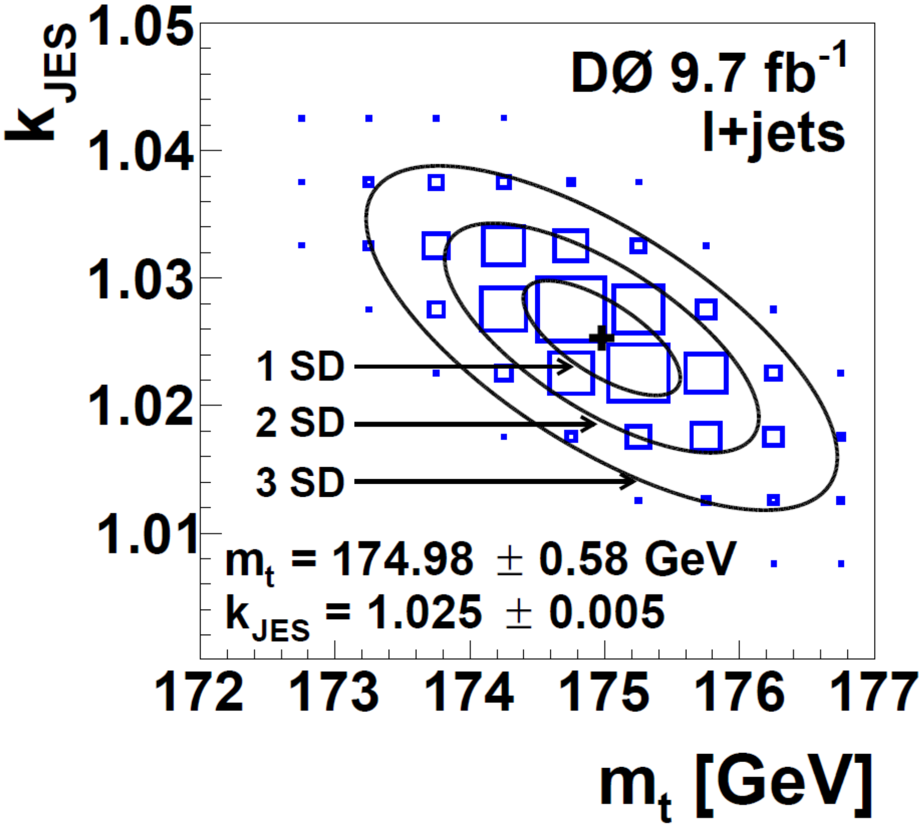

Figure 5.19. Fitted Gaussian contours of equal probability for the two-dimensional likelihoods as a function of m_t and k_{JES}. The counters correspond to a 1-σ, 2-σ, and 3-σ statistical uncertainty on m_t.

An earlier version of this factor was used as a calibration for the first time in the analysis of 4.3 fb^{-1} [82] When carrying over the ℓ+jets JES to the $t\bar{t}$ dilepton channel, the difference between the b jets in the two channels should be considered. The primary difference is event topology between the two samples. The jet multiplicity is higher in the ℓ+jets channel than in the dilepton channel. In the ℓ+jets channel, the hadronically decayed W boson produces a color dipole of two light quarks, where more radiation is emitted in between the two quarks during showering process. This non-uniform dipole radiation complicates jet reconstruction and affects jet energies. On the other hand, the b jets in the ℓ+jets channel could also overlap with the light quark jets, resulting in about ∼3% more particles in the ℓ+jets channel b jet [83].

The slight difference in particle multiplicity between b jets in the two channels can produce a sub-percent shift in JES. We estimate the difference between the b quark JES in the two channels by calculating a *double ratio*, using the single particle responses described in Section 5.1.5:

$$\mathcal{R}^b_{2\ell}(p^b_T) = \frac{R^{2\ell}_{data}(p^b_T)/R^{2\ell}_{MC}(p^b_T)}{R^{\ell+jets}_{data}(p^b_T)/R^{\ell+jets}_{MC}(p^b_T)}, \tag{5.23}$$

where $R^{2\ell}_{data}$ and $R^{2\ell}_{MC}$ are the b jet energy response for MC and data sample in the dilepton channel, $R^{\ell+jets}_{data}$ and $R^{\ell+jets}_{MC}$ are the respective responses for the ℓ+jets channel. Plugging in Eq. 5.17, the double ratio can be expressed as:

$$\mathcal{R}^b_{2\ell}(p^b_T) = \frac{F^{dilepton}_{corr}(p^b_T)}{F^{\ell+jets}_{corr}(p^b_T)}, \tag{5.24}$$

where $F^{dilepton}_{corr}(p^b_T)$ and $F^{\ell+jets}_{corr}(p^b_T)$ are flavor dependent corrections for dilepton b jets and ℓ+jets b jets, respectively. The double ratio as a function of b jet transverse momentum is shown in Figure 5.20.

We fit a constant value to the double ratio for $p^b_T > 60$ GeV to avoid contamination from b jet confusion with light quark jets from Ws in the ℓ+jets channel. As shown

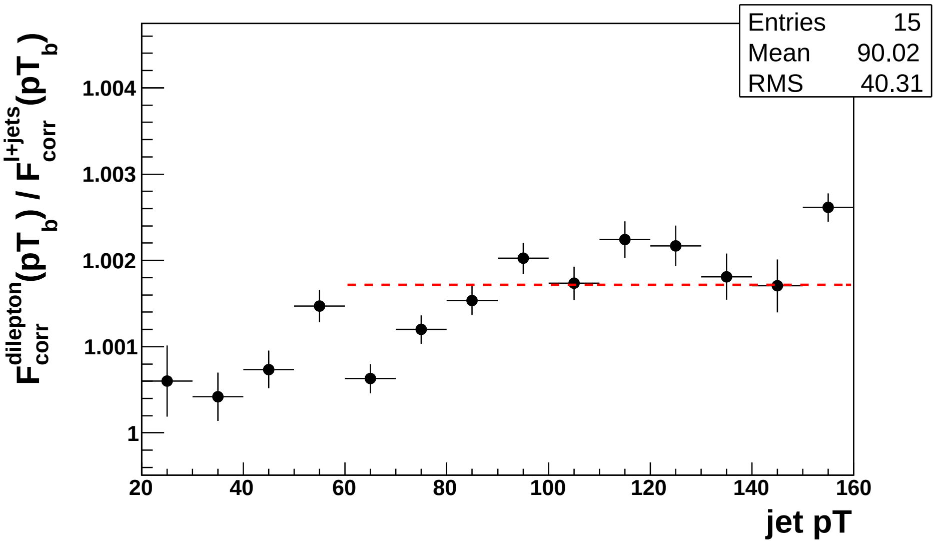

Figure 5.20. The double ratio, $R_{2\ell}^{b}$, is plotted vs b jet transverse momentum. The value of the double ratio in each bin is shown with corresponding error bars reflecting the uncertainty. Dashed line is the fitted value of the double ratio above 60 GeV.

in Figure 5.20, the double ratio ranges from 1.0005 to 1.0026 for $p_T^b > 60$ GeV, and the fit is shifted from unity by a small deviation of 0.17% with a statistical uncertainty of 6.1×10^{-5}. The ∼3% relative difference of b jet particle number is large enough to cause such a shift. The fact of this difference being small is an indication that the ℓ+jets b jets are very similar to the dilepton b jets. It does not necessitate a systematic uncertainty since the DØ flavor dependent correction described in Section 5.1.5 considers each jet particle content individually.

We apply the central value of ℓ+jets JES k_{JES} to our b jets and estimate the JES systematic uncertainty from the statistical uncertainty of k_{JES}. The residual effects due to p_T and η dependence of k_{JES} is considered a systematic uncertainty, which is discussed in Chapter 8.

Chapter 6

THE TOP MASS EXTRACTION METHOD

The final state of dilepton events contains two undetectable neutrinos. The vector sum of the two neutrinos' transverse momenta can be measured as the imbalance in the event transverse momentum ($\not\!\!E_{\mathrm{T}}$). However, the loss of knowledge of four components of momentum means the event is underconstrained. A solution is found by scanning a range of top quark masses and neutrino rapidities and comparing the solved neutrino momentum in each case to the measured $\not\!\!E_{\mathrm{T}}$. A template method is employed to extract the top quark mass and its statistical uncertainty.

This chapter discusses the kinematic reconstruction of the dilepton event, the construction of templates, as well as the maximum likelihood technique. The calibration of the method is discussed at the end of this chapter.

6.1. Kinematic Reconstruction

As shown in Fig. 6.1, the $t\bar{t}$ dilepton final state consists of six outgoing particles: two oppositely charged leptons, two jets originating from b quarks, and two neutrinos. Since the masses of each b quark, W boson and all leptons are known with uncertainties much smaller than the world average value of the top quark mass, we parameterize the kinematic reconstruction using the world average values of all involved final-state particles' masses as inputs. We ignore the negligible neutrino mass in the dilepton event reconstruction. In the dilepton final state, there are $6 \times 4 = 24$ independent kinematic variables from the six particles. The known masses of outgoing particles can exclude 6 degrees of freedom (d.o.f.). Twelve more d.o.f can be constrained by the

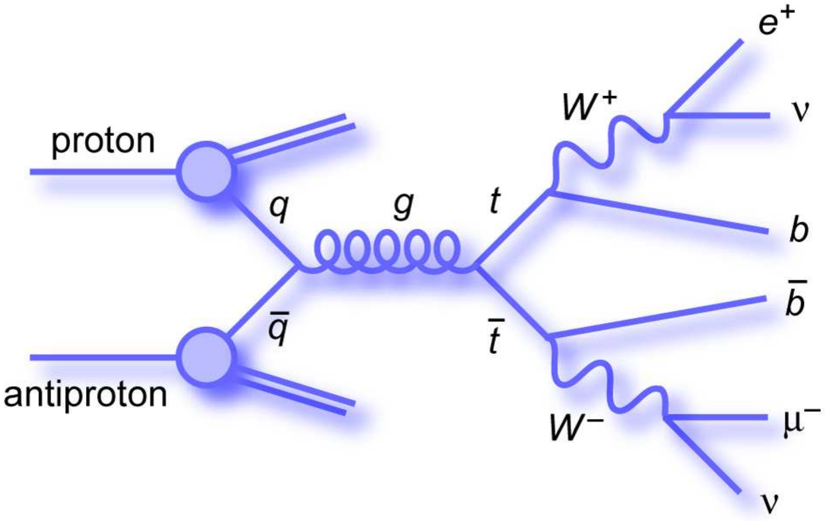

Figure 6.1. Illustration of the $e\mu$ channel in $t\bar{t}$ final states produced in $p\bar{p}$ hard-scattering process.

kinematics of leptons and jets that are measured through their energy deposition in the calorimeters. Six momentum components of the two neutrinos are undetermined in the final state. On the other hand, there are 5 more constraints that can be added by requiring that (i) the two components of the observed vector $\not\!\!E_T$ equal the sum of the respective components of the two neutrinos, (ii) the invariant mass of each lepton and neutrino pair equals the W boson mass, and (iii) that the mass of the top and antitop quarks are equal [87]. These lead to a total of 17 constraints to a system of 18 variables, which is one constraint less than required to fully reconstruct the event. The system of equations can be written as follows

$$M^2_{W^+} = (E_{\ell_1} + E_{\nu_1})^2 - (\vec{p}_{\ell_1} + \vec{p}_{\nu_1})^2 \tag{6.1}$$

$$M^2_{W^-} = (E_{\ell_2} + E_{\nu_2})^2 - (\vec{p}_{\ell_2} + \vec{p}_{\nu_2})^2 \tag{6.2}$$

$$(E_{\ell_1}+E_{\nu_1}+E_{b_1})^2-(\vec{p}_{\ell_1}+\vec{p}_{\nu_1}+\vec{p}_{b_1})^2=(E_{\ell_2}+E_{\nu_2}+E_{b_2})^2-(\vec{p}_{\ell_2}+\vec{p}_{\nu_2}+\vec{p}_{b_2})^2 \quad (6.3)$$

where M_W is the invariant mass of the W boson; $(E_\ell, \vec{p_\ell})$, and $(E_\nu, \vec{p_\nu})$ are the components of the Lorentz four-vector of a lepton and neutrino from the W boson decay.

To solve the underconstrained system of equations, instead of directly involving the observed $\not{E}_T$ into the calculation, we scan all possible η for each unobserved neutrino (neutrino-weighting, or νWT) [84] [85] [86]. With input η values for the two neutrinos and input m_t, the four-momentum of each neutrino can be fully solved. Since m_t is what we are looking for, we scan a wide range of m_t for all combinations of the two given neutrino η's. This procedure is called "kinematic reconstruction".

The equations (6.1) - (6.3) can be reduced to a system of two quadratic equations with each equation corresponding to one of the two neutrinos. A chosen pair of η will be noted as failing the kinematic reconstruction if no real solutions are found for any given m_t. If all chosen η and m_t values fail, then the event will be noted as failing the kinematic reconstruction. A detailed derivation of quadratic solutions is documented in Appendix A.

The agreement of the calculated p_T of the two neutrinos and the observed $\not{E}_T$ is quantified by a weight assigned to each pair of neutrino solutions:

$$\omega(\eta_1,\eta_2)=\frac{1}{N_{\text{iter}}}\sum_{i=1}^{N_{\text{iter}}}\exp\left(\frac{-(\not{E}_{x,i}^{\text{calc}}(\eta_1,\eta_2)-\not{E}_x^{\text{obs}})^2}{2\sigma^2_{\not{E}_x}}\right)\exp\left(\frac{-(\not{E}_{y,i}^{\text{calc}}(\eta_1,\eta_2)-\not{E}_y^{\text{obs}})^2}{2\sigma^2_{\not{E}_y}}\right), \quad (6.4)$$

where N_{iter} runs over all neutrino solutions for all assignments of jets with leptons in the $t\bar{t}$ final state for each given η pair. There are 2 assignments of jets for each event and each assignment gives up to 2 solutions per ν, so N_{iter} is up to 8 in total. The resolutions $\sigma_{\not{E}_x}$ and $\sigma_{\not{E}_y}$ are detector-based parameters of the method that account for the difference between the calculated $\not{E}_T$ and observed $\not{E}_T$. This parameter can affect the sensitivity to the m_t, and more details are discussed in the next Section. For each given m_t, if we integrate the contribution from all pairs of neutrino ηs, an overall weight $W(m_{\mathrm{t}})$ will be derived as follows:

$$W(m_{\mathrm{t}}) = \int \omega(\eta_1, \eta_2)\rho(\eta_1)\rho(\eta_2)d\eta_1 d\eta_2 \tag{6.5}$$

where $\omega(\eta_1, \eta_2)$ is the weight for the given neutrino η pair, and the $\rho(\eta)$ probability distribution is taken as Gaussian, with a root mean square (RMS) that depends on m_t. As discussed in Ref. [88], the width dependence on the top quark mass can be parameterized as a linear function:

$$\sigma_\eta = -0.001 \times m_t + 1.17 \tag{6.6}$$

In fact, the sensitivity of fitted m_t to the specific parameterization of the Gaussian is very small.

A weight distribution is defined once the weights are computed as a function of the scanned m_t for each event. In this analysis, weights are calculated for each given neutrino η pair with 1 GeV increments in a newly optimized mass range of 115 to 220 GeV. This mass range is narrower than in our previous choice of 80 to 330 GeV to improve the statistical uncertainty (see Sec. 7.3). Fig. 6.2 shows an example of a single event weight distribution. Typically the weight distribution features a peak near the input top quark mass ($m_{\mathrm{t}}^{\mathrm{MC}}$) contributed by the high weights from good agreements of calculated and observed $\not{E}_T$. There are also contributions from incorrect neutrino solutions generated by quadratic equations, as well as wrong jet assignments of leptons and neutrinos. In fact, most of the properties of the top quark (eg., the object p_T) are mass dependent (see Fig. 1.5), and offer some sensitivity to m_t even if combined improperly in incorrect jet assignments and neutrino solutions. As shown in Fig. 6.3, the weight distribution averaged over all events for samples with $m_{\mathrm{t}}^{\mathrm{MC}}$ of 160 GeV, 170 GeV and 180 GeV are well separated. Since we employ a template method, the νWT approach is less reliant than a Matrix-Element method [79] on specific details of modeling, particularly of jets in the final states. For example, the Matrix-Element method needs to incorporate a transfer function that calculates the probability of a truth level parton energy to be reconstructed as a certain measured energy.

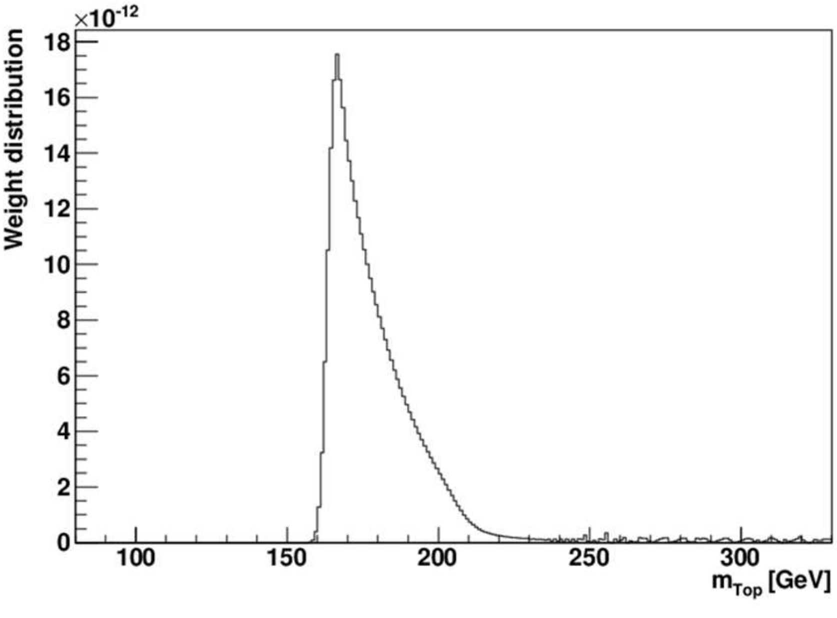

Figure 6.2. Example weight distribution for a single event in $t\bar{t}$ MC sample with $m_t = 172.5$ GeV.

6.2. Unclustered $\not{E}_T$ Resolution

The unclustered $\not{E}_T$ ($\not{E}^{\text{unc}}$) is defined as the event $\not{E}_T$ after all the reconstructed p_T (of charged leptons and jets) is removed. It may come from out-of-cone showering at detector level, soft gluon radiation, pileup, etc. The $\not{E}^{\text{unc}}$ resolution ($\sigma^{\text{unc}}_{\not{E}_{x,y}}$) is considered since both the $\not{E}^{\text{calc}}_{x,y}$ and the $\not{E}^{\text{obs}}_{x,y}$ components in Eq. 6.4 contain the

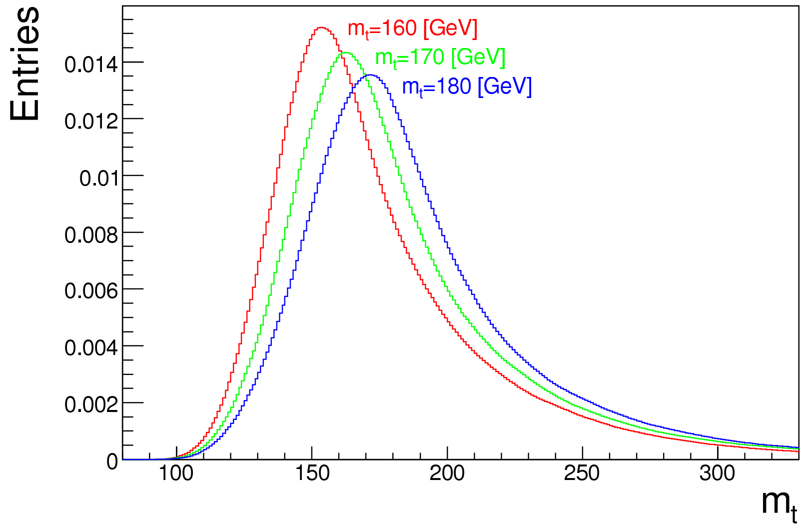

Figure 6.3. The weight distribution averaged over all events in MC $t\bar{t}$ sample of masses 160 GeV (*red*), 170 GeV (*green*) and 180 GeV (*blue*).

very same jets and leptons, so only the fluctuations in the unclustered energy can cause differences. The magnitude of the resolutions in Eq. 6.4 is based on that of $\not{E}^{\mathrm{unc}}$ measured in the $Z \rightarrow ee$ channel, which can be parameterized as a linear dependence on the square root of the unclustered scalar transverse energy ($S_{\not{E}_T}$), or as a value determined from all the events in the dilepton channel. The $S_{\not{E}_T}$ is defined as the scalar sum of the transverse energies of all unclustered calorimeter cells. This linear parameterization was first used in Run II-A (see Ref. [89]). I rederived this parameterization for Run II-B1 + Run II-B2 MC samples (4.3 fb^{-1}), as well as for the full Run II-B MC samples as a whole (8.7 fb^{-1}). I firstly use a Gaussian to fit $\not{E}_{x,y}$ in each $S_{\not{E}_T}$ bin. Then I take the RMS of the fit as $\sigma^{unc}_{\not{E}_{x,y}}$ and finally fit it to a linear function that is dependent on the square root of $S_{\not{E}_T}$ (see Fig. 6.4). The parameterization in Run II-B is given by:

$$\sigma^{unc}_{\not{E}_{x,y}} = 6.24 + 0.60 \times \sqrt{S_{\not{E}_T}}. \tag{6.7}$$

The full Run II-B MC is checked to be consistent with both Run II-B1 & Run II-B2 MC in $\sigma_{\not{E}_{x,y}}$, and they are all systematically larger than Run II-A MC by about 5 GeV. This is because the increased instantaneous luminosity causes more pileup and worsens the $\not{E}_{\mathrm{T}}$ resolution. The agreement between data and MC linear parameterization has been validated in Ref. [89] for Run II-A data.

In addition to the ${\not{E}_{x,y}}^{unc}$ resolution, there are effects from unclustered extra jets, or disrete values of top quark mass and neutrino η that vary the $\not{E}^{\mathrm{calc}}_{x,y}$ from $\not{E}^{\mathrm{obs}}_{x,y}$ by a few GeV. Therefore, we will use a flat parameterization that can automatically take into account all above effects. The new parameterization is determined to be 25 GeV, which is described in Sec. 7.3.

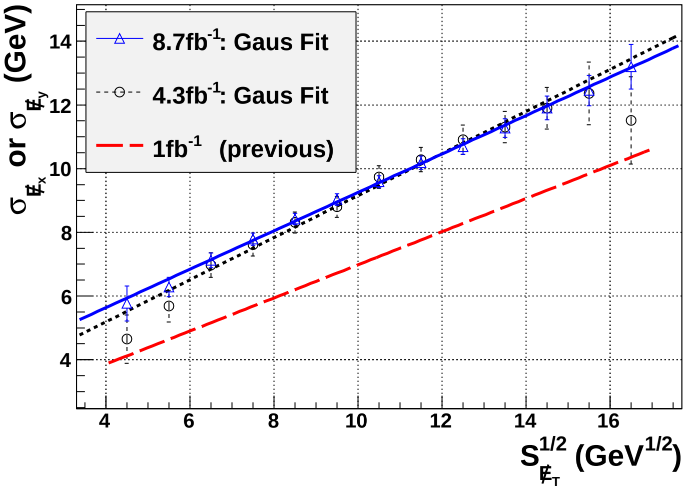

Figure 6.4. Dependence of the resolution in ${\not{E}_x}^{unc}$ and ${\not{E}_y}^{unc}$ for exclusive $Z \rightarrow ee$ events with two jets, as a function of $\sqrt{S_{\not{E}_T}}$. The previous 1 fb^{-1} parameterization is from Ref. [89].

6.3. Kinematic Reconstruction Efficiencies

The event yields, after all event selections, are shown in Tables 6.1 and 6.2 for all channels before and after kinematic reconstruction. The efficiencies in kinematic reconstruction of the individual channels are given in Table 6.3. It shows that the efficiencies of kinematic reconstruction are not only consistent between data and the expectation, but also universal across all the channels in the dilepton final states for all $t\bar{t}$ events. The efficiencies for backgrounds are slightly lower than that of signals. Table 6.4 shows the efficiencies for each run period in the $e\mu$ channel, which indicates that the kinematic reconstruction efficiency is independent of the run periods as well. The variation of the efficiencies in data and for backgrounds is due to the statistical limit, especially for the instrumental backgrounds where we have only 15 events in the $e\mu$ channel.

Table 6.1: Expected and observed dilepton event yields from background and signal (for $\sigma_{t\bar{t}} = 7.24$ pb) processes in 9.7 fb^{-1} of integrated luminosity. The event yields are AFTER all selections and BEFORE the kinematic reconstruction of $t\bar{t}$ pairs.

Channel	$t\bar{t} \to ll$	$Z \to ll$	diboson	instrumental	total	data
$e\mu$	267.1	11.7	3.2	19.7	301.7	340
ee	91.9	11.0	1.5	3.1	107.5	115
$\mu\mu$	86.0	17.2	2.2	0	105.4	110

Table 6.2: Expected and observed dilepton event yields from background and signal (for $\sigma_{t\bar{t}} = 7.24$ pb) processes in 9.7 fb^{-1} of integrated luminosity. The event yields are AFTER all selections and AFTER the kinematic reconstruction of $t\bar{t}$ pairs.

Channel	$t\bar{t} \to ll$	$Z \to ll$	diboson	instrumental	total	data
$e\mu$	265.2 ± 23.4	11.4 ± 1.5	3.0 ± 1.2	18.5 ± 6.2	298.1 ± 24.6	336
ee	91.6 ± 9.9	10.4 ± 1.7	1.4 ± 0.3	3.1 ± 1.8	106.5 ± 11.0	113
$\mu\mu$	85.8 ± 7.4	15.6 ± 2.0	2.1 ± 0.5	0	103.5 ± 8.3	109

Table 6.3: Efficiencies for kinematic $t\bar{t}$ reconstruction after implementing all selections and optimizing the resolutions $\sigma_{\not{E}_x}$ and $\sigma_{\not{E}_y}$ in the ee, $e\mu$ and $\mu\mu$ channels.

Sample	$t\bar{t}$ (172.5 GeV)	Z$\to \ell\ell$	diboson	instrumental	expected	data
$e\mu$	99.3%	97.7%	94.3%	93.8%	98.9%	98.9%
ee	99.7%	94.2%	94.2%	100.0%	99.0%	98.1%
$\mu\mu$	99.8%	90.8%	95.0%	-	98.3%	99.0%

6.4. Probability Density Templates

The weight distribution generated from the weighted neutrino solutions for each event contains the information of the top quark mass. To utilize the weight distribution, we can take just one parameter to serve as an estimation of the top quark mass. For example, we can use the peak of the weight distribution, or more complicated quantities derived from the weight distribution. Parameters that are more mass dependent and less correlated with each other are more effective for the discrimination of different masses. In this analysis, the first two moments, namely the mean (μ_w) and RMS (σ_w) of the weight distributions are chosen to construct templates. These have been found to preserve nearly all of the useful information in the weight

Table 6.4: Efficiencies for kinematic $t\bar{t}$ reconstruction, after implementing all cuts in the $e\mu$ channel, presented as a funtion of separate run periods. The instrumental backgrounds have an efficiency of 100% in Run II-B3 and 85.7% in Run II-B4, and data are 100% efficient in Run II-B3 and 98.8% in Run II-B4. Efficiencies for diboson and instrumental backgrounds are subject to their statistical limits.

Run period	$t\bar{t}$ (172.5 GeV)	$Z\rightarrow \tau\tau$	diboson	instrumental	expected	data
RunII-A	99.3%	96.7%	97.1%	100%	99.1%	95.4%
RunII-B1	99.4%	98.7%	89.8%	100%	99.2%	98.3%
RunII-B2	99.4%	97.3%	95.0%	100%	99.2%	100%
RunII-B3&4	99.3%	98.0%	94.6%	88.9%	98.6%	99.3%

distribution [89]. The distributions in these two parameters are given in Figs. 6.5 and 6.6 where data is shown to agree well with the signal and background hypothesis. The background enriched distributions of μ_w with events before topological cuts and kinematic reconstruction are shown in Fig. 6.7, where the MC simulation is also in good agreement with data. Fig. 6.8 are the distributions of μ_w with different $m_{\mathrm{t}}^{\mathrm{MC}}$. It shows that for $m_{\mathrm{t}}^{\mathrm{MC}} >$ or $<$ 172.5 GeV, the distributions are well separated from the 172.5 GeV distribution and are all systematically shifted to the right or left of 172.5 GeV correspondingly. The good discrimination of different $t\bar{t}$ MC samples with various $m_{\mathrm{t}}^{\mathrm{MC}}$ is important in the template method since it will help reduce the statistical uncertainties of fitted m_{t} and improve the precision of the measurement.

For signal, a 3-D probability density distribution can be constructed from μ_w, σ_w, and $m_{\mathrm{t}}^{\mathrm{MC}}$, denoted as $h_s(\mu_w, \sigma_w \mid m_{\mathrm{t}}^{\mathrm{MC}})$. We construct 15 signal templates for $m_{\mathrm{t}}^{\mathrm{MC}}$ from 130 GeV to 200 GeV with a 5 GeV increment. Due to different statistics of the various $t\bar{t}$ MC samples, all 2-D sub-distributions of μ_w and σ_w are normalized to the same number of events for different $m_{\mathrm{t}}^{\mathrm{MC}}$. The errors are adjusted to reflect the full statistics via the fractional uncertainty. Illustrations of signal templates at

$m_{\mathrm{t}}^{\mathrm{MC}}$=175 GeV, $h_s(\mu_w, \sigma_w \mid 175\mathrm{GeV})$ for all channels are shown in Fig. 6.9. The binning is determined separately for each individual dilepton channel as shown in Fig. 6.9. The bin sizes are chosen to minimize the expected statistical uncertainty in studies of pseudoexperiments [88] (see Sec. 7.3).

The background probability density histograms, $h_b(\mu_w, \sigma_w)$, are obtained as the 2-D distribution of μ_w and σ_w of simulated background events. Contributions from all backgrounds are weighted with respect to their expected yields and summing over into one background template. The background template is also normalized to the same scale of all signal templates. Illustrations of background templates for all channels are shown in Fig. 6.10. The binning of the background templates is the same as the signal templates.

6.5. Maximum Likelihood and Top Quark Mass Extraction

The top quark mass is extracted using a maximum likelihood method. We define the likelihood of the true m_t to be equal to $m_{\mathrm{t}}^{\mathrm{MC}}$ as:

$$\begin{aligned}&\mathcal{L}(\mu_{\mathrm{i}}\mathrm{tw}_{\{1..\mathrm{N}\}}, \sigma_{w\{1..\mathrm{N}\}}, \mathrm{N} \mid \bar{\mathrm{n}}_{\mathrm{b}}, \bar{\mathrm{n}}_{\mathrm{s}} \mid m_{\mathrm{t}}^{\mathrm{MC}}) = \\ &\quad \prod_{i=1}^{N} \frac{\bar{n}_s h_s(\mu_{\mathrm{i}}\mathrm{tw}_i, \sigma_{w\mathrm{i}} \mid m_{\mathrm{t}}^{\mathrm{MC}}) + \bar{n}_b h_b(\mu_{w\mathrm{i}}, \sigma_{w\mathrm{i}})}{\bar{n}_s + \bar{n}_b},\end{aligned} \tag{6.8}$$

where i is the event number in the data sample, N is the total number of observed events, and $\bar{n}_s$ and $\bar{n}_b$ are the expected number of signal and background events in our data sample, respectively (see Table 6.2). From left to right, the three groups of parameters of the likelihood are separated by vertical bars: measured, expected and input values. The range of the $m_{\mathrm{t}}^{\mathrm{MC}}$ is from 130 GeV to 200 GeV with a 5 GeV increment.

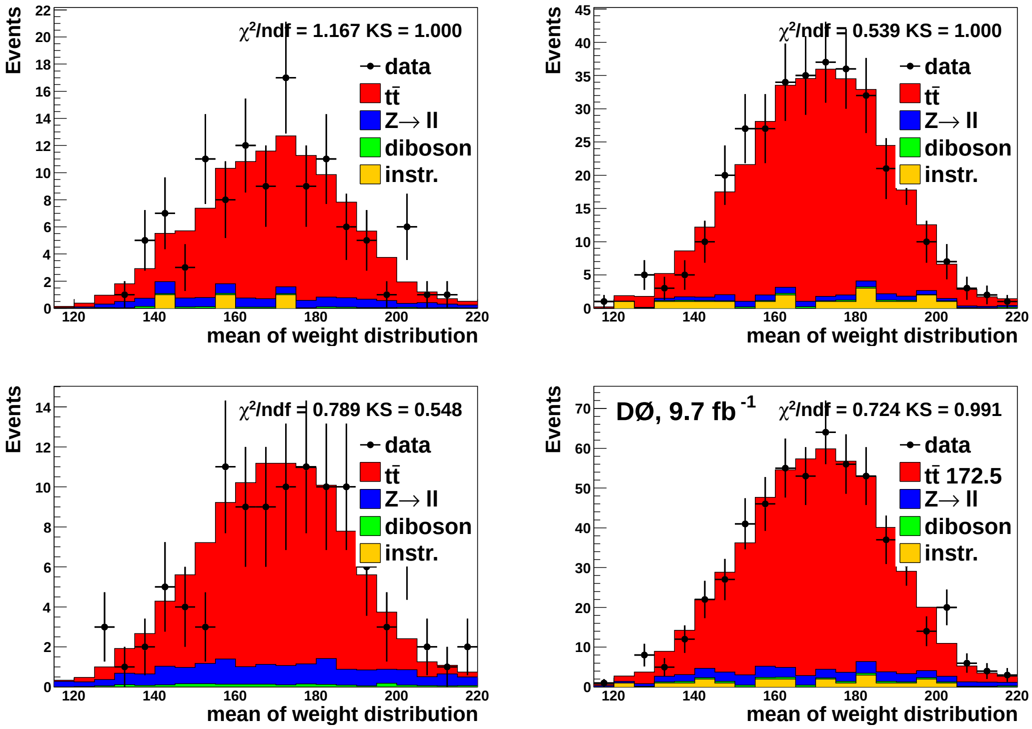

Figure 6.5. Distribution of μ_w for all events after full selections and kinematic reconstruction in the ee (top left), $e\mu$ (top right), $\mu\mu$ (bottom left) and combined (bottom right) channels.

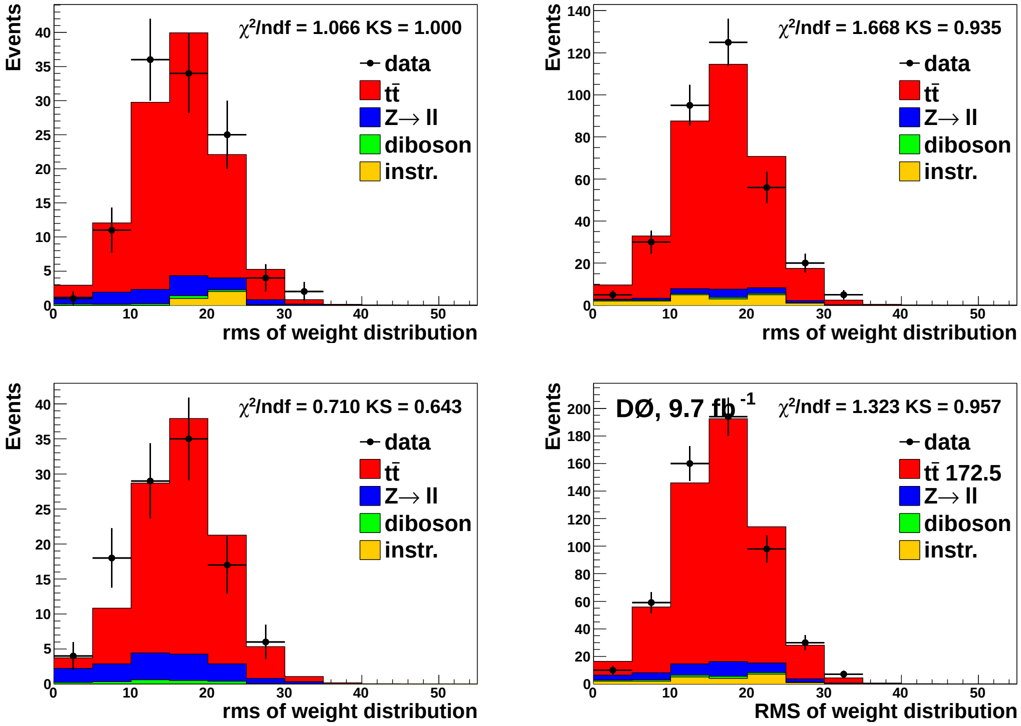

Figure 6.6. Distribution of σ_w for all events after full selections and kinematic reconstruction in the ee (top left), $e\mu$ (top right), $\mu\mu$ (bottom left) and combined (bottom right) channels.

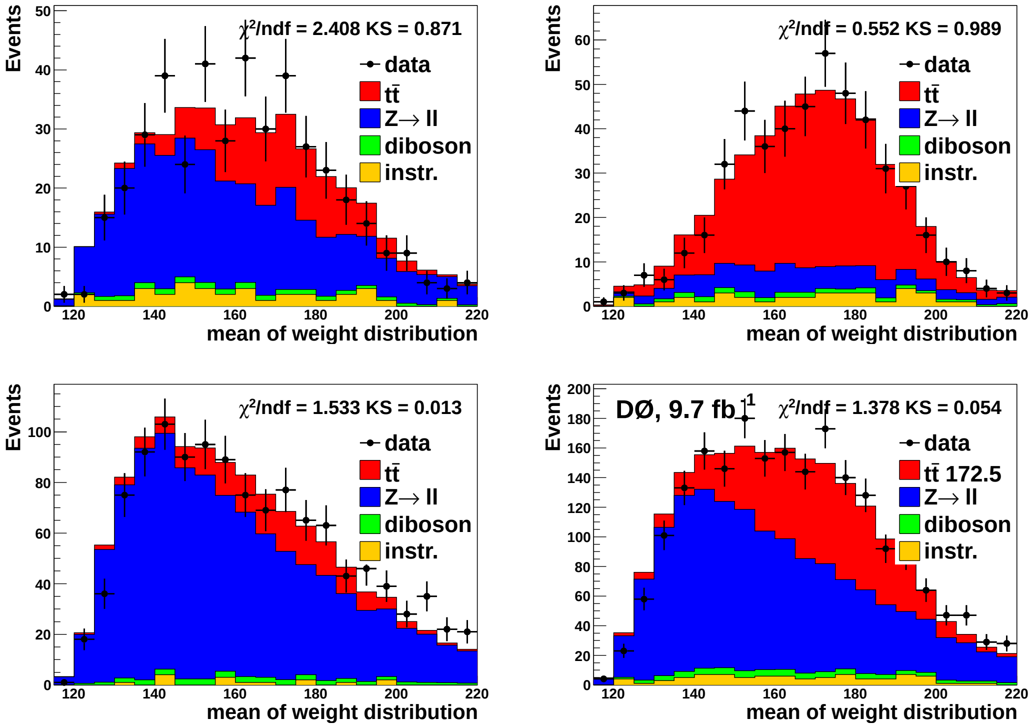

Figure 6.7. Distribution of μ_w for all events before topological cuts but after kinematic reconstruction in the ee (top left), $e\mu$ (top right), $\mu\mu$ (bottom left) and combined (bottom right) channels.

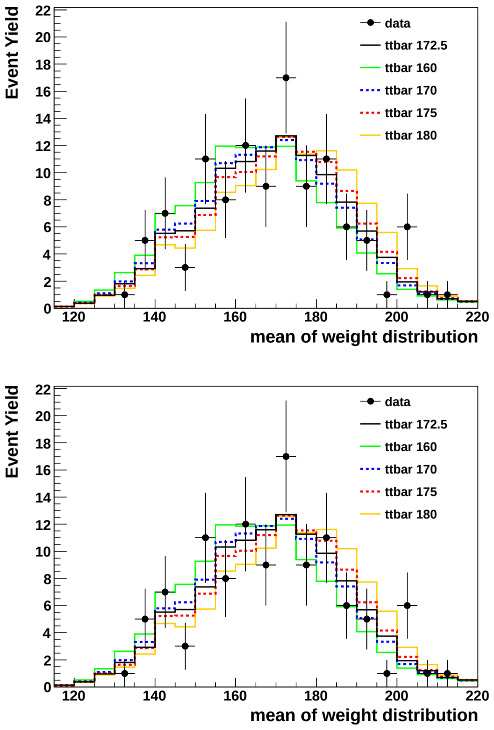

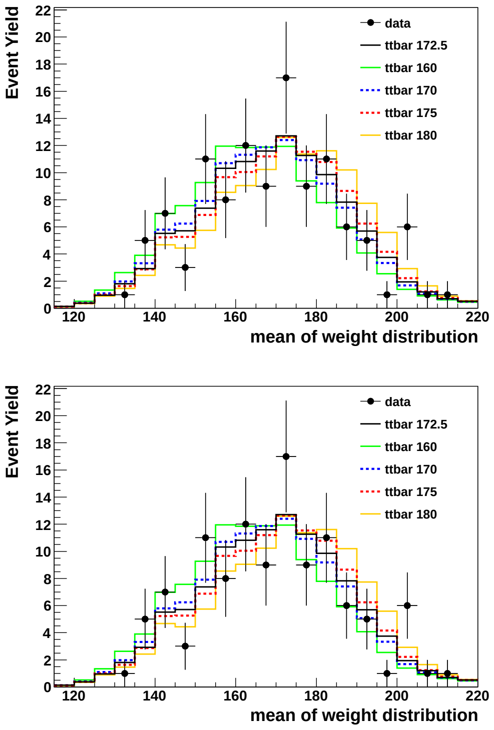

Figure 6.8. Comparison of distribution of μ_w with different $m_{\rm t}^{\rm MC}$ for all events after full selections and kinematic reconstruction in the ee (top left), $e\mu$ (top right), $\mu\mu$ (bottom left) and combined (bottom right) channels.

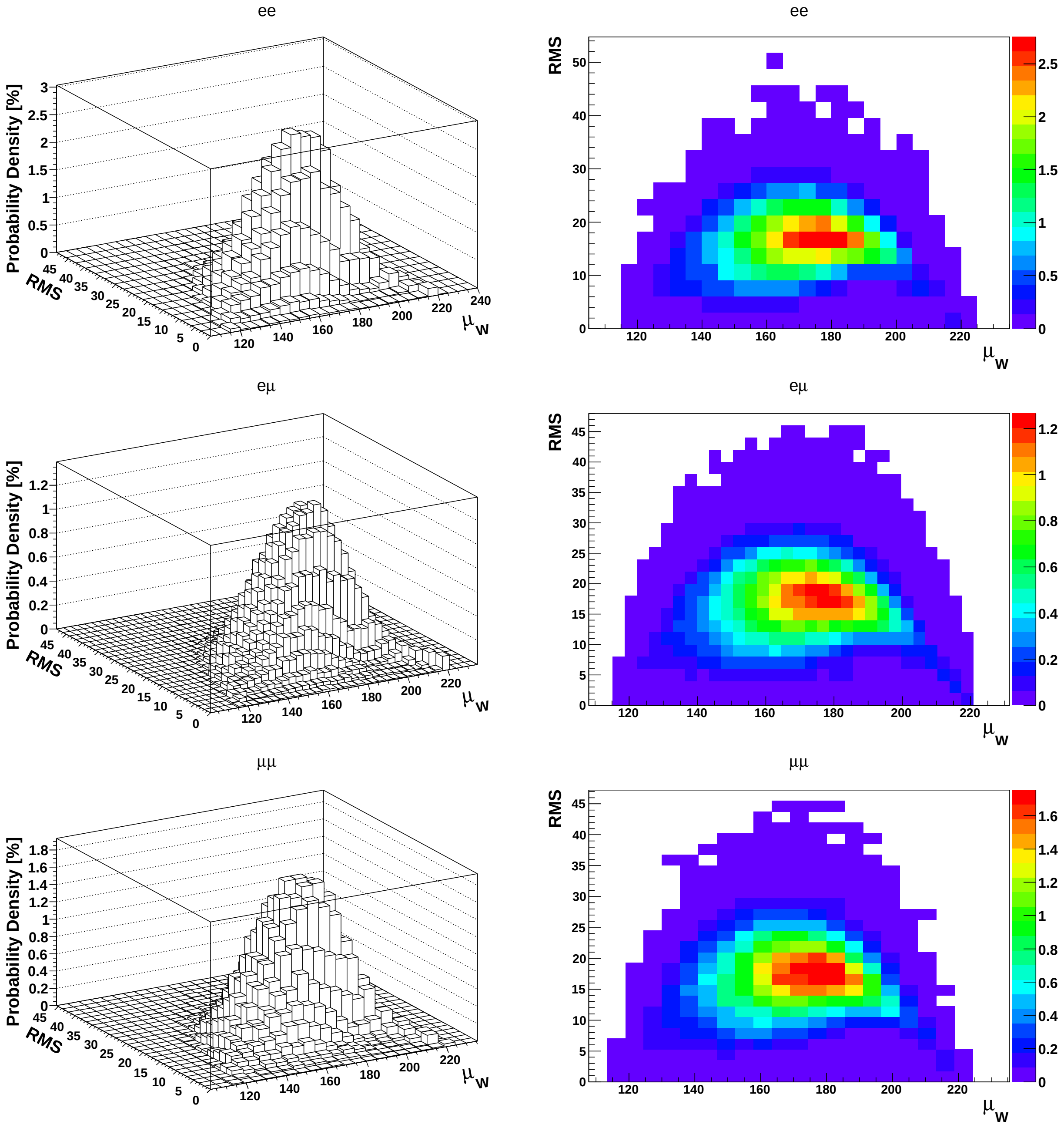

Figure 6.9. The optimized signal probability density histogram for Run II-B $t\bar{t}$ MC sample with m_t^{MC}=175 GeV for (top) ee, (middle) $e\mu$, and (bottom) $\mu\mu$ channels in (left) 3-D and (right) color representation.

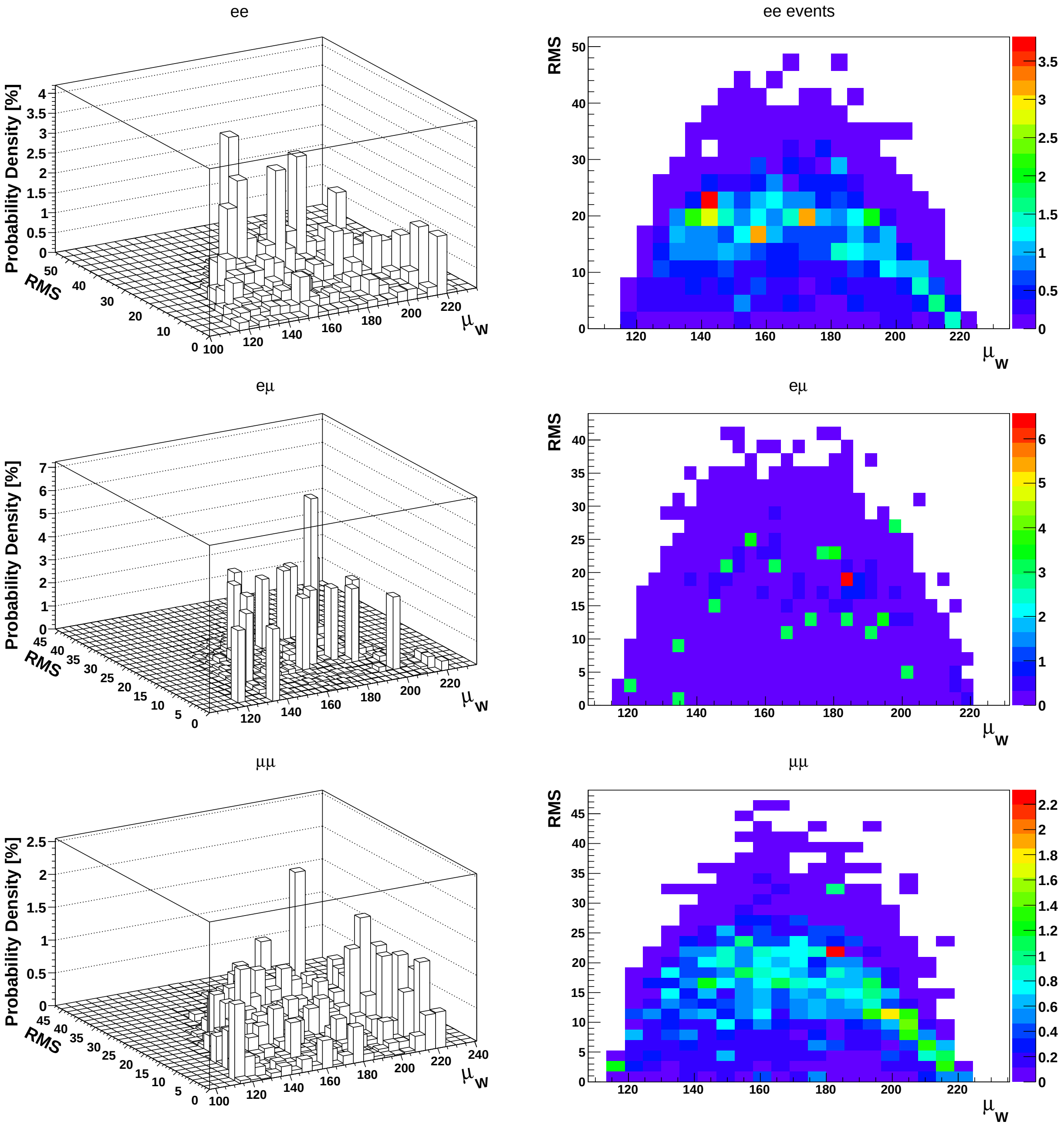

Figure 6.10. The optimized background probability density histogram for Run II-B (top) ee, (middle) $e\mu$, and (bottom) $\mu\mu$ channels in (left) 3-D and (right) color representation.

For each event in data, $h_s(\mu_w, \sigma_w \mid m_{\mathrm{t}}^{\mathrm{MC}})$ and $h_b(\mu_w, \sigma_w)$ are obtained from corresponding bins in the signal and background templates. The overall likelihood for each $m_{\mathrm{t}}^{\mathrm{MC}}$ is calculated by multiplying contributions from each event in data. The distribution of $-\log\mathcal{L}$ vs. $m_{\mathrm{t}}^{\mathrm{MC}}$ is fit by a parabola with a fit interval of 15 GeV for all the channels around the lowest value of $-\log\mathcal{L}$. This range is optimized by testing the performance of the expected statistical uncertainty (see Sec. 7.3). In principle, the likelihood distribution is not essentially parabolic, so the fit range is restricted to minimize biases while still retaining a precise fitted result. This fitting procedure is iterated up to five times until the difference between the new and previous fitted m_t value ($m_{\mathrm{t}}^{\mathrm{fit}}$) is below 0.1 GeV. If the 0.1 GeV difference is not reached in five iterations, the last fitted value is taken as the estimated m_t. It starts with the minimum of the likelihood points and centers the fit range around this point. In subsequent iterations, the center of the fit range is replaced by the minimum from the fit in the previous iteration until the above requirements are satisfied. The iterative fitting provides greater stability of fitted m_t than with just one fit. Although most distributions can be fit with the parabola around its minimum, a fit in the full range requires more complicated functions. The likelihood $-\log\mathcal{L}$ is no longer a parabola at full range and previous studies showed that fitting the full range with third degree polynomials did not improve our precision.

The value of $m_{\mathrm{t}}^{\mathrm{fit}}$ at the minimum of the parabola defines our top quark mass estimate. Near the minimum, the Gaussian approximation allows you to consider half of the width of the parabola where $-\log\mathcal{L}$ rises 0.5 units above its minimum value to be the estimated statistical uncertainty, σ_{m_t}.

The combination of all three channels is done by multiplying the likelihoods of all these channels:

$$\mathcal{L}^{combined}(m_t) = \mathcal{L}^{ee}(m_t) \times \mathcal{L}^{e\mu}(m_t) \times \mathcal{L}^{\mu\mu}(m_t) \tag{6.9}$$

Therefore the combined negative log-likelihood is

$$-\ln(\mathcal{L}^{combined}(m_t)) = \sum_{ch}(-\ln(\mathcal{L}^{ch}(m_t))) \tag{6.10}$$

where “ch” denotes each of the three channels.

6.6. Calibration

There are several factors that can cause biases in the estimated top quark mass, for instance, the presence of backgrounds, or the fact that the likelihood is non-parabolic. Therefore a calibration of the fitted top mass and its uncertainty is needed.

6.6.1. Pseudoexperiments

The performance of the mass extraction is evaluated using an ensemble testing techniques, where the value of m_t is extracted using pseudoexperiments (PEs). The pseudoexperiments mimic the data measurement by utilizing simulated events that are randomly selected with the number of events match the data. An array of pseudoexperiments is called an *ensemble*. The number of signal and background events in a given pseudoexperiment is selected according to a Poisson distribution, with the mean taken from a random number generated with a Gaussian distribution that centered at the expected event yield, and with uncertainty equal to the total statistical and systematic uncertainty.

The number of PEs are chosen to be 3000 for the purpose of reducing the statistical uncertainty of the sysetmatic uncertainties as described in Sec. 7.3. Due to the fact that the MC samples are statistically limited while the number of PEs is large, events can be selected more than once into a given ensemble. Therefore, a correction for correlations among PEs must be performed. The oversampling of a MC sample can falsely reduce the uncertainties of the PEs. The uncertainties on the average $m_{\mathrm{t}}^{\mathrm{fit}}$ in the 3000 PEs is corrected by multiplying an oversampling parameter given by $\sqrt{N_{\mathrm{sig}} * N_{\mathrm{pe}}/N_{\mathrm{MC}}}$, where N_{sig} is the number of average $t\bar{t}$ events in each pseudoexperiment, N_{pe} is the total number of pseudoexperiments (3000 in our optimal case), and N_{MC} is the number of events passing the selection in the $t\bar{t}$ MC sample. This gives the average number of times each event in the pools of events is elected for ensemble testing. The uncertainties on pulls which is discussed in the last section are also corrected according to $\sqrt{\frac{1}{2}(\frac{1}{N_{\mathrm{template}}^{\mathrm{events}}} + \frac{1}{N_{\mathrm{pe}}})}$, where $N_{\mathrm{template}}^{\mathrm{events}}$ is the total number of $t\bar{t}$ events with respect to the corresponding $m_{\mathrm{t}}^{\mathrm{MC}}$.

6.6.2. Mass measurement calibration

A good method must work for a large range of possible top quark masses. To perform the calibration, PEs are performed for a total of 7 mass points including m_t^{MC} = 160, 165, 170, 175, 180, 185, and 190 GeV. The mean value of fitted m_t at each point is parameterized as the following:

$$m_t^{fit} = \alpha(m_t^{MC} - 170) + \beta + 170 \tag{6.11}$$

where m_t^{fit} is the fitted m_t. Plots are shown in Fig. 6.11. The same MC events are used for templates and PEs. This ensures that any bias detected within ensemble testing is systematic from the method. The high χ^2/ndf in the plots is mainly due to the finite statistics of signal templates. Details about the corresponding correction are discussed in Sec. 7.3.

To calibrate the measured top quark mass, Eq. 6.11 is inverted:

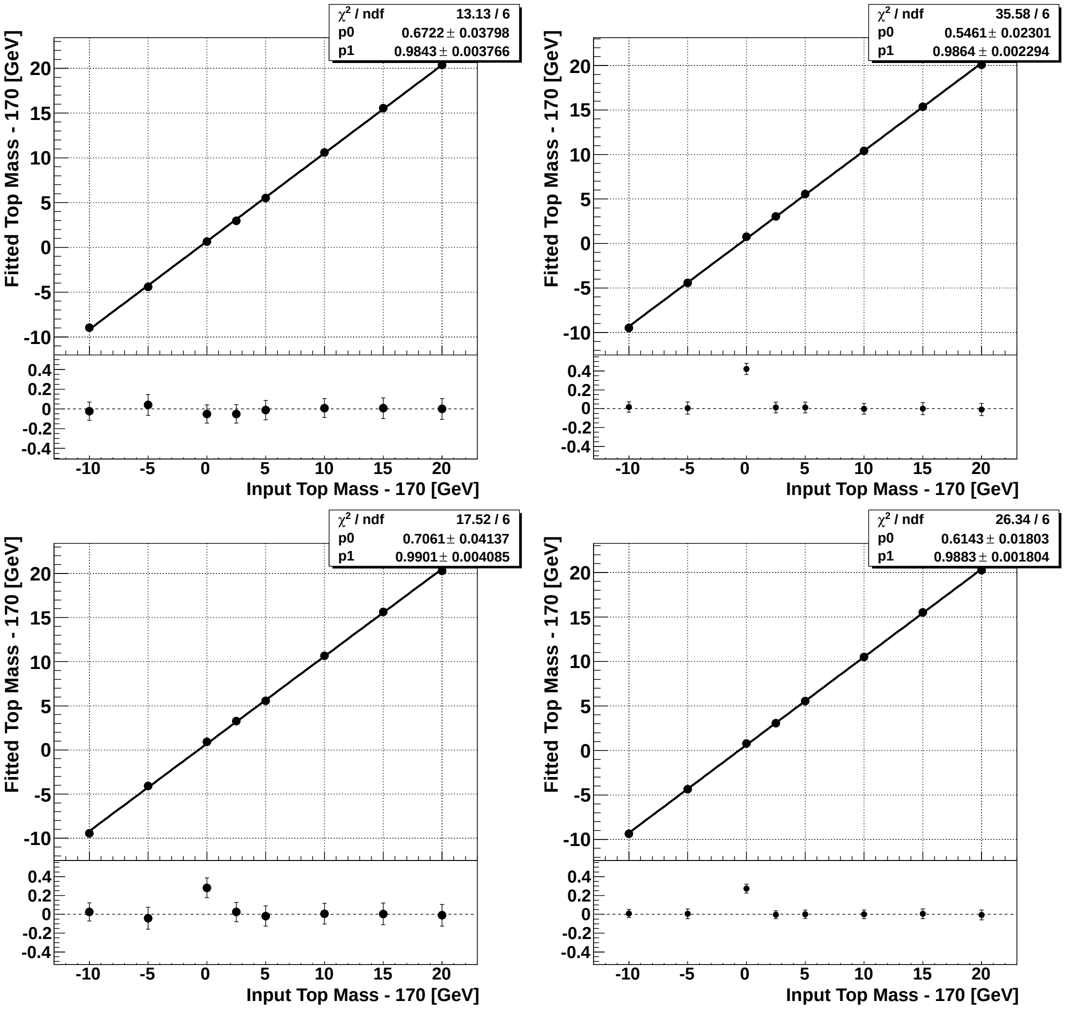

Figure 6.11. Calibrations of m_t: Fitted m_t as a function of $m_{\mathrm{t}}^{\mathrm{MC}}$ for the *ee* (top left), $e\mu$ (top right), $\mu\mu$ (bottom left) and combined (bottom right) channels.

$$m_t^{calib} = \frac{m_t^{fit} - \beta - 170}{\alpha} + 170 \tag{6.12}$$

where m_t^{calib} is the measured top quark mass with the possible biases of the method corrected for.

To correct the estimated statistical uncertainty of the m_t^{meas}, the calibration can be formulated through error propagation:

$$\sigma^{calib} = \frac{\sigma^{meas}}{\alpha} \tag{6.13}$$

To ensure that the statistical uncertainty is correctly estimated, a further test is done using the *pull*, defined as:

$$p = \frac{m_t^{calib} - m_t^{MC}}{\sigma^{calib}} \tag{6.14}$$

The pull is calculated for each individual PE and the pull distribution of the ensemble is used to test the uncertainty. Usually, the pull distribution is Gaussian and the width can be used as a quantified tool of the tests. For a good estimation of the statistical uncertainty, the pull width should be close to 1. If the uncertainty is overestimated, the pull width will be smaller than 1, and it will be larger than 1 for underestimation. Fig. 6.12 shows the distribution of pull widths for all the three channels and the combination. The pull width is correlated with the χ^2/ndf of the calibration curve, but as discussed in the previous section, since the pull is corrected for oversampling, it becomes less sensitive to statistical fluctuations than the χ^2/ndf.

The pull vs. $m_{\mathrm{t}}^{\mathrm{MC}}$ is fitted to a constant:

$$p(m_t) = \lambda \tag{6.15}$$

To calibrate for the overestimation or underestimation of the statistical uncertainty, the correction is applied as:

$$\sigma^{corr} = \frac{\lambda}{\alpha}\sigma^{meas} \tag{6.16}$$

where $\sigma^{calib,\,corr}$ is the calibrated, pull-corrected statistical uncertainty.

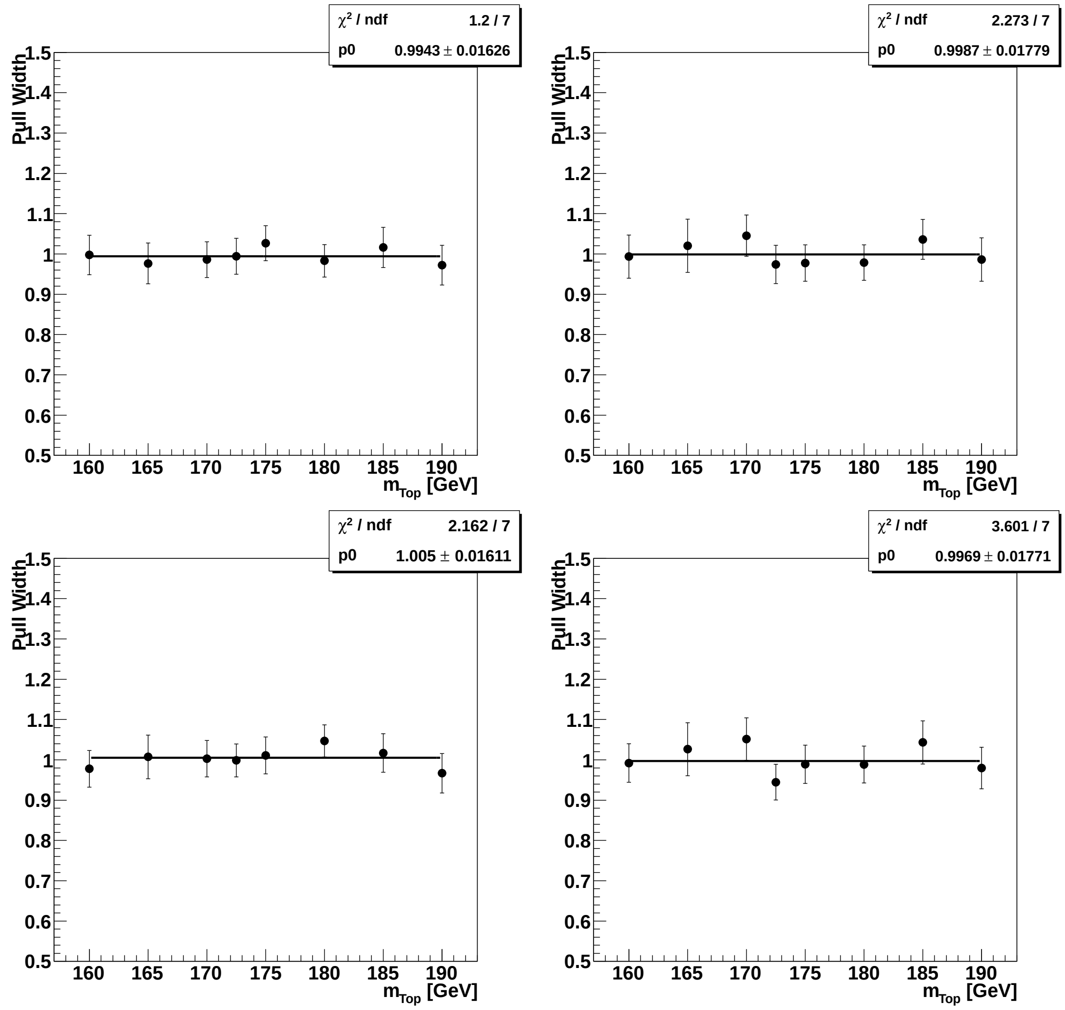

Figure 6.12. Calibrations of m_t: Pull width as a function of m_t^{MC} for the ee (top left), $e\mu$ (top right), $\mu\mu$ (bottom left) and combined (bottom right) channels.

Chapter 7

OPTIMIZATION OF THE METHOD

The performance of the mass extraction method is directly affected by the mass resolution in the weight distribution, which can be optimized through choice of jet assignments, $\sigma_{\not{E}}^{\mathrm{unc}}$, scanned mass range, etc. On the other hand, the increased number of data and MC events require adjustment to statistis-sensitive parameters such as the binning of the templates and the number of pseudoexperiments. As a result, I have developed a strategy of fully optimizing the analysis comparing to the setups used in previous 4.3 fb^{-1} analysis (*nominal analysis*). Since statistical uncertainty were projected to dominate, I focused in optimizing the expected statistical uncertainty. However, I also worked to ensure systematic uncertainties. This chapter talks about the optimizations of the method and their expected performance.

7.1. Study of the Performance of Assigning Jets and ν Solutions

In the dilepton final states, the breakdown of particles in the decay chain is shown in Fig. 7.1. Since we do not know the electric charge of the jet corresponding to the b or $\bar{b}$ quarks, there are two possible jet-to-lepton assignments. In each assignment, the system of quadratic equations results in up to two neutrino p_T solutions for each of the two neutrinos. Therefore, with the correct jet assignment and neutrino rapidities, there is one pair of "correct" solutions (Configuration 1) out of four configurations of neutrino solutions. Fig. 7.2 shows the weight distribution of a single MC event ($m_{\mathrm{t}}^{\mathrm{MC}}$=170 GeV) for the four configurations of neutrino solutions with correct neutrino rapidities. The correct configuration (Configuration 1) peaks just around 170

GeV, and has the maximum integrated weight of the four configurations. Therefore, as shown in the top plot of Fig. 7.3, the overall weight distribution is dominated by the correct configuration with the mean value of the distribution shifted slightly from 170 GeV by Configuration 3.

In all given masses and neutrino η pairs tried, only a few trials give reconstructed neutrino momenta that are close to the true values. Each trial is weighted with Eq. 6.4. The distribution in signal weight typically features a peak around the input m_t, m_t^{MC}, with incorrect ν solutions spreading out (see bottom plot of Fig. 7.3), while the background weight distribution is more dispersed (see Fig. 7.4). Table 7.1 shows the truth level neutrino momenta and solved neutrino momenta with correct jet assignment and correct neutrino η assumptions. As can be seen, ν_1 solution 1 corresponds to $\bar{\nu}$ and ν_2 solution 1 corresponds to ν by matching all their momenta components.

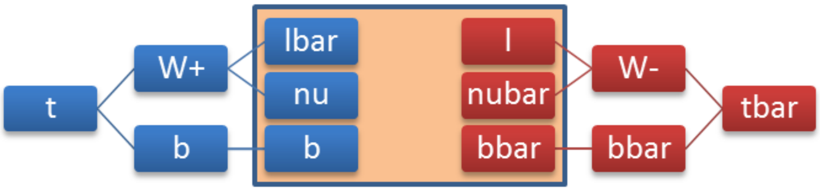

Figure 7.1. Diagram of the decay process of $t\bar{t}$ events. The particles in the boxed orange area are final state particles.

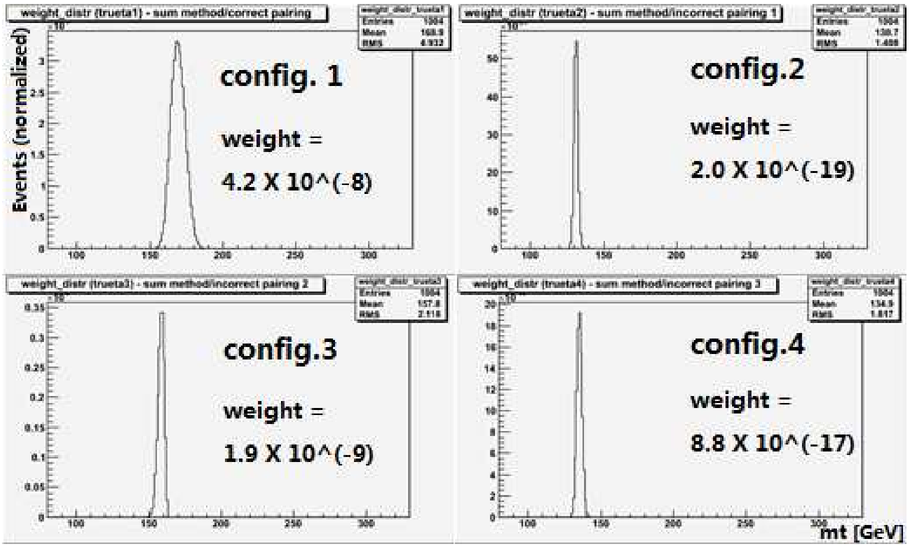

Figure 7.2. The weight distribution of a single MC $t\bar{t}$ event ($m_{\mathrm{t}}^{\mathrm{MC}}$=170 GeV) for four configurations of neutrino solutions with correct neutrino rapidities. Configuration 1 (top left) corresponds to two correct solutions, configuration 2 (top right) and 3 (bottom left) correspond to one correct and one incorrect solutions, configuration 4 (bottom right) corresponds to two incorrect solutions. The integrated weight of each configuration is shown in the plots.

Table 7.1: Truth level neutrino momenta and all neutrino solutions with correct jet assignment and correct neutrino η's.

truth level	P_x	P_y	P_z	η	Energy
ν	57.85	45	-26.88	-0.35	78.07
$\bar{\nu}$	48.77	-46.37	-1.81	-0.02	67.32
ν_1 soln 1	49.19	-50.14	-1.89	-0.02	70.26
ν_1 soln 2	-71.99	-133.62	-4.09	-0.02	151.84
ν_2 soln 1	58.06	46	-27.16	-0.35	78.9
ν_2 soln 2	-142.66	64.6	-57.43	-0.35	166.8

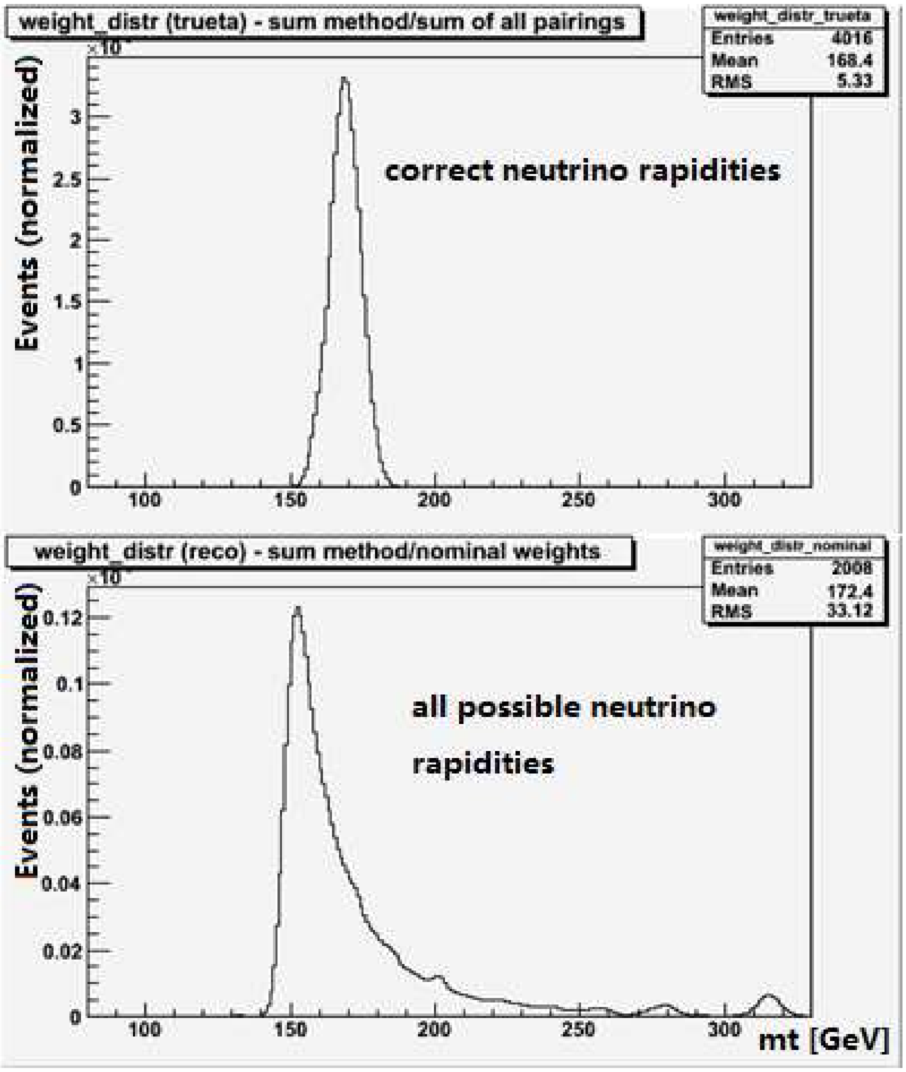

Figure 7.3. The weight distribution of a single MC $t\bar{t}$ event (m_t^{MC}=170 GeV) with correct neutrino rapidities (top) and all possible combinations of neutrino rapidities and jet assignments (bottom).

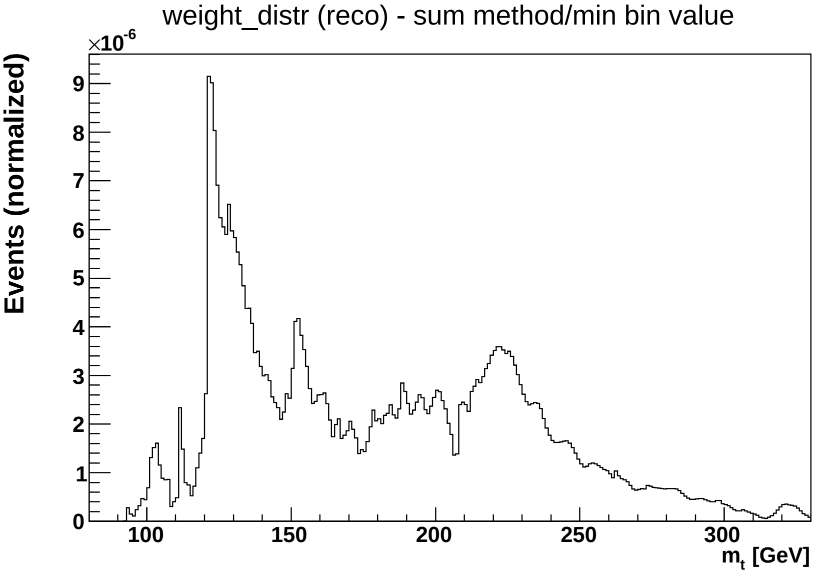

Figure 7.4. The weight distribution of a single MC diboson event with all possible combinations of neutrino rapidities and jet assignments.

Studies of the weight distribution have been performed at both the particle and the reconstructed levels, using Run II-B MC samples and an earlier version of the MC JES. The fully reconstructed leptons and jets are required to match to the particles within a cone of $\Delta R = 0.2$ and 0.5, respectively. With correct jet assignment, the RMS of the weight distribution improves by 20.4% for the particle level and 18.4% for the reconstructed level. The sum of weight distribution for 298k $t\bar{t}$ MC events ($m_{\mathrm{t}}^{\mathrm{MC}}$=172.5 GeV) are shown in Fig. 7.5 for solutions that are closest to the true ν momenta with correct jet assignment ("correct" solutions). With correct jet assignment and correct neutrino solutions (solutions that give least discrepancy from truth level), the RMS of weight distribution for signal improves by 31.1% at particle level and 23.3% at the reconstructed level.

Since we do not have truth information in data, we need an observable which can indicate when we have a correct solution. One way to utilize the particle information is to construct probability density distributions from the RMS of weight distribution (see Fig. 7.6), separated according to correct and incorrect jet assignments. The RMS exhibits a peak around 10 GeV in the truth level and 5 GeV in the reconstructed level for the correct jet assignment, while for the incorrect assignment the RMS peaks at zero. The RMS probability of correct assignment is larger than the one for incorrect assignment for RMS $>$ 6 GeV for both truth and reconstructed levels. This implies that the RMS may be a useful tool to discriminate correct and incorrect assignments. I tried several schemes, and one way used the RMS (see Fig. 7.6) to rescale weight distributions, as shown in Fig. 7.7. Fig. 7.6 shows that correct assignment tends to peak at 10 GeV for truth level and 6 GeV for reconstruction level, while the incorrect assignment peaks near 0 GeV. The relative weight from these RMS distributions is calculated from the product of the probabilities of the two assignments for correct+incorrect possibility and incorrect+correct possibility. A 10%

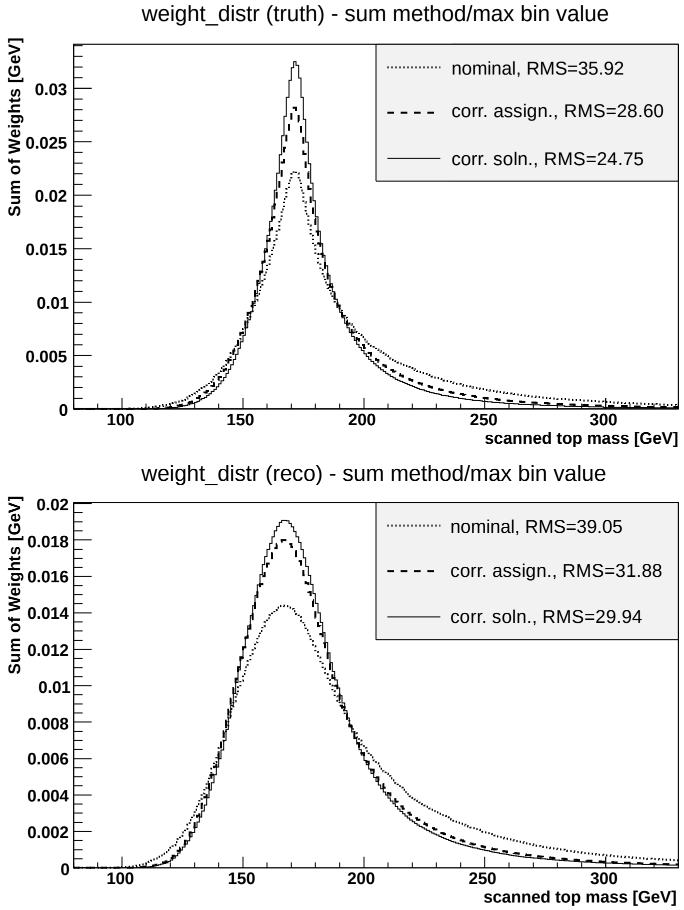

Figure 7.5. Weight distributions of $m_{\mathrm{t}}^{\mathrm{MC}}$=172.5 GeV sample at truth level (top) and reconstruction level (bottom) using nominal method (dotted), correct jet assignments (dashed) and correct neutrino solutions + correct jet assignment (solid).

improvement is expected at the truth level and 9% at the reconstructed level through this reweighting (see Tab. 7.2). The studies on jet assignments and ν solutions show that the resolution for the distribution of weights can improve by restricting wrong assignments/solutions. This result suggested limiting the low-weight solutions by restricting the scanned m_{t} range as discussed in Sec. 7.3.

Table 7.2: The RMS of the distribution summed from all single event weight distribution for $m_{\mathrm{t}}^{\mathrm{MC}}$=172.5 GeV sample at truth level and reconstruction level with nominal method, correct solutions and assignment, and after applying the RMS weighting.

method	nominal[GeV]	correct soln.+assign.[GeV]	RMS weighting[GeV]
truth level	35.92	24.75	32.31
reco. level	39.05	29.94	35.54

7.2. Impact of b-tagging

In previous 4.3 fb^{-1} analysis [82], no b-tagging was applied. While in current 9.7 fb^{-1} analysis, the MVA$_{bl}$ algorithm is employed to discriminate b-jets from light quark jets. This causes 15% loss of $t\bar{t}$ events. However, the background drops dramatically and the expected statistical uncertainty on m_t is improved by about 7%. The specific cuts used in the MVA$_{bl}$ b-tagging is discussed in Sec. 7.3 for each dilepton channel.

7.3. Optimization of Different Parameters in the Method

When solving the problem of wrong solutions/assignments, the study in Sec. 7.1 suggests an analysis of the parameters that affect the weights and the relative contribution of correct and incorrect configurations. Such parameters include the resolution

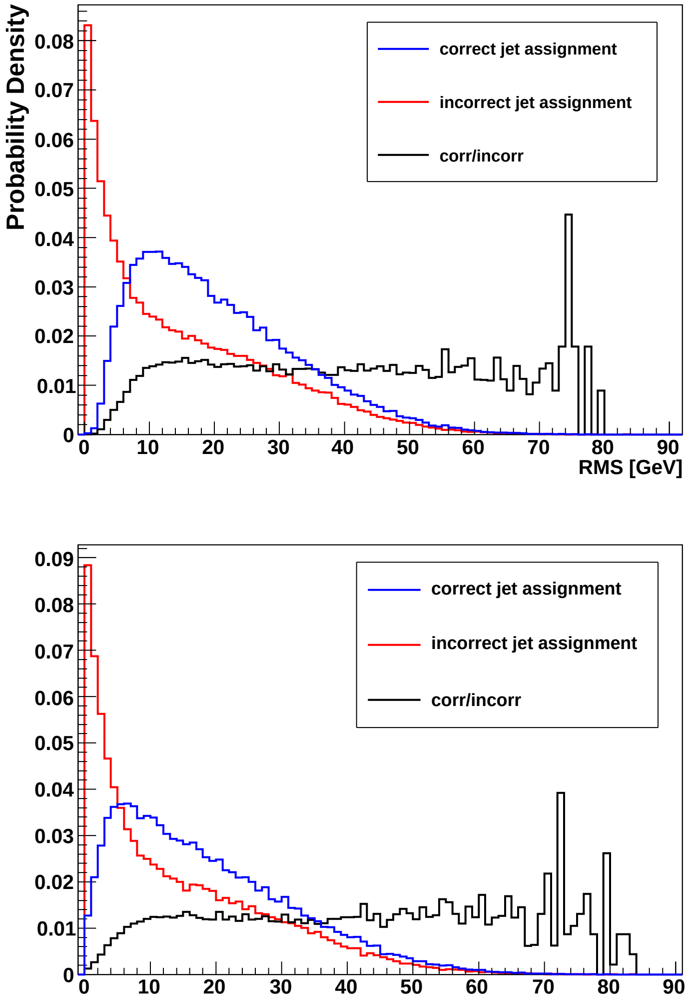

Figure 7.6. The RMS of weight distribution for $m_{\mathrm{t}}^{\mathrm{MC}}$=172.5 GeV sample at truth level (top) and reconstruction level (bottom). The RMS is separately plotted for correct and incorrect jet assignments, and for a ratio between correct and incorrect assignments.

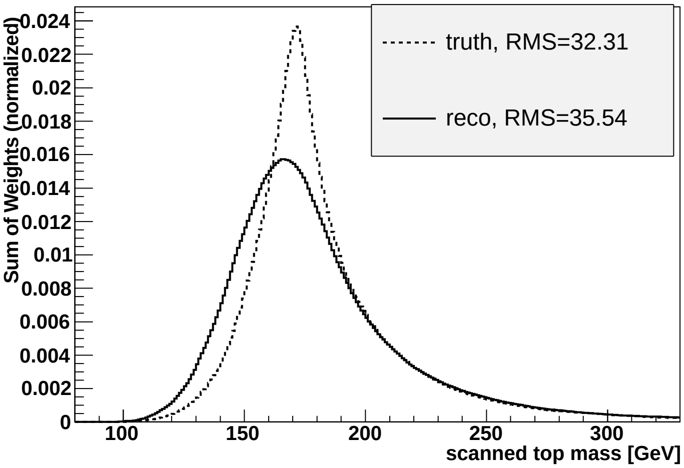

Figure 7.7. Summed distribution of all single event weight distributions for $m_{\mathrm{t}}^{\mathrm{MC}}$=172.5 GeV sample at truth level (dashed) and reconstruction level (solid) with RMS of weight distribution employed as the weighting basis. The truth level has a RMS of 32.31 and reconstruction level is 35.54.

of $\not{E}^{\mathrm{unc}}$ and the chosen m_{t} range. We broadened the study to other parameters of the analysis, including binning of the templates, event selection, parabolic fit range, and the number of pseudoexperiments. I performed all these studies using the 9.7 fb^{-1} of MC samples. Each optimization is evaluated after previous ones implemented.

Since the expected statistical uncertainties are determined within some nonnegligible statistical uncertainty, which is about 0.03 GeV for the $e\mu$ channel and 0.05 GeV for the ee and $\mu\mu$ channels, picking the optimal point from the one giving minimual expected statistical uncertainty is not reliable for a precise measurement. Thus the optimal parameters in this analysis are picked with the following three algorithms: 1) for 1-parameter case, e.g. the unclustered $\not{E}_T$ resolution, a third order polynomial is employed to fit all trials and the point closest to fitted minimum of expected statistical uncertainty is picked. 2) for 2-parameter case, e.g. the template binning study, the expected statistical uncertainty in each row and column are summed together and the point with the smallest sum in each dimension is picked. 3) for 3-parameter case, e.g. the kinematic cut study in the ee and $\mu\mu$ channels, all the expected statistical uncertainty associated with one of the several scanned values of a parameter are summed, meaning that the 3-D parameter space is projected into 1-D. The point with the smallest sum in each parameter is picked.

The optimization can be grouped into three categories : weight calculation, event selection and likelihood calculation. The 172.5 GeV MC sample is not included in the weight calculation optimization to prevent biases in mass range study, and is included for the other two optimizations.

7.3.1. Weight calculation

- *Resolution in unclustered $\not{E}_T$:* The resolution in $\not{E}^{\mathrm{unc}}$ can be implemented both using a linear dependence on the square root of $S_{\not{E}_T}$ or as a $S_{\not{E}_T}$-independent constant. In tests using different resolutions in the weight calculation, the mass analysis was found to be insensitive to modest changes in this value and whether it had a $S_{\not{E}_T}$ dependence. On top of the unclustered energy, the calculated $\not{E}_T$ and reconstructed $\not{E}_T$ could be off due to extra jets in the events, or discrete values of scanned m_t and neutrino rapidities. Since the reconstructed $\not{E}_T$ is derived from all calorimeter cells, it contains the information of extra jets while the calculated $\not{E}_T$ involves only two leading jets, resulting in more deviation between the reconstructed $\not{E}_T$ and the calculated $\not{E}_T$. The discrete segmentation of scanned m_t and neutrino rapidity values makes it hard to match with the truth values of m_t and neutrino rapidity perfectly. The effect of this segmentation can cause up to 5 GeV level deviation between the reconstructed $\not{E}_T$ and the calculated $\not{E}_T$. Therefore, the parameterization of $\sigma_{\not{E}_{x,y}}$ needs to be generalized to include these effects. Comparing a range of trials with a $S_{\not{E}_T}$-independent parameterization as well as linear parameterizations, we observe $S_{\not{E}_T}$-independent behaviors as shown in Table 7.3. By fitting the $S_{\not{E}_T}$-independent parameterizations with a third order polynomial, we find 25.9 GeV as the minimum. Therefore, we choose the $S_{\not{E}_T}$-independent parameterization of 25 GeV to optimize the expected statistical uncertainties, which provides an 5% improvement to the expected statistical uncertainty in the $e\mu$ channel. This parameter does not create bias if it is chosen nonoptimally, because the maximum likelihood approach discussed below adjusts for the bias.

- *Scanned* m_{t} *range:* In the nominal analysis, the scanned m_{t} range in the weight calculation was determined based on the mass limits set by the mass of the W boson for low end and the SM unitary for high end (as deduced in the 1990s).

Table 7.3: Expected statistical uncertainty (GeV) for 175 GeV input m_{t} with various flat $\sigma_{\not{E}_{x,y}^{\mathrm{unc}}}$ using $e\mu$ events of Run II MC samples. The linear parameterization is obtained using $e\mu$ events of Run II-B MC samples as shown in Fig. 6.4. The previous 4.3 fb^{-1} analysis used 7 GeV as the parameterization, and 25 GeV is finally chosen as parameterization of the $\sigma_{\not{E}_{x,y}^{\mathrm{unc}}}$ for the 9.7 fb^{-1} analysis.

$\sigma_{\not{E}_{x,y}}[GeV]$	4	7	10	15	20	25	30	40	100	linear
stat. err. [GeV]	2.20	2.17	2.13	2.07	2.07	2.06	2.05	2.08	2.24	2.31

The range was chosen to be 80-330 GeV. In fact, the m_{t} range is optimizable since it affects the proportion of “correct” and “incorrect” jet assignments and ν solutions. A proper amount of “incorrect” solutions can help discriminate weight distributions for $t\bar{t}$ events with different $m_{\mathrm{t}}^{\mathrm{MC}}$. By extending the mass range from 80-330 GeV, the expected statistical uncertainty is found to be not affected within 0.03 GeV statistical component of the statistical uncertainty, so we turn to limit the range. The low end and high end of the mass range are determined independently by scanning 100-170 GeV and 180-300 GeV, respectively. By summing over the expected statistical uncertainties for each low end and high end of the tested m_{t} ranges as shown in Table 7.14, we find 115-220 GeV to be the optimal range. The improvement in expected statistical uncertainty is about 6% for the $e\mu$ events.

7.3.2. Event Selection

- *Event Selection:* For fixed luminosity, getting more signal statistics and getting better signal-to-background ratio usually go in a contrary way, a balance be-

Table 7.4: Expected statistical uncertainty (GeV) for 175 GeV inputm_{t} with different mass ranges using $e\mu$ events of Run II MC samples. The mass range is optimized to 115-220 GeV from previous setup 80-330 GeV.

high/low	100	110	115	120	125	130	140	150	170	sum
180	2.01	2.01	1.99	2.03	2.02	2.00	2.00	2.12	-	-
190	1.94	1.93	1.93	1.93	1.95	1.96	1.98	2.28	4.55	27.30
200	1.91	1.92	1.92	1.93	1.94	1.94	1.94	2.10	4.17	26.25
205	1.95	1.94	1.92	1.95	1.93	1.95	1.96	2.10	4.46	26.51
210	1.94	1.94	1.93	1.94	1.94	1.93	1.96	2.10	4.17	26.34
215	1.92	1.93	1.91	1.93	1.92	1.93	1.94	2.10	3.98	26.13
220	1.93	1.93	1.94	1.94	1.93	1.93	1.94	2.09	3.89	26.10
225	1.95	1.93	1.93	1.93	1.92	1.94	1.95	2.09	3.98	26.22
230	1.95	1.94	1.94	1.95	1.95	1.94	1.95	2.11	3.93	26.28
235	1.93	1.94	1.94	1.95	1.98	1.95	1.98	2.14	3.87	26.42
240	1.97	1.96	1.95	1.97	1.97	1.97	1.98	2.15	3.92	26.62
250	1.97	1.97	1.98	1.96	1.97	2.00	2.00	2.18	4.05	26.97
260	1.98	1.96	1.98	1.99	2.01	1.99	2.03	2.23	4.07	27.23
270	1.99	1.98	2.00	1.99	2.00	2.00	2.03	2.23	4.08	27.36
280	2.01	2.03	1.99	2.02	2.03	2.03	2.06	2.24	4.11	27.62
290	2.02	2.03	2.04	2.03	2.02	2.04	2.08	2.26	4.18	27.91
300	2.02	2.03	2.01	2.02	2.03	2.02	2.07	2.28	4.22	27.98
sum	33.39	33.37	33.30	33.46	33.51	33.52	33.85	36.80	63.63	

tween the two has to be studied. Since H_T, $\not\!\!E_T$ and $\not\!\!E_T$ significance significance, and b-tagging all affect the number of events in the samples, we determine these cuts simultaneously by studying a 2-D or 3-D parameter space. The 2-D space for the $e\mu$ channel is shown in Table 7.5, and one slice of the 3-D space is shown in Table 7.6 for the ee channel with maxMVA cut at 0.05, and in Table 7.7 for the $\mu\mu$ channel with maxMVA cut at 0.05. The full list of tables for the ee and $\mu\mu$ channels are shown in Appendix B for all tested maxMVA cuts.

Table 7.5: Expected statistical uncertainty (GeV) with 172.5 GeV input m_t for different maxMVA cuts and H_T cuts in the $e\mu$ channel. The final cut on maxMVA in the $e\mu$ channel is determined to be 0.03, and the H_T cut is determined to be 100 GeV.

maxMVA/H_T	100	110	120	130	140	150	160	170	sum
0.02	1.87	1.86	1.91	1.97	2.05	2.16	2.29	2.52	16.63
0.03	1.85	1.86	1.91	1.96	2.05	2.16	2.28	2.49	16.56
0.04	1.88	1.90	1.91	1.96	2.07	2.20	2.30	2.48	16.70
0.05	1.88	1.90	1.92	1.99	2.10	2.20	2.31	2.50	16.80
0.06	1.91	1.90	1.96	2.00	2.10	2.19	2.30	2.53	16.89
0.07	1.92	1.94	1.97	2.00	2.11	2.21	2.35	2.52	17.02
0.08	1.92	1.92	1.94	2.03	2.11	2.23	2.34	2.52	17.01
sum	13.23	13.28	13.52	13.91	14.59	15.35	16.17	17.56	

Table 7.6: Expected statistical uncertainty (GeV) with 172.5 GeV input m_t for different $\not\!\!E_T$ cuts in Z mass window and $\not\!\!E_T$ significance cuts and maxMVA cut at 0.05 in the ee channel. The final cut on $\not\!\!E_T$ in the ee channel is determined to be 40 GeV for events in Z mass window 70-110 GeV, and the $\not\!\!E_T$ significance cut is determined to be 3.5.

$\not\!\!E_T/\not\!\!E_T$ sig.	3.5	4	4.5	5	5.5	sum
20	3.37	3.38	3.37	3.39	3.37	16.88
30	3.29	3.25	3.29	3.40	3.31	16.54
40	3.19	3.26	3.30	3.32	3.35	16.42
50	3.25	3.31	3.39	3.41	3.41	16.77
60	3.36	3.40	3.50	3.51	3.51	17.28
sum	16.46	16.60	16.85	17.03	16.95	

Table 7.7: Expected statistical uncertainty (GeV) with 172.5 GeV input m_t for different $\not\!\!E_T$ cuts and $\not\!\!E_T$ significance cuts and maxMVA cut at 0.05 in the $\mu\mu$ channel. The final cut on $\not\!\!E_T$ in the $\mu\mu$ channel is determined to be 40 GeV, and the $\not\!\!E_T$ significance cut is determined to be 4.

$\not\!\!E_T/\not\!\!E_T$ sig.	2	3	4	5	6	7	8	sum
20	4.15	3.87	3.64	3.67	3.62	3.78	3.90	26.63
30	3.85	3.73	3.60	3.58	3.63	3.85	3.90	26.14
40	3.61	3.57	3.58	3.56	3.56	3.87	3.91	25.66
50	3.54	3.57	3.66	3.64	3.69	3.85	3.93	25.88
60	3.73	3.70	3.78	3.84	3.89	3.99	4.02	26.95
sum	18.88	18.44	18.26	18.29	18.39	19.34	19.66	

7.3.3. Likelihood Calculation

- *Parabolic Fit Range:* The $-\log\mathcal{L}$ vs. $m_{\mathrm{t}}^{\mathrm{MC}}$ is not perfectly parabolic. Therefore the fit range is optimizable in balancing the performance of the fit. In the nominal analysis, the fit range was optimized to be 15 GeV for the ee, $e\mu$, and combined channels. It has been checked that this optimization still holds in the 9.7 fb^{-1} analysis. The $\mu\mu$ channel used a wider range of 25 GeV in the nominal analysis due to low statistics. The increased $\mu\mu$ events requires this parameter to be redetermined. We look at the expected statistical uncertainties with 4 different fit ranges: 10 GeV, 15 GeV, 20 GeV, and 25 GeV. We find 15 GeV gives the best estimation of statistical uncertainty, and therefore is picked as the new fit range for the $\mu\mu$ channel.

Table 7.8: Expected statistical uncertainty (GeV) with 172.5 GeV input m_{t} for different fit ranges in the $\mu\mu$ channel. The final fit range in $\mu\mu$ channel is determined to be 15 GeV.

fit range [GeV]	10	15	20	25
stat. err. [GeV]	3.52	3.51	3.53	3.58

- *Template binning:* The statistics of MC samples has been largely increased over previous analysis. Thus the binning of the templates should be redetermined accordingly. The μ_w and σ_w dimensions are segmented independently and expected statistical uncertainties are filled into a 2D table (Tabs. 7.9 - 7.13) for all binning trials. A coarse binning is firstly probed, and then based on it a fine binning is performed in the optimal range. Since the $e\mu$ channel has 3X the data of *ee* or $\mu\mu$ channel, and the muon resolution is relatively worse than electron resolution, so the binning of the templates is determined separately in each individual channel, and the fine binning of $\mu\mu$ channel is based on the coarse binning in the *ee* channel. We replaced the previous binning of (15, 6)[GeV] with (3, 2) [GeV], (5, 3) [GeV] and (5.5, 1.75) [GeV] as the widths of μ_w and σ_w for the $e\mu$, *ee* and $\mu\mu$ channels (see Figs. 6.9- 6.10). The expected statistical uncertainty is improved by about 10% in the $e\mu$ channel.

Table 7.9: Table of coarse template binnings and corresponding expected statistical uncertainties at $m_{\mathrm{t}}^{\mathrm{MC}}$=172.5 GeV using $e\mu$ events of Run II MC samples. The bin size in this table is rounded to 0.5 GeV.

μ_w/σ_w	12	6	3.5	2	1.5	1	sum
50.00	2.22	2.06	2.06	2.05	2.04	2.03	12.46
25.00	2.06	1.95	1.92	1.92	1.91	1.91	11.67
15.00	1.95	1.85	1.83	1.83	1.83	1.83	11.12
12.00	1.92	1.82	1.81	1.80	1.80	1.80	10.95
8.00	1.88	1.79	1.79	1.77	1.77	1.77	10.77
6.50	1.87	1.79	1.79	1.77	1.77	1.76	10.75
5.00	1.88	1.79	1.79	1.77	1.76	1.76	10.75
3.50	1.86	1.78	1.77	1.76	1.76	1.76	10.69
2.50	1.86	1.78	1.77	1.75	1.75	1.76	10.67
1.50	1.85	1.78	1.77	1.76	1.76	1.76	10.68
1.00	1.85	1.77	1.76	1.76	1.76	1.79	10.69
sum	21.20	20.16	20.06	19.94	19.91	19.93	

Table 7.10: Table of fine template binnings and corresponding expected statistical uncertainties at $m_{\mathrm{t}}^{\mathrm{MC}}$=172.5 GeV using $e\mu$ events of Run II MC samples. The bin size in this table is rounded to 0.25 GeV.

μ_w/σ_w	3.5	3	2.5	2	1.75	1.5	1.25	1	0.5	sum
8.00	1.79	1.78	1.77	1.77	1.78	1.78	1.76	1.77	1.77	15.97
7.00	1.79	1.78	1.77	1.76	1.77	1.78	1.77	1.76	1.76	15.94
6.00	1.78	1.77	1.76	1.76	1.77	1.77	1.76	1.76	1.76	15.89
5.00	1.79	1.77	1.77	1.77	1.78	1.77	1.77	1.76	1.77	15.95
4.00	1.77	1.77	1.77	1.76	1.77	1.77	1.76	1.77	1.78	15.92
3.50	1.77	1.76	1.76	1.75	1.76	1.76	1.76	1.76	1.77	15.85
3.00	1.77	1.76	1.77	1.75	1.76	1.76	1.76	1.76	1.76	15.85
2.50	1.77	1.76	1.76	1.75	1.76	1.76	1.76	1.76	1.78	15.86
2.00	1.76	1.76	1.77	1.76	1.76	1.77	1.78	1.76	1.79	15.91
1.75	1.76	1.76	1.76	1.75	1.77	1.76	1.77	1.77	1.81	15.91
1.50	1.76	1.76	1.77	1.75	1.76	1.77	1.77	1.77	1.82	15.93
1.25	1.76	1.76	1.76	1.75	1.76	1.77	1.77	1.78	1.83	15.94
1.00	1.76	1.76	1.77	1.76	1.76	1.77	1.78	1.79	1.87	16.02
0.50	1.78	1.78	1.79	1.78	1.79	1.79	1.84	1.86	2.01	16.42
sum	24.81	24.73	24.75	24.62	24.75	24.78	24.81	24.83	25.28	

Table 7.11: Table of coarse template binnings and corresponding expected statistical uncertainties at $m_{\mathrm{t}}^{\mathrm{MC}}$=172.5 GeV using *ee* events of Run II MC samples. The bin size in this table is rounded to 0.5 GeV.

μ_w/σ_w	12	6	3.5	2	1.5	1	sum
50.00	3.86	3.55	3.46	3.46	3.42	3.44	21.19
25.00	3.55	3.31	3.24	3.25	3.24	3.23	19.82
15.00	3.40	3.19	3.16	3.13	3.13	3.13	19.14
12.00	3.32	3.13	3.10	3.08	3.05	3.07	18.75
8.00	3.27	3.08	3.05	3.04	3.04	3.06	18.54
6.50	3.25	3.07	3.04	3.03	3.02	3.05	18.46
5.00	3.23	3.06	3.03	3.02	3.01	3.03	18.38
3.50	3.23	3.07	3.04	3.04	3.04	3.06	18.48
2.50	3.21	3.05	3.04	3.05	3.04	3.11	18.50
1.50	3.22	3.05	3.05	3.09	3.14	3.17	18.72
1.00	3.24	3.07	3.06	3.13	3.26	3.29	19.05
sum	36.78	34.63	34.27	34.32	34.39	34.64	

Table 7.12: Table of fine template binnings and corresponding expected statistical uncertainties at $m_{\mathrm{t}}^{\mathrm{MC}}$=172.5 GeV using *ee* events of Run II MC samples. The bin size in this table is rounded to 0.25 GeV.

μ_w/σ_w	4.5	4	3.5	3	2.5	2	1.75	1.5	1.25	sum
10.00	3.07	3.09	3.08	3.07	3.07	3.07	3.08	3.08	3.07	27.68
9.00	3.07	3.08	3.06	3.06	3.06	3.06	3.05	3.07	3.05	27.56
8.00	3.06	3.06	3.07	3.06	3.05	3.05	3.05	3.05	3.05	27.50
7.50	3.06	3.06	3.05	3.04	3.04	3.04	3.05	3.04	3.04	27.42
7.00	3.04	3.04	3.04	3.03	3.04	3.04	3.03	3.03	3.05	27.34
6.75	3.05	3.04	3.05	3.03	3.03	3.04	3.04	3.04	3.04	27.36
6.50	3.05	3.05	3.05	3.03	3.03	3.03	3.03	3.03	3.04	27.34
6.25	3.05	3.05	3.04	3.02	3.03	3.03	3.03	3.03	3.04	27.32
6.00	3.05	3.04	3.04	3.03	3.03	3.03	3.03	3.04	3.03	27.32
5.50	3.04	3.04	3.03	3.02	3.03	3.04	3.04	3.03	3.04	27.31
5.00	3.03	3.03	3.03	3.02	3.01	3.02	3.04	3.03	3.03	27.24
4.50	3.04	3.04	3.04	3.02	3.03	3.03	3.04	3.04	3.03	27.31
4.00	3.03	3.02	3.04	3.01	3.03	3.02	3.04	3.04	3.04	27.27
3.50	3.03	3.04	3.03	3.03	3.03	3.04	3.04	3.03	3.05	27.32
3.00	3.03	3.02	3.03	3.03	3.03	3.04	3.05	3.05	3.07	27.35
2.00	3.05	3.04	3.04	3.04	3.04	3.07	3.06	3.07	3.09	27.50
sum	48.75	48.74	48.72	48.54	48.58	48.65	48.70	48.70	48.76	

Table 7.13: Table of fine template binnings and corresponding expected statistical uncertainties at $m_{\mathrm{t}}^{\mathrm{MC}}$=172.5 GeV using $\mu\mu$ events of Run II MC samples. The bin size in this table is rounded to 0.25 GeV.

μ_w/σ_w	4.5	4	3.5	3	2.5	2	1.75	1.5	1.25	sum
10.00	3.41	3.40	3.39	3.40	3.39	3.38	3.38	3.39	3.38	30.52
9.00	3.38	3.38	3.37	3.34	3.36	3.36	3.34	3.33	3.36	30.22
8.00	3.39	3.38	3.37	3.36	3.38	3.37	3.35	3.38	3.38	30.36
7.50	3.38	3.38	3.36	3.35	3.36	3.37	3.33	3.35	3.38	30.26
7.00	3.37	3.37	3.35	3.37	3.35	3.37	3.33	3.34	3.32	30.17
6.75	3.36	3.36	3.36	3.33	3.35	3.35	3.38	3.34	3.37	30.20
6.50	3.38	3.38	3.36	3.36	3.36	3.35	3.33	3.33	3.33	30.18
6.25	3.37	3.37	3.36	3.35	3.36	3.35	3.34	3.35	3.35	30.20
6.00	3.37	3.36	3.35	3.35	3.35	3.35	3.33	3.34	3.33	30.13
5.50	3.36	3.37	3.34	3.33	3.35	3.34	3.34	3.33	3.32	30.08
5.00	3.38	3.37	3.35	3.37	3.36	3.36	3.35	3.36	3.36	30.26
4.50	3.36	3.35	3.35	3.36	3.38	3.37	3.37	3.36	3.35	30.25
4.00	3.36	3.37	3.35	3.34	3.34	3.36	3.33	3.35	3.35	30.15
3.50	3.36	3.34	3.33	3.34	3.34	3.36	3.33	3.36	3.35	30.11
3.00	3.38	3.37	3.35	3.36	3.37	3.36	3.35	3.37	3.35	30.26
2.00	3.37	3.37	3.36	3.37	3.39	3.35	3.39	3.39	3.40	30.39
sum	53.98	53.92	53.70	53.68	53.79	53.75	53.57	53.67	53.68	

- *Number of pseudoexperiments:* Finite number of PEs can result in larger fluctuations in systematic uncertainty determination. This, in turn, will tend to inflate the overall uncertainty which is taken as a sum. A proper number of pseudoexperiments would reduce the fluctuation of expected statistical and systematic uncertainties without causing bias due to oversampling of limited samples. The systematic uncertainties are more sensitive to the number of pseudoexperiments than statistical uncertainty since only two or three $t\bar{t}$ samples are used, while the statistical uncertainty involves eight in the calibration and they jointly reduces the fluctuation. To determine an optimal number of pseudoexperiments, we look into all signal modeling uncertainties, object reconstruction and identification uncertainties, and two JES uncertainties of all systematic uncertainties summed in quadrature. We estimate the fitted m_{t} from each systematic sample and calculate the RMS from 10 different random seeds for each sample as shown in Table. 7.14. Tests with different number of PEs show that most of the RMS's of fitted m_{t} descend with the number of PEs growing. No gain is evident beyond 3000 PEs, so we optimize on this choice. The $\mu\mu$ channel is considered to have similar performance as ee channel since their statistics are very close.

Table 7.14: RMS [GeV] of m_{t}^{fit} estimated from 10 different random seeds for the default 172.5 GeV sample in $e\mu$ and ee channels. The systematic uncertainties used in this study are signal modeling uncertainties, object reconstruction and identification uncertainties, and a couple of JES uncertainties.

# of P.E.s	1200	2000	2400	3000	3500	4000
$e\mu$	0.044	0.037	0.029	0.029	0.027	0.028
ee	0.121	0.104	0.086	0.067	0.073	0.069

The above optimizations have been performed sequentially as listed in this section, and an overall net 25% improvement is obtained in the end. This includes the 7% improvement from implementing b-tagging. The cross checks executed later show that these optimizations are not strongly correlated. A summary of all optimizations is shown in Table 7.15 with previous and new nominal settings listed together.

Table 7.15: Summary of the parameters in the nominal and optimized analysis shown separately before and after a rising slash (/). $*$The $\not{E}_T$ cut in the ee channel is performed for events with the invariant mass of the two leptons in the Z boson mass window 70-110 GeV.

Parameter	ee	$e\mu$	$\mu\mu$
$\sigma_{\not{E}_{x,y}}$	7/25		
scanned m_t range	$(80, 330)/(115, 220)$		
number of P.E.	1000/3000		
template binning (μ_w,σ_w)	(15,6)/(5,3)	(15,6)/(3,2)	(15,6)/(5.5,1.75)
fit range	15/15	15/15	25/15
H_T	-	120/100	-
$\not{E}_T$	40$*$	-	40/40
$\not{E}_T$ significance	5.0/3.5	-	5.0/4.0
maxMVA	0.05	0.03	0.05

7.4. Statistical Performance

As indicated in Fig. 6.11, the calibration suffers from high χ^2/ndf. The ee channel has an acceptable χ^2/ndf of 13.13/6, but $e\mu$, $\mu\mu$ and combined channels are up to 35.58/6, 17.52/6 and 26.34/6 respectively. Prior work [90] revealed this mainly originates from the finite statistics of signal templates. To address the issue, we estimate an oversampling correction [91] [92] by calculating the RMS of fitted m_{t} from 100 PEs. Each PE uses the very same events with signal templates fluctuated according to their statistical uncertainties. This study is done using the $t\bar{t}$ samples with $m_{\mathrm{t}}^{\mathrm{MC}}$ = 172.5 GeV. The oversampling corrections are calculated to be 0.15 GeV for the $e\mu$ channel and 0.23 GeV for the $\mu\mu$ channel. We add these values in quadrature with the estimated error on m_{t} at each mass point in the $e\mu$ and $\mu\mu$ calibration diagrams. The combined channel adopts the value from the $e\mu$ channel. Note that this oversampling uncertainty is applied to correct for the oversampling in templates, which is different from the oversampling correction discussed in previous chapter, which corrects for oversampling events in ensemble tests. The calibration fits after optimization and correcting for finite statistics of signal templates are summarized in Table 7.16, and plots are shown in Figs. 7.8 - 7.9. The χ^2/ndf approach 1 as expected. In Fig. 7.10 are the expected statistical uncertainty for $m_{\mathrm{t}}^{\mathrm{MC}}$=175 GeV. By applying the optimizations, the expected statistical uncertainty is improved by about 25% across all dilepton channels.

Table 7.16: Calibration slope and offset of the 9.7 fb^{-1} analysis in Figs. 7.8 - 7.9, the pull width, and the mean value of the expected statistical uncertainty after calibration for the ee, $e\mu$, $\mu\mu$ and combined channels. The results are after all optimizations.

approach	slope	offset [GeV]	$\langle$pull width$\rangle$	expected $\langle\sigma_{m_{\mathrm{t}}}\rangle$ [GeV]
ee	0.984 ± 0.004	0.672 ± 0.038	0.994 ± 0.016	2.98
$e\mu$	0.985 ± 0.006	0.549 ± 0.064	0.998 ± 0.018	1.72
$\mu\mu$	0.989 ± 0.010	0.718 ± 0.100	1.005 ± 0.016	3.31
2ℓ	0.988 ± 0.006	0.617 ± 0.062	0.995 ± 0.018	1.35

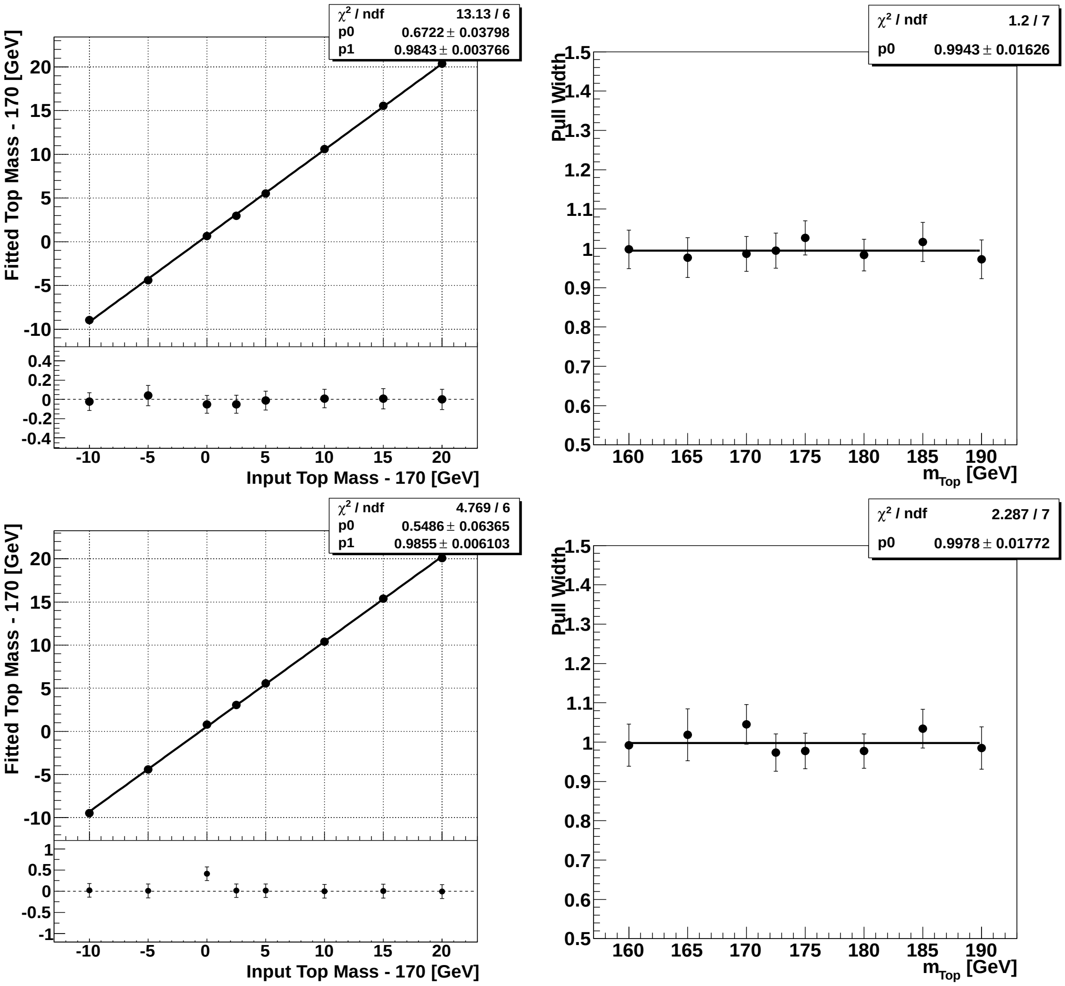

Figure 7.8. Calibrations of $m_{\rm t}$ after optimizations: (left) estimated $m_{\rm t}$ as a function of $m_{\rm t}^{\rm MC}$ and (right) the pull width as a function of $m_{\rm t}^{\rm MC}$ for the ee (top) and $e\mu$ (bottom) channels.

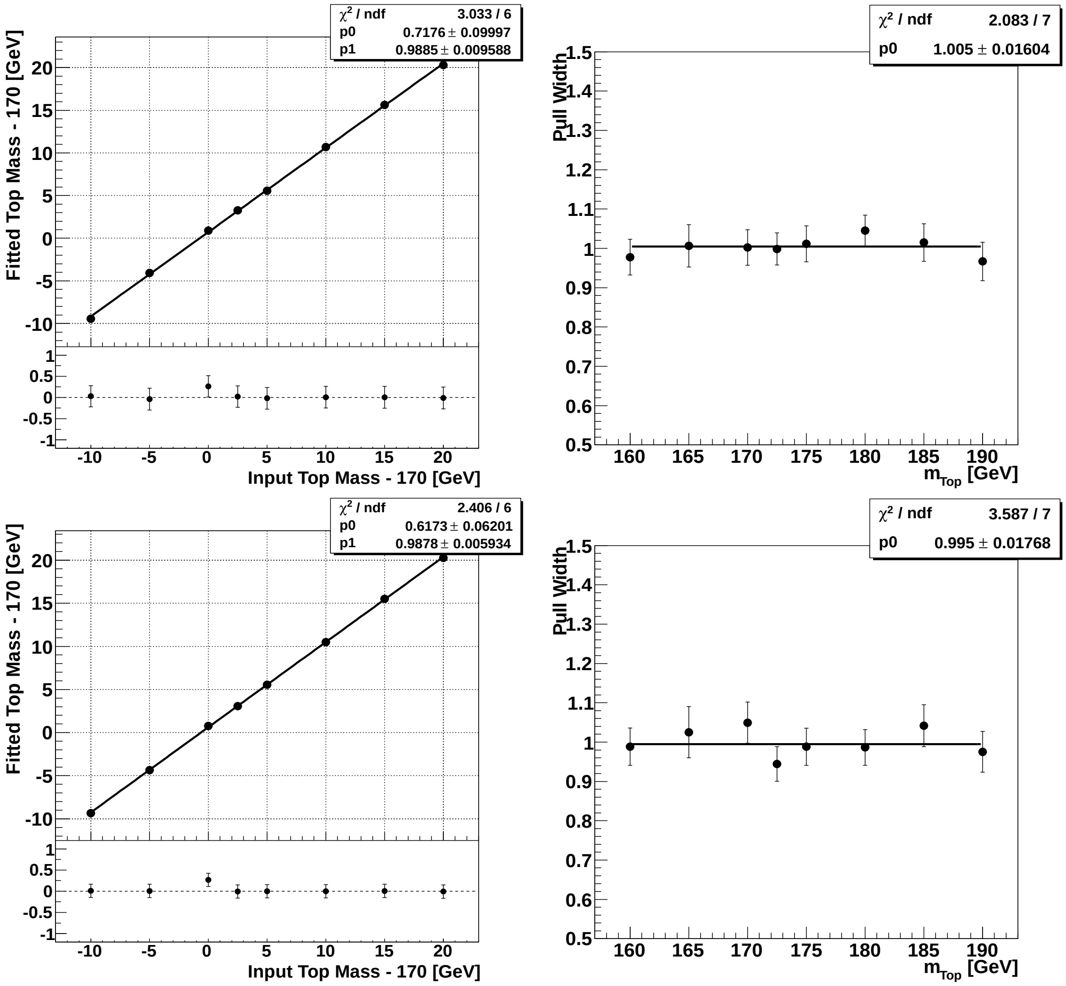

Figure 7.9. Calibrations of m_{t} after optimizations: (left) estimated m_{t} as a function of $m_{\mathrm{t}}^{\mathrm{MC}}$ and (right) the pull width as a function of $m_{\mathrm{t}}^{\mathrm{MC}}$ for the $\mu\mu$ (top) and combined (bottom) channels.

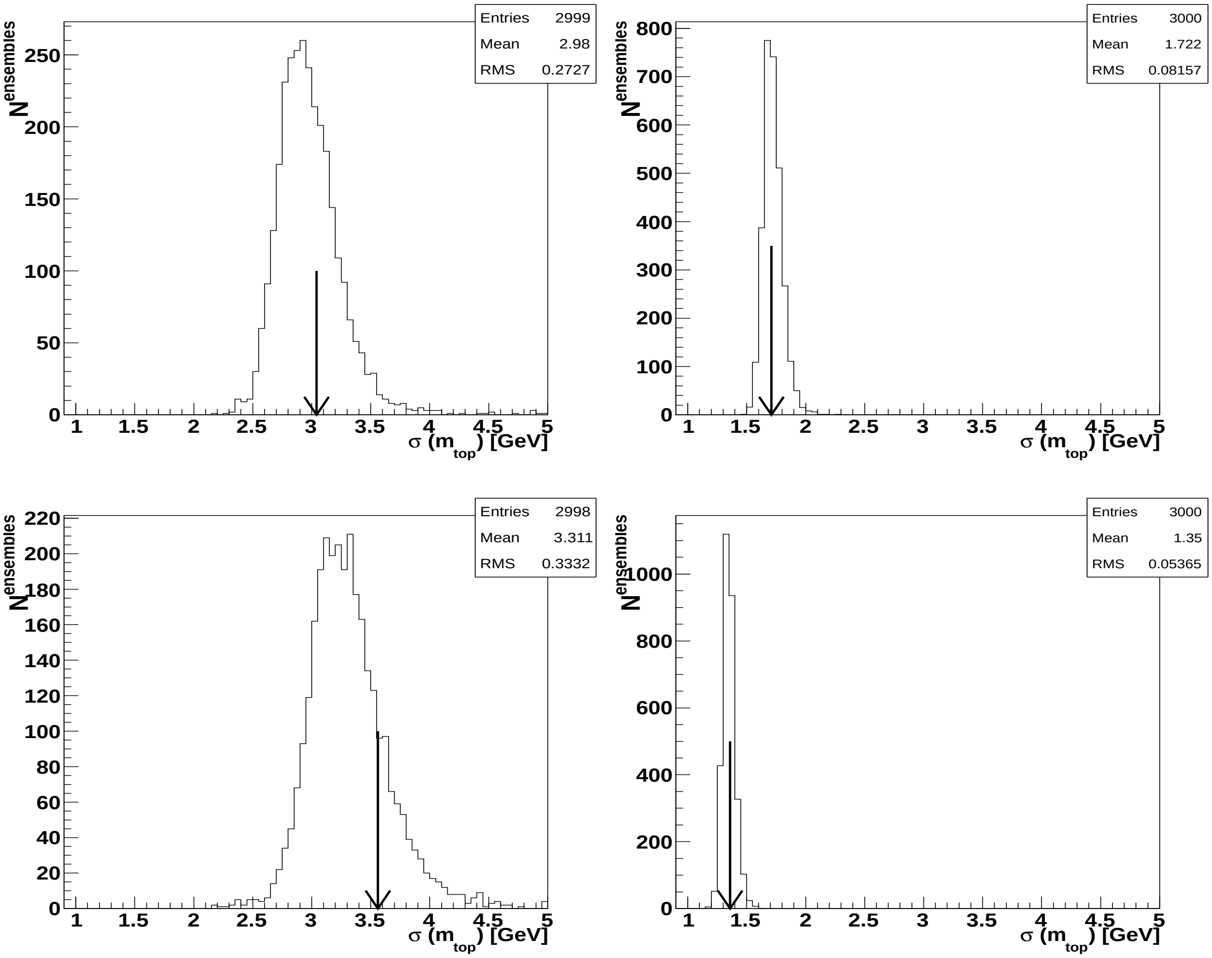

Figure 7.10. Distribution of expected statistical uncertainties after correcting for the pull width and slope for m_t^{MC}=175 GeV for the ee (top left), $e\mu$ (top right), $\mu\mu$ (bottom left) and combined (bottom right) channels with arrows indicating the measured statistical uncertainties from data.

Chapter 8

MEASUREMENT OF THE TOP QUARK MASS

8.1. Data Measurement

Using the methods discussed in Chapter 6 and optimal parameters determined in Chapter 7, which is based on the DØ note 6435 v2.5, the data measurement was originally performed with a blinded test, in which a random offset corresponding to a gaussian distribution with a 2 GeV σ is added to the measured top mass. After making all the cross-checks in this analysis, the offset was then removed. The unblinded, calibrated top quark mass and calibrated, pull-corrected statistical uncertainty for each dilepton channel is the following:

$$\begin{aligned} m_{\rm t}^{ee} &= 173.99 \pm 3.04 \text{ (stat) GeV}, \\ m_{\rm t}^{e\mu} &= 171.86 \pm 1.71 \text{ (stat) GeV, and} \\ m_{\rm t}^{\mu\mu} &= 178.58 \pm 3.56 \text{ (stat) GeV}. \end{aligned}$$

The combination of the measurements in all three dilepton channels is:

$$m_{\rm t}^{\rm combined} = 173.32 \pm 1.36 \text{ (stat) GeV}.$$

The negative log-likelihood and the parabolic fit are shown in Fig. 8.1.

8.2. Data-MC agreement

As a cross check, we evaluated the minimum of the $-\log \mathcal{L}$ with respect to different k_{JES} values. As shown in Table 8.1, the minimum of $-\log \mathcal{L}$ favors $k_{JES} = 1.025$ in

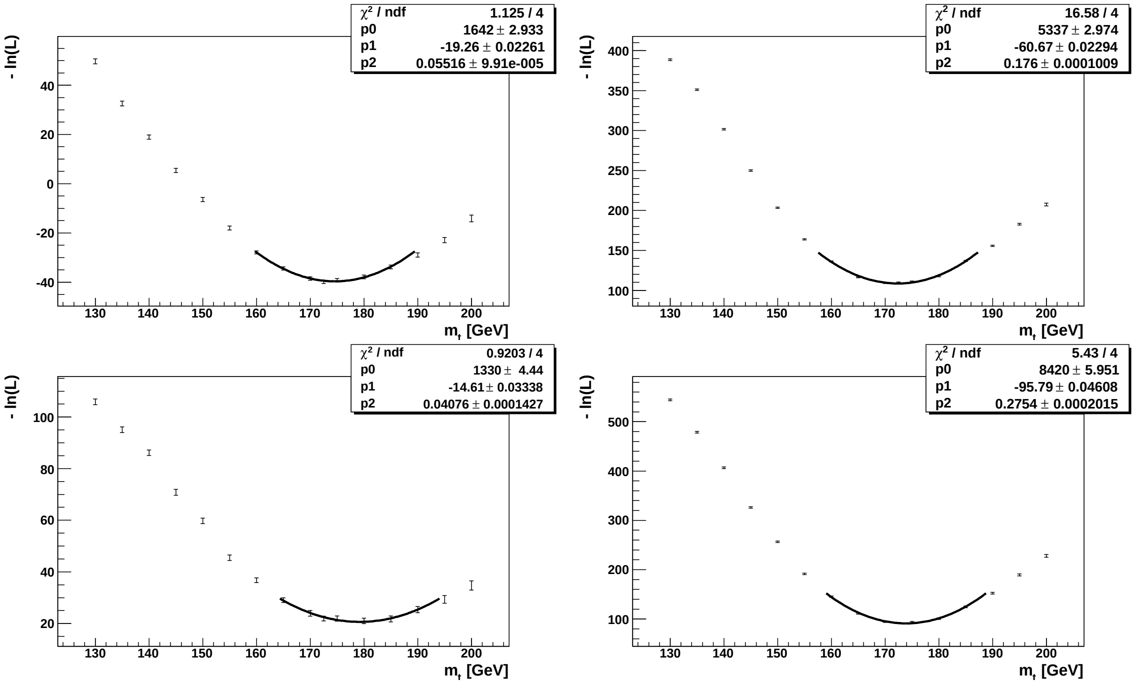

Figure 8.1. The $-\ln(L(m_t))$ as a function of m_t^{MC} for the ee (*top left*), $e\mu$ (*top right*), $\mu\mu$ (*bottom left*) channels and their combination (*bottom right*). The minimum of the parabola represents the estimated m_t before calibration.) and combined (bottom right) channels.

the $e\mu$ channel with an uncertainty of 6, which is a clear indication that the k_{JES} improves the data and MC agreement and is applicable to the dilepton b jets. There is no clear pattern for the ee, $\mu\mu$ channels and the combination since the uncertainties of their minimum are relatively much larger, being 6, 9 and 12, respectively. This pattern is due to the assumption that the mass of a top quark equals the mass of an antitop quark. The correlation between the two b jets are non-linear, so when their energies are shifted from the central value of k_{JES}, the weight distribution will disperse and give a more spreaded likelihood distribution.

Table 8.1: Four different k_{JES} values from the central value of k_{JES} = 1.025 are probed. The k_{JES} vs. uncalibrated m_t from data measurement and the corresponding minimum of $-\log\mathcal{L}$ are shown in the table for the ee, $e\mu$, $\mu\mu$ and combined channels. The m_t and the minimum of $-\log\mathcal{L}$ are separated by comma.

k_{JES}	0.975	1.000	1.025	1.050	1.075
ee	179.9, -44.8	176.6, -43.1	174.6, -39.6	172.7, -37.8	169.5, -37.1
$e\mu$	176.8, 115.1	174.6, 109.4	172.4, 108.6	169.8, 118.4	167.4, 122.4
$\mu\mu$	185.0, 15.7	181.8, 18.1	179.2, 20.6	177.7, 14.9	175.2, 19.7
combined	178.5, 88.0	176.2, 85.3	173.9, 91.1	171.7, 97.7	169.2, 106.8

A cross check is performed by looking at the distribution of jet p_T and $\not\!\!E_{\rm T}$ before and after applying k_{JES} to data. Fig. 8.2 and 8.3 shows the leading jet p_T distribution for each individual dilepton channel and the combined channel, before and after k_{JES} correction, respectively. The KolmogorovCSmirnov (KS) test clearly indicates that the data-MC agreement is improved after applying k_{JES} to the dilepton data events.

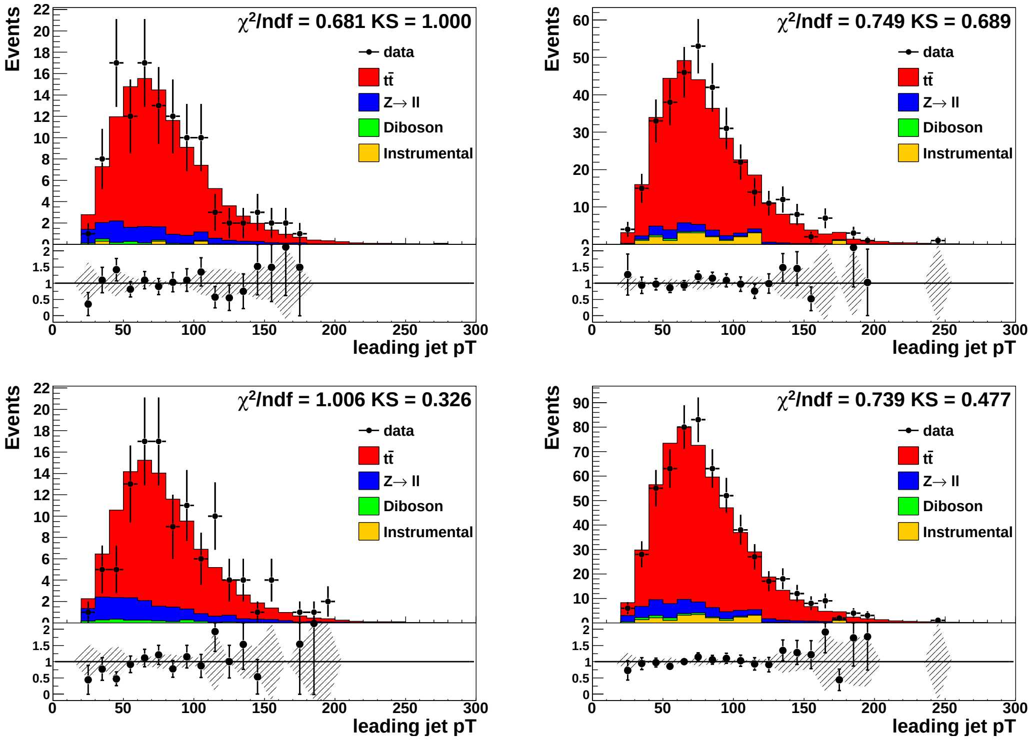

Figure 8.2. Distribution in the p_T of the leading jet for the ee (top left), $e\mu$ (top right), $\mu\mu$ (bottom left) and combined (bottom right) channels before applying k_{JES} to data.

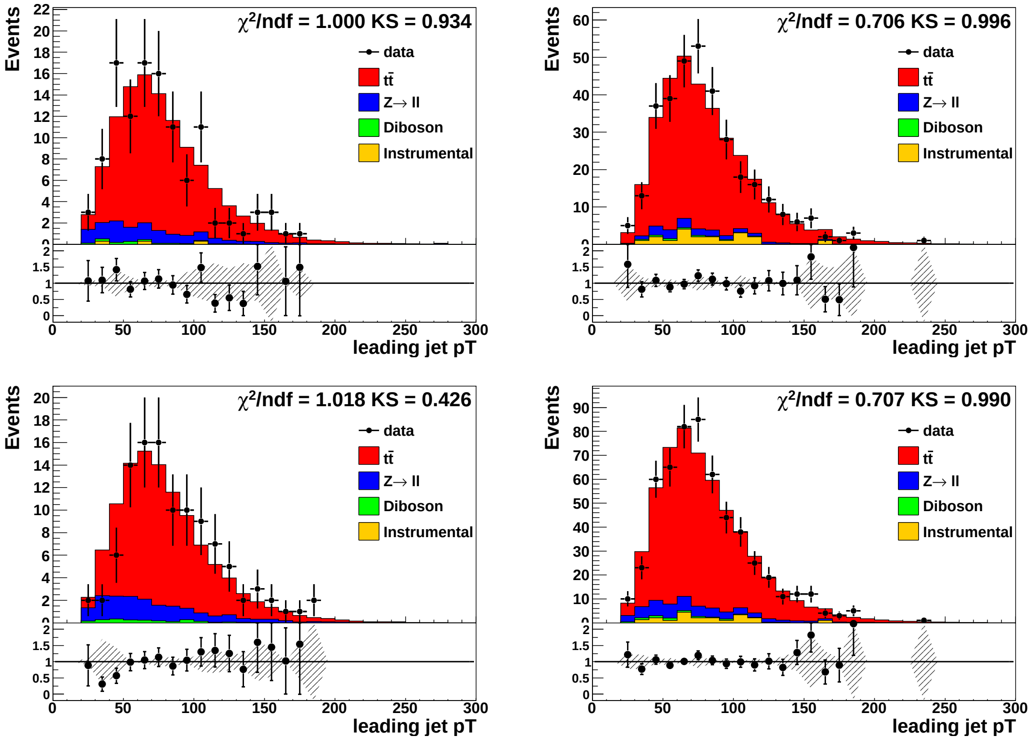

Figure 8.3. Distribution in the p_T of the leading jet for the ee (top left), $e\mu$ (top right), $\mu\mu$ (bottom left) and combined (bottom right) channels after applying k_{JES} to data.

8.3. Systematic Uncertainties

The systematic uncertainties in the dilepton top quark mass measurement can be classified into four groups:

- jet energy scale,
- modeling of signal events,
- simulation of detector response, and
- other uncertainties associated with procedures used in the analysis.

For hadron collider physics, the jet energy determination is a complicated and significant procedure so the JES associated uncertainties are specifically grouped into one category, a) JES: including effects from the statistical uncertainty of the JES, residual effects from p_T and η dependence of the standard JES, and flavor dependence of jet response; b) Signal modeling: The signal modeling uncertainties include effects from color reconnection in the string fragmentation model, additional jets from ISR/FSR, next-to-leading order (NLO) correction, modeling of the hadronization procedure, modeling of b quark fragmentation, and uncertainties of the parton distribution functions; c) Object reconstruction and identification: there are uncertainties on the identificaiton efficiency and energy resolution of jets, as well as the energy scale and resolution of leptons; d) Method: This category consists of systematic uncertainties from the template method itself, including the uncertainties in the calibration, limited MC statistics in the construction of templates, and the fraction of signal events.

8.3.1. Determination of Systematic Uncertainties

The estimation of systematic uncertainties utilizes the background samples and the default $t\bar{t}$ signal sample with $m_{\mathrm{t}}^{\mathrm{MC}} = 172.5$ GeV. Only a few modeling related systematic uncertainties require new $t\bar{t}$ MC samples but with the same $m_{\mathrm{t}}^{\mathrm{MC}} = 172.5$ GeV.

The exact estimation method of systematic uncertainties is described in Ref. [93], which is used by both the DØ and CDF experiments. There are three different modes based on the relationship between m_t^-, m_t^0 and m_t^+, where m_t^0 is the estimated top quark mass corresponding to the central value of a certain parameter when using the nominal MC signal sample, and m_t^+/m_t^- are the ones corresponding to one sigma up/down variation of that parameter. The three modes are calculated as follows:

- if $m_t^- < m_t^0 < m_t^+$ or $m_t^+ < m_t^0 < m_t^-$, then $\delta m_t = |m_t^+ - m_t^-|/2$
- if $\mathrm{sign}(m_t^+ - m_t^0) = \mathrm{sign}(m_t^- - m_t^0)$, then $\delta m_t = \max(|m_t^+ - m_t^0|/2, |m_t^- - m_t^0|/2)$
- if m_t^- or m_t^+ does not exist, $\delta m_t = m_t^+ - m_t^0$ or $\delta m_t = m_t^- - m_t^0$

where δm_t is the estimated systematic uncertainty. Individual systematic uncertainties are described in the following sections, with corresponding values given for the combination at the end of each section.

8.3.2. Jet Energy Scale

8.3.2.1. Uncertainty due to lepton+jets JES

In the dilepton channel, the b jet energies are calibrated by the ℓ+jets JES. Therefore the statistical uncertainty of the factor k_{JES} can cause a systematic shift in the estimated top quark mass in the dilepton channel. In 9.7 fb^{-1}, the ℓ+jets analysis yields a JES factor $k_{JES} = 1.0250 \pm 0.0046$ (stat.) [81]. This is obtained from the increased amount of data and updated standard JES for the full DØ Run II datasets, which more effectively treats aging and time-dependent calorimeter corrections. We also omit the double ratio (see Eq. 5.24) systematic effect. It is unnecessary now since the current DØ JES incorporated flavor-dependent effects. Instead of using the general JES uncertainty, the dilepton JES uncertainty is estimated from the statistical uncertainty of the ℓ+jets JES factor through varying the factor k_{JES} up and down by 1 σ, and symmetrizing the difference of the estimated m_{t}. We found the JES uncertainty in the dilepton channel to be 0.47 GeV. This JES uncertainty was the largest source of systematic uncertainties in previous analysis, and now has been reduced down to the same scale as other systematics like the physics modeling ones.

8.3.2.2. Residual jet energy scale

The residual JES uncertainty arises from the fact that the Jet Energy Scale (JES) depends on jet p_T and η. When adopting the JES from the ℓ+jets measurement, we assumed a globally fixed JES. To account for the p_T and η dependence, the fractional uncertainties associated with the default JES corrections are first plotted for the jets in our $t\bar{t} \to ee$ sample at $m_t = 172.5$ GeV after all selections. We use the ee sample since the muon fake rate is much lower in this channel and therefore can provide a more accurate knowledge of $\not\!\!E_T$. The average corrections per bin are then plotted versus E_{jet} and fitted with the standard DØ parameterization [71] [75]:

$$\frac{\sigma}{JES} = p_1 + p_2 E_{jet} + p_3 \mathrm{exp}(-E_{jet}/p_4) \tag{8.1}$$

for 4 η regions: (0-0.5), (0.5-1.0), (1.0-1.5), (1.5-) (see Fig. 8.4). Subsequently, this parametrization is applied to scale up and down jet energies as a function of E_{jet} in all the channels:

$$1 \pm ((\frac{\sigma}{JES})_b^{dilepton} - < \frac{\sigma}{JES} >_{light}^{\ell+jets}) \tag{8.2}$$

where $< \frac{\sigma}{JES} >_{light}^{\ell+jets}$ is the average fractional JES uncertainty light quark jets in the ℓ+jets channel, which I calculated to be 0.0200. This single constant offset is subtracted from this parameterization across all four η regions to take into account the p_T spectrum differences between light quark jets and b jets. The residual uncertainty was evaluated by shifting the standard DØ JES up and down and comparing them to the central values of m_t. As shown in Table 8.2, the up/down variations are symmetric in the $e\mu$ channel while they are different in the ee channel by 0.09 GeV and about 0.05 GeV in the $\mu\mu$ channel. This could be due to the larger ratio of background events in the ee and $\mu\mu$ events, where the down variation will cause signal events to be background-like with a lower m_t. Since the background template is also spiky, it results in bias in the estimated value of m_t. Therefore, we decided to take both the up and down varations instead of taking the average value to prevent overestimating the deviation in down variation case. The estimated symmetrized residual JES uncertainty is $^{+0.35}_{-0.36}$ GeV.

As a cross check, the difference in b jet and light quark jet p_T spectrum can be estimated by using a shifted k_{JES} instead of the constant offset from light quark jet. The up shifted k_{JES}, denoted by k_{JES}^{up}, is determined in the $l + jets$ channel when all jet energies are shifted up by 1 σ of standard JES uncertainty. It is applied to the b jets in the dilepton channel to correct for the corresponding up variation of jet energies. Since we apply k_{JES} to the data instead of MC samples, to compare to the central value of m_t, the above scaling of jet energy is further divided by the k_{JES}. The down variation was not estimated in the ℓ+jets channel as it was found to be symmetric with the up variation in that channel analysis. As shown in Table 8.2, the up variation is in good agreement with the cross check. This is also a cross check that the standard JES and k_{JES} are consistent. We do not take the values from the cross check as residual uncertainty since we found the up/down variations are asymmetric in dilepton channel for the template method. More importantly, using an offset is a more direct interpretation than using a shifted k_{JES}, which involves all the machinery of the ℓ+jets Matrix-element analysis.

Table 8.2: Residual systematic uncertainty (GeV) from the up variation (first column), down variation (second column) and cross check with up variation (third column) for the ee, $e\mu$, $\mu\mu$ and combined analysis. The cross check is in good agreement with the up varation.

channel	up variation	down variation	up variation cross check
ee	+0.321	-0.410	+0.334
$e\mu$	+0.367	-0.342	+0.352
$\mu\mu$	+0.328	-0.373	+0.303
combined	+0.346	-0.359	+0.338

8.3.2.3. Flavor dependent uncertainty

The flavor dependent correction is based on single particle responses that are applied to all MC samples to improve agreements between data and MC. In the current analysis, the single particle response has been integrated into general JES package and corrections are applied jet-by-jet based on particle content. This minimizes the inaccuracy from considering only the "bulk" flavor of a jet and also reduces the difference between MC b jets and data b jets. The flavor dependent uncertainty arises from the uncertainties on single particle response. Therefore we estimate this systematic uncertainty by shifting the single particle responses up and down by 1 σ of their

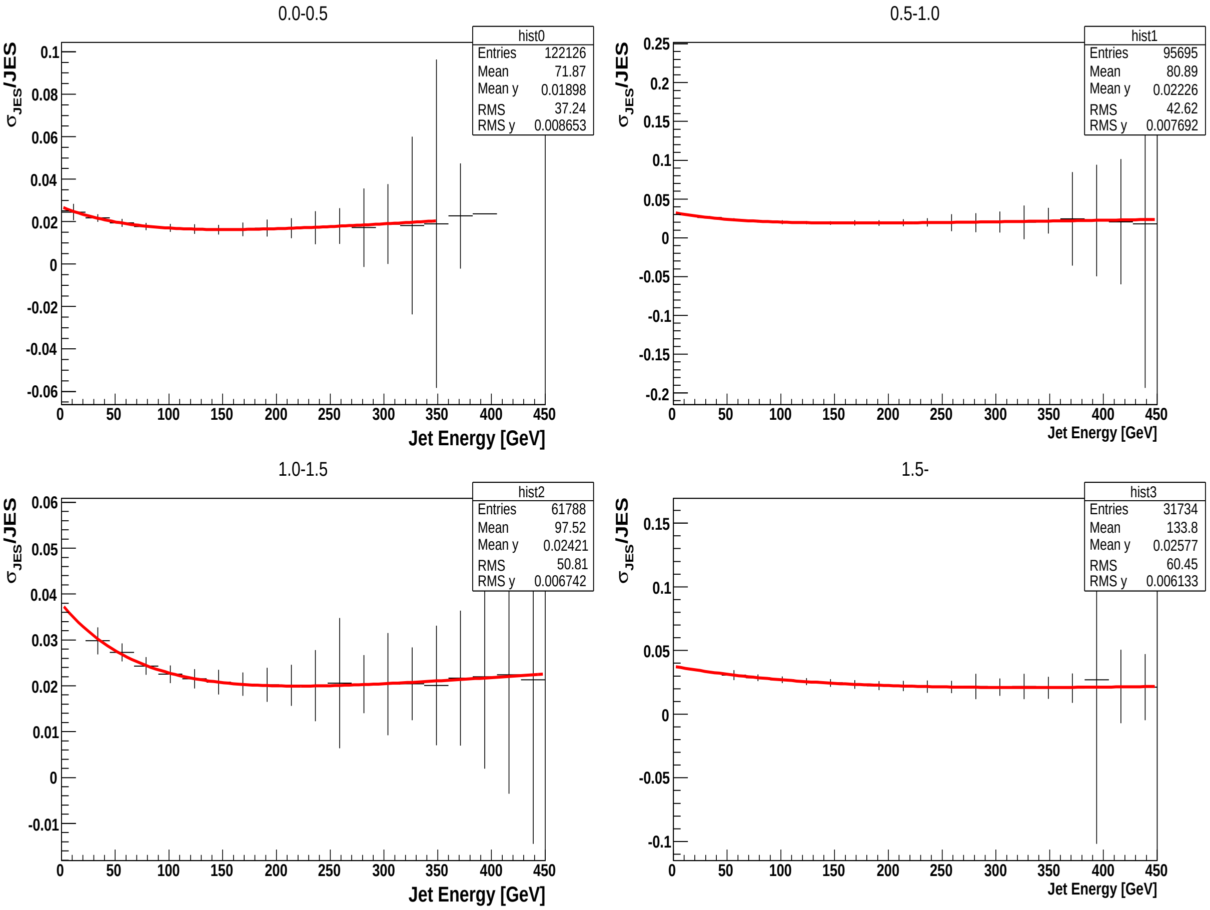

Figure 8.4. Fitted fractional JES as a function of jet energy in 4 η regions.

uncertainty and apply them to the light quark jets and b jets in the MC samples. The estimated uncertainty is 0.27 GeV.

8.3.3. Physics Modeling

8.3.3.1. ISR/FSR

The modeling of the initial and final state radiation can have a systematic impact on the measurement due to extra jets in the events [94]. We evaluate this systematic uncertainty by using ALPGEN + PYTHIA samples that are analogous to the default $t\bar{t}$ sample with $m_{\mathrm{t}}^{\mathrm{MC}} = 172.5$ GeV. The renormalization scale parameter for the CKKM matching scheme in ALPGEN interfaced to PYTHIA is varied up and down by 1.5 from its default value $\mu = \sqrt{\sum((2m_t)^2 + p_T^2)}$ to decrease and increase ISR/FSR. The systematic uncertainty due to ISR/FSR is found to be 0.15 GeV.

8.3.3.2. Color reconnection

In strong interactions, the color reconnection (CR) represents the processes induced by the high density of color charges, which may lead to a nontrivial nonlinear manner of interactions. The default DØ PYTHIA tune does not explicitly include CR, while the top quark mass is found to have a potentially nonnegligible sensitivity to the specific modeling of CR [95]. To evaluate the effects from CR, two different tunes on the ALPGEN +PYTHIA samples with $m_{\mathrm{t}}^{\mathrm{MC}} = 172.5$ GeV are generated, Perugia 2011 and Perugia 2011NOCR [96]. The Perugia 2011 tune has an explicit modeling of CR while the Perugia 2011NOCR tune does not. The CR modeling in Perugia is more explicit and more phenomenologically motivated. For example, the color string survival probability is modeled to be dependent on the distance in rapidity between the beginning and the end of the color string in Perugia. Moreover, Perugia 2011 and Perugia 2011NOCR PYTHIA tunes are 100% correlated since the exact same events are used to reduce statistical effects. The uncertainty due to CR is obtained by comparing the estimated top quark mass from the two different tunes, which is estimated to be +0.22 GeV.

8.3.3.3. Higher order effects

The ALPGEN generator is a LO generator with higher powers of α_S. It does not account for NLO effects in the initial states of gg fusion, or in the extra radiation from hard jets. To evaluate these effects, samples with full NLO calculations are generated with MC@NLO [97] [98] [99]. Since MC@NLO can only be interfaced with HERWIG, ALPGEN is equivalently combined with HERWIG to avoid double-counting effects from different models of parton showering in HERWIG and PYTHIA of our standard samples. Both samples are generated with an $m_{\mathrm{t}}^{\mathrm{MC}} = 172.5$ GeV. The estimated m_t in MC@NLO + HERWIG is found to be 0.33 GeV higher than in ALPGEN + HERWIG, which is quoted as the uncertainty due to higher order effects. The sign of this systematic uncertainty is not kept since it reflects the actual effects from a more precise NLO calculations.

8.3.3.4. Hadronization

The choice of a specific hadronization model may cause bias in the measured m_t. To evaluate this effect, we use two sets of events that are similarly generated by the ALPGEN generator but differently hadronized by HERWIG and PYTHIA. Note that the JES calibration is obtained for the default PYTHIA tune, which can be different for HERWIG. The ℓ+jets analysis has checked that this difference between fitted k_{JES} in the two models is very small at particle level, thus the potential effect of different JES is factorized out. In dilepton channel, we found that the HERWIG hadronization is systematically lower than PYTHIA by 0.11 GeV.

8.3.3.5. b quark fragmentation

The modeling of b-quark fragmentation can bring a systematic uncertainty to the measured m_t. To estimate this uncertainty, the default PYTHIA b-fragmentation function is replaced with the Bowler fragmentation function [100]. Then the default MC samples are reweighted with this function input parameters tuned to SLD data, and to LEP data [101]. The largest difference in estimated m_t between these two reweightings and the default $t\bar{t}$ sample is quoted as the b-fragmentation systematic uncertainty, which is -0.10 GeV in the combination.

8.3.3.6. Uncertainties in PDF

To estimate the systematic uncertainty due to uncertainties of parton distribution functions (PDFs), the ALPGEN + PYTHIA $t\bar{t}$ sample with $m_t = 172.5$ GeV is reweighted by shifting each of the 20 PDFs from CTEQ6M [102] 1 σ up and down. The overall systematic uncertainty can be calculated with the following equation as described in Ref. [93]:

$$\delta m_t = \frac{1}{2}\left(\sum_{i=1}^{N_p}(m_t(S_i^+) - m_t(S_i^-))^2\right)^{1/2} \tag{8.3}$$

where i runs over the set of PDFs, N_p is the total number of PDFs ($N_p = 20$), $m_t(S_i^+)$ and $m_t(S_i^-)$ are the measured top quark masses for the positive and the negative excursion by one standard deviation respectively of the i-th PDF. This uncertainty is found to be 0.08 GeV.

8.3.4. Object Reconstruction & Identification

8.3.4.1. Electron energy scale and muon momentum scale

The electron energy scale and muon energy scale measured in MC do not match exactly to the value in data. For electrons, an energy scale is applied to correct for their interaction with detector materials which is better described in data. For muons, differences are found in the $Z \to \mu^+\mu^-$ MC sample compared to the data. Thus, a scaling function is applied to correct the muon p_T. We evaluate the systematic effects of these changes in scale by varying them up and down separately for electrons and muons, and found an overall 0.01 GeV value for the electrons and muons.

8.3.4.2. Electron energy and muon p_T resolution

The energy resolution of electrons and the p_T resolution of muons in MC do not match perfectly with data. This is corrected by applying additional smearing to the MC samples [103]. The smearing corrections have uncertainties that can be used for up and down variation. The varied smearings compared to the default ones yield an overall systematic uncertainty of 0.03 GeV for electron and muons.

8.3.4.3. Jet energy resolution

Similarly to the lepton p_T resolution, the jet energy resolution in MC does not agree exactly with data as well due to several reasons, for instance, mismodeling of the detecor, or approximations made in the showering and hadronization model in PYTHIA. A correction based on γ+jets events known as JSSR (jet smearing, shifting and removing) [104], is applied to account for these effects. The parameters in this correction are shifted by 1 σ up and down to evaluate the systematic uncertainty. The ensemble testing shows that this systematic uncertainty is 0.12 GeV.

8.3.4.4. Jet identification efficiency

The jet multiplicity in data is slightly different from MC, which causes a small difference in reconstruction efficiencies between data and MC. To estimate the systematic uncertainty from this effect, the jet identification efficiency is decreased by 1 σ with respect to its uncertainty. By comparing the estimated m_t with the default nominal value from $t\bar{t}$ sample with $m_{\mathrm{t}}^{\mathrm{MC}} = 172.5$ GeV, we obtain a value of -0.03 GeV as the systematic uncertainty.

8.3.5. Method

8.3.5.1. Calibration uncertainty

As shown in Table 7.16, the fitting parameters in the calibration Equation. 6.12 have nonnegligible statistical uncertainties due to limited statistics of $t\bar{t}$ MC events at each mass point. Typically, the offset has an uncertainty that is 10 times larger than the slope uncertainty, therefore it dominates the uncertainty from calibration. Through the propagation of uncertainties, the systematic uncertainty due to calibration can be expressed as the following:

$$\delta m_t^{calib,meas} = \sqrt{\left(\frac{\partial m_t^{calib,meas}}{\partial\alpha}\right)^2 \delta\alpha^2 + \left(\frac{\partial m_t^{calib,meas}}{\partial\beta}\right)^2 \delta\beta^2} \tag{8.4}$$

where $\delta\alpha$ and $\delta\beta$ are the uncertainties of slope α and offset β. Plugging in Equation. 6.12 and resolving the derivatives, the uncertainty can be finally written as:

$$\delta m_t^{calib,meas} = \frac{1}{\alpha}\sqrt{(m_t^{meas} - \beta - 170)^2\delta\alpha^2 + \alpha^2\delta\beta^2} \tag{8.5}$$

Through error propagation, we get an uncertainty of 0.07 GeV.

8.3.5.2. Template Statistics

As an analysis based on a template method, the sensitivity of the estimated top quark mass, m_t, depends on the shape of the templates. In templates, each bin value is determined within some uncertainties. The limited statistics of simulated MC events can cause shifts in the template bin values, and therefore may result in an overall shift of the template shape, and hence the estimated m_t. The evaluation of this systematic uncertainty uses data events. We constructed 1000 new templates for both signal and background varying their bins within their gaussian uncertainties, and used these new templates to obtain 1000 new measurements on data. The RMS of these 1000 measurements is quoted as a systematic uncertainty, which is found to be 0.18 GeV.

8.3.5.3. Signal fraction

The expected signal and background event yields are determined with statistical uncertainties due to limited MC statistics (see Table 6.2). Since the relative uncertainty of signal yields is much smaller than background, the actual signal fraction is subject to the background uncertainty. To estimate the systematic effect of the statistical uncertainty on the background event yield, we varied the mean yield of all background processes up and down by their statistical error as shown in Table 6.2. The uncertainty is calculated to be 0.01 GeV.

The systematic uncertainties for each individual channel, and for the combined analysis are listed in Table 8.3.

Table 8.3: Summary of uncertainties for the measurement of m_{t} in dilepton final states using 9.7 fb^{-1} of data. The 9.7 fb^{-1} combination uses fitting method. The BLUE method is used for the combination with ℓ+track.

Source	Uncertainty (GeV)					
	9.7 fb^{-1}				1 fb^{-1}	Combination
	ee	$e\mu$	$\mu\mu$	2ℓ	ℓ+track	
Jet Energy Scale:						
JES	±0.47	±0.47	±0.50	±0.47	±1.41	±0.46
Flavor dependent	±0.28	±0.26	±0.31	±0.27	±0.17	±0.26
Residual uncertainty	$^{+0.32}_{-0.41}$	$^{+0.37}_{-0.34}$	$^{+0.33}_{-0.37}$	$^{+0.35}_{-0.36}$	-	$^{+0.34}_{-0.35}$
Physics Modeling:						
Color reconnection	+0.21	+0.21	+0.35	+0.22	±0.25	$^{+0.22}_{-0.01}$
ISR/FSR	±0.09	±0.22	±0.03	±0.15	±0.15	±0.15
Higher order effects	+0.45	+0.02	+1.38	+0.33	±1.24	$^{+0.35}_{-0.04}$
Hadronization	±0.25	±0.33	±0.25	±0.11	±0.11	±0.11
b quark fragmentation	±0.17	±0.11	±0.31	±0.10	±0.17	±0.10
PDF uncertainty	±0.20	±0.14	±0.12	±0.08	±0.33	±0.09
Object Reconstruction & Identification:						
Electron energy scale	±0.02	±0.03	-	±0.00	±0.00	±0.00
Electron energy resolution	±0.04	±0.01	-	±0.00	±0.17	±0.00
Muon p_T scale	-	±0.01	±0.00	±0.01	±0.01	±0.01
Muon p_T resolution	-	±0.03	±0.00	±0.03	±0.08	±0.03
Jet resolution	±0.14	±0.14	±0.01	±0.12	±0.25	±0.12
Jet identification	−0.02	−0.03	−0.06	−0.03	±0.50	$^{+0.01}_{-0.04}$
Method:						
Calibration uncertainty	±0.04	±0.07	±0.13	±0.07	±0.33	±0.07
Template statistics	±0.41	±0.20	±0.57	±0.18	±0.50	±0.18
Signal fraction	±0.12	±0.01	±0.02	±0.01	±0.08	±0.01
Total systematic uncertainty	$^{+1.00}_{-0.90}$	$^{+0.85}_{-0.81}$	$^{+1.69}_{-1.03}$	$^{+0.82}_{-0.72}$	±2.12	$^{+0.83}_{-0.72}$
Statistical uncertainty	±3.04	±1.71	±3.56	±1.36	±8.40	±1.34
Total uncertainty	$^{+3.20}_{-3.17}$	$^{+1.91}_{-1.89}$	$^{+3.94}_{-3.71}$	$^{+1.59}_{-1.54}$	±8.66	$^{+1.58}_{-1.52}$

8.3.6. Statistical Components of Systematic Uncertainties

An estimation to the statistical uncertainty of systematic uncertainty has been derived by splitting MC samples into 5 equivalent subsets. Each subset provides an independent estimation of systematic uncertainties. We calculate the RMS of the 5 measurements for each systematic uncertainty and then divide them by $\sqrt{4}$ to correct for the reduced sample size. This RMS is our estimation of the statistical uncertainties of systematic uncertainties. A list is provided in Table 8.4 for most of the systematic uncertainties.

On average the systematics estimated from tuning parameters have a statistical uncertainty of 0.05 GeV. Other systematics which compare two differently generated samples have about 2 times bigger statistical uncertainties since they are usually not symmetrized.

The NLO effect in the $\mu\mu$ channel is unexpectedly much bigger than the other two channels. We looked into the statistical uncertainty of the NLO systematic as shown in Table 8.4. It shows that the large effect is unlikely to be caused by statistical fluctuations. The reason for the large NLO uncertainty in $\mu\mu$ could be misconfiguration in event generation or object reconstruction. So I investigated the kinematic variables of the NLO samples. We use MC@NLO + HERWIG sample for the estimation of NLO effects. In the comparison of kinematics between ALPGEN + PYTHIA and MC@NLO + HERWIG, for example, we see that the $\mu\mu$ jet p_T (see Fig. 8.5) agrees well among all the three channels. There is no obvious sign of a difference between the $\mu\mu$ channel and the other two channels. Event selection differences since the overall $\not{E}_T$ cut is only applied in this channel. A partial $\not{E}_T$ cut in the Z boson mass window is applied in the ee channel, and there is a lower NLO systematic uncertainty. In the $e\mu$ channel, the $\not{E}_T$ cut is absent, and the NLO systematic uncertainty is found to be almost zero. These indicate that the NLO systematic uncertainty is very likely to be $\not\!\!E_T$ cut sensitive. Since the $\mu\mu$ channel has the least contribution to the combined results, the effect from this large uncertainty is very limited in the combination.

Table 8.4: Estimated statistical uncertainty of most systematics for all dilepton channels using 5 independent subsamples. Unit is in GeV.

Syst[GeV]./Ch	ee	$e\mu$	$\mu\mu$
Jet identification	0.067	0.121	0.088
Jet resolution	0.057	0.069	0.087
Electron energy resolution	0.046	0.051	-
Electron energy scale	0.076	0.040	-
Muon p_T resolution	-	0.055	0.126
Muon p_T scale	-	0.048	0.113
Flavor dependent	0.089	0.042	0.075
b quark fragmentation	0.108	0.125	0.228
ISR/FSR	0.057	0.059	0.061
Higher order effects	0.097	0.080	0.107
Color reconnection	0.098	0.091	0.127

8.3.7. Combination

As shown in Eq. 6.9 and 6.10, for the combination of all the dilepton measurements, we fit the combined likelihood calculated from each individual channel to a parabola. The (blinded) results from each channel are the following:

$$m_{\mathrm{t}}^{ee} = 173.99 \pm 3.04 \text{ (stat)}^{+1.00}_{-0.90} \text{ (syst) GeV.}$$

$$m_{\mathrm{t}}^{e\mu} = 171.86 \pm 1.71 \text{ (stat)}^{+0.85}_{-0.81} \text{ (syst) GeV.}$$

$$m_{\mathrm{t}}^{\mu\mu} = 178.58 \pm 3.56 \text{ (stat)}^{+1.69}_{-1.03} \text{ (syst) GeV.}$$

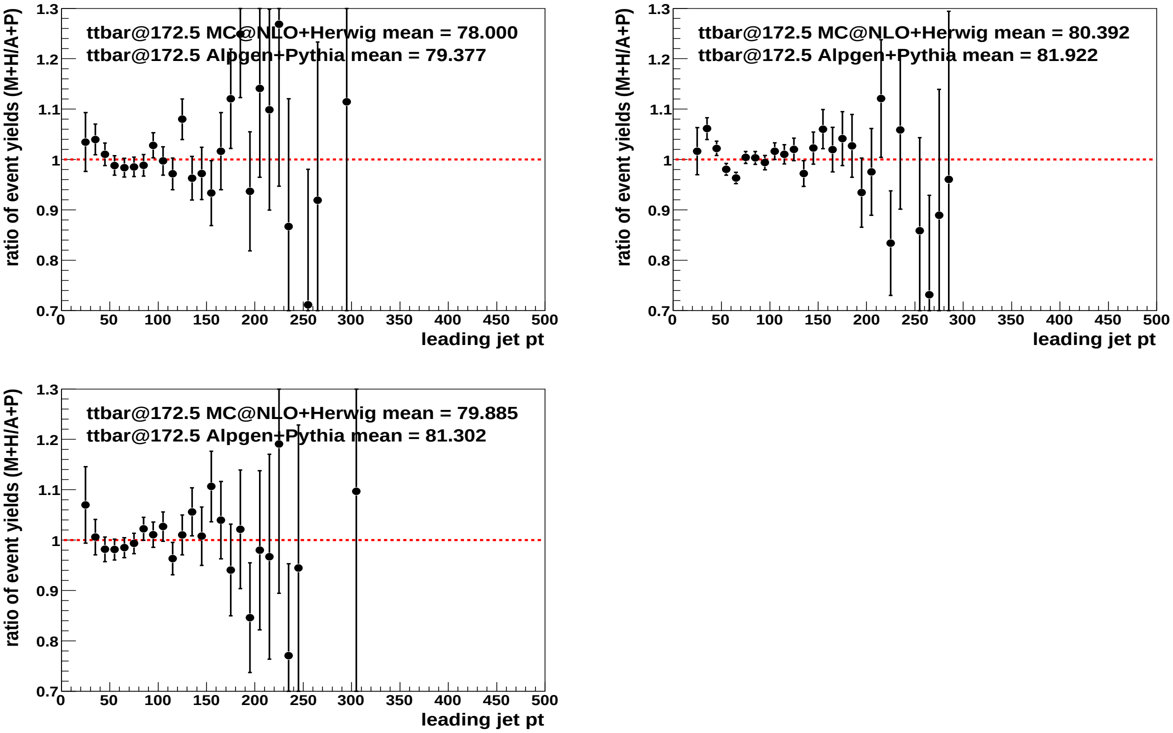

Figure 8.5. Ratio of (MC@NLO+HERWIG)/(ALPGEN+PYTHIA) with $m_{\rm t}^{\rm MC}$=172.5 GeV vs. leading jet pt for the ee, $e\mu$ and $\mu\mu$ channels.

And the combined result is:

$$m_{\rm t}^{\rm combined} = 173.32 \pm 1.36\ ({\rm stat})^{+0.82}_{-0.72}\ ({\rm syst})\ {\rm GeV}.$$

8.3.7.1. Combination with 1 fb^{-1} lepton+track measurement

A measurement of m_t was previously performed in 1 fb^{-1} of DØ data with 14 lepton+track events (ℓ+track), which have one identified lepton (e or μ), one isolated track and at least one b-tagged jet [89]. This measurement employed both neutrino weighting and matrix weighting techniques. To combine with the ℓ+track measurement, we use the BLUE (Best Linear Unbiased Estimator) [105] [106] method.

In the 1 fb^{-1} analysis, the ℓ+track selections were made to be orthogonal to the contemporary dilepton event selections through vetoing dilepton events. Since electron identification has been changed and muon/track identification are also slightly updated for the 1 fb^{-1} of data, I needed to check the orthogonality for the 9.7 fb^{-1} dilepton event selections.

- The electron likelihood requirement for tight electron selection is replaced with Boosted Decision Trees (BDT), where the likelihood becomes a variable of BDT. This may affect the orthogonility between the ee and $e\mu$ channels and the ℓ+track channel.
- The muon identification is tighter in the ℓ+track channel due to global muon fitting and tighter DCA and isolation requirements.
- In addition, the ℓ+track channel requires leading jet $p_T > 40$ GeV and a cut on the $\not{E}_T$ in the Z boson mass window.

After making these ℓ+track selections on top of the 9.7 fb^{-1} of dilepton events after all selections, we found 0.81 $t\bar{t}$ event and 1 data event in the ee channel, 0.73 $t\bar{t}$ event and 1 data event in the $e\mu$ channel, as well as 0.02 $t\bar{t}$ event and 0 data event in the $\mu\mu$ channel (see Table 8.5). It shows that at most 1.56 dilepton $t\bar{t}$ events may get selected into 14.0 ℓ+track $t\bar{t}$ events. Also, the dilepton b tagging efficiency is 87.6% while the ℓ+track b tagging efficiency is about 50%, conservatively the chance of ℓ+track events passing through the b tagging requirement is 50%/87.6% $\approx$ 57%. Therefore, the maximum estimation of dilepton and ℓ+track correlation is about 6%. Furthermore, in the 1 fb^{-1} ℓ+track analysis, the correlation between the neutrino weighting method and matrix weighting method is 61%, and the latter contribute a lot more to the combination. Therefore, the dilepton and ℓ+track channels are $< 5\%$ correlated and we assume zero correlation for their combination.

Table 8.5: Number of $t\bar{t}$ and data events that pass the tighter ℓ+track selections in the ee, $e\mu$ and $\mu\mu$ channels.

channel	$t\bar{t}$	data
ee	0.81	1
$e\mu$	0.73	1
$\mu\mu$	0.02	1
total	1.56	3

All JES related systematic uncertainties and method related systematic uncertainties are considered to be uncorrelated, others are considered 100% correlated. Some uncertainties in the 9.7 fb^{-1} of measurement are not available in the ℓ+track channel, including ISR/FSR, hadronization and lepton energy/p_T scale. We use the 9.7 fb^{-1} values for the missing entries in the ℓ+track measurement.

In Ref. [89], the reported systematic uncertainties are not broken down. The individual systematic uncertainties are only available for neutrino weighting method in Ref. [89] with a total systematic uncertainty of 2.7 GeV. Therefore, I normalized the neutrino weighting systematic uncertainties to the combination of neutrino weighting and matrix weighting methods, which has a total systematic uncertainty of 2.4 GeV.

Combining the 9.7 fb^{-1} of dilepton measurement and 1 fb^{-1} ℓ+track measurement, we get blineded measurement:

$$m_{\mathrm{t}} = 173.11 \pm 1.34\ (\mathrm{stat})^{+0.83}_{-0.72}\ (\mathrm{syst})\ \mathrm{GeV}.$$

Chapter 9

CONCLUSION

In proton-antiproton collision data corresponding to an integrated luminosity of 9.7 fb^1, I used the neutrino weighting method to extract a top quark mass estimate from $t\bar{t}$ events in the dilepton final states. The results for each channel are the following:

$$m_{\mathrm{t}}^{ee} = 173.99 \pm 3.04 \text{ (stat)}^{+1.00}_{-0.90} \text{ (syst) GeV.}$$
$$m_{\mathrm{t}}^{e\mu} = 171.86 \pm 1.71 \text{ (stat)}^{+0.85}_{-0.81} \text{ (syst) GeV.}$$
$$m_{\mathrm{t}}^{\mu\mu} = 178.58 \pm 3.56 \text{ (stat)}^{+1.69}_{-1.03} \text{ (syst) GeV.}$$

For the combination of all three channels, I fit the combined likelihood of all dilepton channels. The result is :

$$m_{\mathrm{t}} = 173.32 \pm 1.36 \text{ (stat)}^{+0.82}_{-0.72} \text{ (syst) GeV.}$$

By combining with our previous 1 fb^{-1} of measurement in the ℓ+track channel using the BLUE method, the final result is:

$$m_{\mathrm{t}} = 173.11 \pm 1.34 \text{ (stat)}^{+0.83}_{-0.72} \text{ (syst) GeV.}$$

As shown in Fig. 9.1, our result is consistent very well with the first official world combination of the top quark mass [107]. The systematic uncertainty of our measurement is the smallest among all the dilepton top quark mass analyses to date. The statistics are now the primary restriction that limit the precision of this measurement.

Nevertheless, the precision has been reduced to 0.9%, which is better than the CDF and ATLAS results in Fig. 9.1 and very competitive to the CMS result despite much less statistics. The indirect measurement of the top Yukawa coupling y_t from our dilepton measurement is 0.9952 ± 0.0090, which is consistent with unity very well.

As legacy measurement of DØ experiment, this analysis will improve the precision of the Tevatron combination of the top quark mass together with the ℓ+jets measurement [81]. The world combination is not trivial and requires a lot more efforts, but if it is possible to be updated, the most precise top quark mass will be defined and push the precision of the SM tests. Moreover, the concept of the kinematic reconstruction can be further used in ttH analyses since top events are major backgrounds. The idea of top-as-a-calibration-tool can also be generalized and becomes a standard for jet energy calibration in different event topologies.

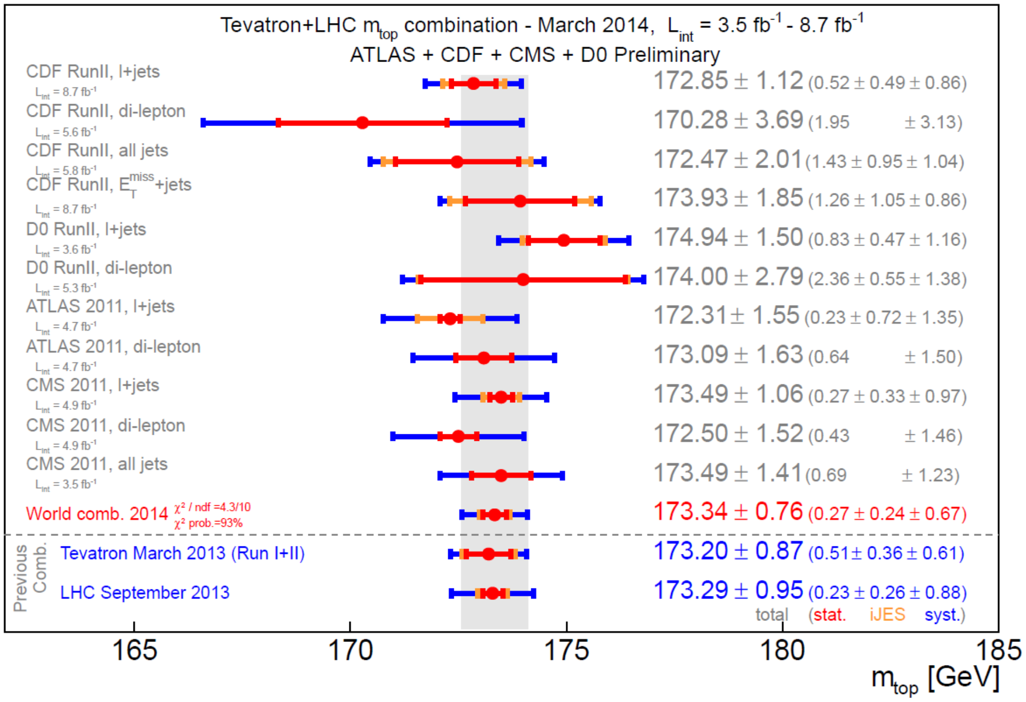

Figure 9.1. The first official world average of the top quark mass using measurements from DØ, CDF, ATLAS and CMS.

Appendix A

Quadratic Solutions in Neutrino Weighting Method

In dilepton final states, the system of equations for each decay of the top/antitop quark is independent. Therefore, for each top/antitop decay, the system can be written as follows:

$$M_W^2 = (E_\ell + E_\nu)^2 - (\vec{p}_\ell + \vec{p}_\nu)^2, \tag{A.1}$$

$$M_t^2 = (E_\ell + E_\nu + E_b)^2 - (\vec{p}_\ell + \vec{p}_\nu + \vec{p}_b)^2, \tag{A.2}$$

where M_W is the invariant mass of the W boson; $(E_\ell,\, \vec{p}_\ell)$, $(E_\nu,\, \vec{p}_\nu)$, and $(E_b, \vec{p}_b)$ are the components of the Lorentz four-vector of lepton and neutrino from the W boson decay, and the b quark from the top decay, respectively. For given top quark mass m_t and known b quark mass m_b, ignoring negligible lepton mass, Eq. A.1 and A.2 can be deduced to be:

$$C_\ell = \frac{M_W^2}{2} = E_\ell E_\nu - \vec{p}_\ell \cdot \vec{p}_\nu, and \tag{A.3}$$

$$\begin{aligned} C_b &= \frac{m_t^2 - M_W^2 - m_b^2 - 2(E_\ell E_b - \vec{p}_\ell \cdot \vec{p}_b)}{2} \\ &= E_b E_\nu - \vec{p}_b \cdot \vec{p}_\nu. \end{aligned} \tag{A.4}$$

Expanding neutrino momenta in spherical coordinates $(E_\nu,\, \theta_\nu,\, \phi_\nu)$, we have

$$\begin{aligned} C_\ell = E_\ell E_\nu &- p_{\ell x} E_\nu \sin\theta_\nu \cos\phi_\nu \\ &- p_{\ell y} E_\nu \sin\theta_\nu \sin\phi_\nu \\ &- p_{\ell z} E_\nu \cos\theta_\nu, and \end{aligned} \tag{A.5}$$

$$\begin{aligned} C_b = E_b E_\nu &- p_{bx} E_\nu \sin\theta_\nu \cos\phi_\nu \\ &- p_{by} E_\nu \sin\theta_\nu \sin\phi_\nu \\ &- p_{bz} E_\nu \cos\theta_\nu . \end{aligned} \tag{A.6}$$

Denoting $\beta_i = p_i/E$, and define $C = \frac{C_b/E_b}{C_\ell/E_\ell}$ then

$$\begin{aligned} 0 = (1 - C) &- \sin\theta_\nu \cos\phi_\nu (\beta_{bx} - C\beta_{\ell x}) \\ &- \sin\theta_\nu \sin\phi_\nu (\beta_{by} - C\beta_{\ell y}) - \cos\phi_\nu (\beta_{bz} - C\beta_{\ell z}). \end{aligned} \tag{A.7}$$

Define p_0, p_1 and p_2 as the following

$$\begin{aligned} p_0 &= \sin^2\theta_\nu ((\beta_{bx} - C\beta_{\ell x})^2 + (\beta_{by} - C\beta_{\ell y})^2), \\ p_1 &= 2\sin\theta_\nu (\beta_{bx} - C\beta_{\ell x})(\cos\theta_\nu (\beta_{bz} - C\beta_{\ell z}) + C - 1), \\ p_2 &= (\cos\theta_\nu (\beta_{bz} - C\beta_{\ell z}) + C - 1)^2 - \sin^2\theta_\nu (\beta_{by} - C\beta_{\ell y})^2. \end{aligned} \tag{A.8}$$

Then we can solve cosϕ_ν from quadratic equation

$$\cos^2\phi_\nu p_0 + \cos\phi_\nu p_1 + p_2 = 0. \tag{A.9}$$

The neutrino energy E_ν can be derived from Eq. A.4 as

$$E_\nu = \frac{C_b/E_b}{1 - \beta_{bx}\sin\theta_\nu\cos\phi_\nu - \beta_{by}\sin\theta_\nu\sin\phi_\nu - \beta_{bz}\cos\theta_\nu}. \tag{A.10}$$

Appendix B

Optimization of event selection in the *ee* and $\mu\mu$ channels

Tables of expected statistical uncertainties for different $\not\!\!E_T$ and $\not\!\!E_T$ significance cuts in the *ee* and $\mu\mu$ channels. Each table is associated with one tested maxMVA cut.

B.1. *ee*

Table B.1: Expected statistical uncertainty (GeV) with 172.5 GeV input $m_{\rm t}$ for different $\not\!\!E_T$ cuts in Z mass window and $\not\!\!E_T$ significance cuts and maxMVA cut at 0.02 in the *ee* channel.

$\not\!\!E_T/\not\!\!E_T$ sig.	3.5	4	4.5	5	5.5
20	3.49	3.56	3.44	3.47	3.38
30	3.38	3.32	3.37	3.41	3.36
40	3.23	3.28	3.34	3.34	3.34
50	3.26	3.33	3.38	3.45	3.43
60	3.33	3.44	3.48	3.53	3.52

Table B.2: Expected statistical uncertainty (GeV) with 172.5 GeV input m_t for different $\not{E}_T$ cuts in Z mass window and $\not{E}_T$ significance cuts and maxMVA cut at 0.03 in the *ee* channel.

$\not{E}_T/\not{E}_T$ sig.	3.5	4	4.5	5	5.5
20	3.45	3.44	3.41	3.42	3.44
30	3.32	3.29	3.35	3.37	3.37
40	3.24	3.29	3.32	3.43	3.35
50	3.30	3.32	3.43	3.50	3.49
60	3.39	3.42	3.52	3.58	3.53

Table B.3: Expected statistical uncertainty (GeV) with 172.5 GeV input m_t for different $\not{E}_T$ cuts in Z mass window and $\not{E}_T$ significance cuts and maxMVA cut at 0.04 in the *ee* channel.

$\not{E}_T/\not{E}_T$ sig.	3.5	4	4.5	5	5.5
20	3.40	3.41	3.38	3.43	3.39
30	3.31	3.32	3.39	3.41	3.33
40	3.23	3.28	3.34	3.35	3.36
50	3.32	3.33	3.46	3.44	3.45
60	3.41	3.46	3.50	3.55	3.56

Table B.4: Expected statistical uncertainty (GeV) with 172.5 GeV input m_t for different $\not{E}_T$ cuts in Z mass window and $\not{E}_T$ significance cuts and maxMVA cut at 0.05 in the *ee* channel.

$\not{E}_T/\not{E}_T$ sig.	3.5	4	4.5	5	5.5
20	3.37	3.38	3.37	3.39	3.37
30	3.29	3.25	3.29	3.40	3.31
40	3.19	3.26	3.30	3.32	3.35
50	3.25	3.31	3.39	3.41	3.41
60	3.36	3.40	3.50	3.51	3.51

Table B.5: Expected statistical uncertainty (GeV) with 172.5 GeV input m_{t} for different $\not\!\!E_T$ cuts in Z mass window and $\not\!\!E_T$ significance cuts and maxMVA cut at 0.06 in the *ee* channel.

$\not\!\!E_T/\not\!\!E_T$ sig.	3.5	4	4.5	5	5.5
20	3.34	3.38	3.35	3.35	3.31
30	3.30	3.30	3.34	3.40	3.32
40	3.19	3.23	3.28	3.30	3.31
50	3.26	3.34	3.39	3.41	3.41
60	3.39	3.45	3.51	3.51	3.51

Table B.6: Expected statistical uncertainty (GeV) with 172.5 GeV input m_{t} for different $\not\!\!E_T$ cuts in Z mass window and $\not\!\!E_T$ significance cuts and maxMVA cut at 0.07 in the *ee* channel.

$\not\!\!E_T/\not\!\!E_T$ sig.	3.5	4	4.5	5	5.5
20	3.39	3.41	3.38	3.44	3.34
30	3.30	3.31	3.35	3.40	3.35
40	3.22	3.24	3.25	3.34	3.29
50	3.25	3.32	3.39	3.45	3.46
60	3.38	3.44	3.53	3.53	3.53

Table B.7: Expected statistical uncertainty (GeV) with 172.5 GeV input $m_{\rm t}$ for different $\not\!\!E_T$ cuts in Z mass window and $\not\!\!E_T$ significance cuts and maxMVA cut at 0.08 in the ee channel.

$\not\!\!E_T/\not\!\!E_T$ sig.	3.5	4	4.5	5	5.5
20	3.40	3.39	3.41	3.45	3.40
30	3.30	3.37	3.36	3.41	3.37
40	3.22	3.29	3.30	3.34	3.37
50	3.25	3.35	3.44	3.51	3.46
60	3.39	3.47	3.56	3.58	3.56

B.2. $\mu\mu$

Table B.8: Expected statistical uncertainty (GeV) with 172.5 GeV input m_{t} for different $\not\!\!E_T$ cuts and $\not\!\!E_T$ significance cuts and maxMVA cut at 0.02 in the $\mu\mu$ channel.

$\not\!\!E_T/\not\!\!E_T$ sig.	2	3	4	5	6	7	8
20	4.42	4.01	3.83	3.75	3.73	3.83	4.00
30	4.14	3.91	3.78	3.74	3.70	3.85	4.00
40	3.85	3.73	3.68	3.67	3.63	3.90	4.03
50	3.77	3.78	3.75	3.76	3.76	3.93	4.01
60	3.86	3.85	3.89	3.92	3.94	4.07	4.09

Table B.9: Expected statistical uncertainty (GeV) with 172.5 GeV input m_{t} for different $\not\!\!E_T$ cuts and $\not\!\!E_T$ significance cuts and maxMVA cut at 0.03 in the $\mu\mu$ channel.

$\not\!\!E_T/\not\!\!E_T$ sig.	2	3	4	5	6	7	8
20	4.24	3.82	3.67	3.71	3.65	3.86	4.02
30	4.00	3.78	3.64	3.71	3.63	3.87	4.05
40	3.64	3.66	3.61	3.64	3.64	3.88	4.07
50	3.70	3.69	3.74	3.76	3.73	3.90	4.02
60	3.81	3.85	3.87	3.96	3.95	4.04	4.09

Table B.10: Expected statistical uncertainty (GeV) with 172.5 GeV input $m_{\rm t}$ for different $\not\!\!E_T$ cuts and $\not\!\!E_T$ significance cuts and maxMVA cut at 0.04 in the $\mu\mu$ channel.

$\not\!\!E_T/\not\!\!E_T$ sig.	2	3	4	5	6	7	8
20	4.21	3.84	3.64	3.66	3.63	3.87	3.97
30	3.87	3.71	3.61	3.63	3.66	3.89	4.00
40	3.66	3.63	3.59	3.64	3.66	3.87	3.98
50	3.57	3.61	3.67	3.73	3.72	3.88	3.98
60	3.78	3.72	3.87	3.89	3.92	3.99	4.05

Table B.11: Expected statistical uncertainty (GeV) with 172.5 GeV input $m_{\rm t}$ for different $\not\!\!E_T$ cuts and $\not\!\!E_T$ significance cuts and maxMVA cut at 0.05 in the $\mu\mu$ channel.

$\not\!\!E_T/\not\!\!E_T$ sig.	2	3	4	5	6	7	8
20	4.15	3.87	3.64	3.67	3.62	3.78	3.90
30	3.85	3.73	3.60	3.58	3.63	3.85	3.90
40	3.61	3.57	3.58	3.56	3.56	3.87	3.91
50	3.54	3.57	3.66	3.64	3.69	3.85	3.93
60	3.73	3.70	3.78	3.84	3.89	3.99	4.02

Table B.12: Expected statistical uncertainty (GeV) with 172.5 GeV input m_{t} for different $\not{E}_T$ cuts and $\not{E}_T$ significance cuts and maxMVA cut at 0.06 in the $\mu\mu$ channel.

$\not{E}_T/\not{E}_T$ sig.	2	3	4	5	6	7	8
20	4.10	3.83	3.71	3.72	3.74	3.97	3.95
30	3.87	3.74	3.61	3.73	3.74	3.93	3.99
40	3.67	3.63	3.63	3.64	3.72	3.80	3.97
50	3.63	3.64	3.68	3.78	3.70	3.93	4.00
60	3.79	3.77	3.90	3.98	3.99	4.03	4.08

Table B.13: Expected statistical uncertainty (GeV) with 172.5 GeV input m_{t} for different $\not{E}_T$ cuts and $\not{E}_T$ significance cuts and maxMVA cut at 0.07 in the $\mu\mu$ channel.

$\not{E}_T/\not{E}_T$ sig.	2	3	4	5	6	7	8
20	4.17	3.80	3.72	3.73	3.75	3.94	4.04
30	3.90	3.73	3.62	3.68	3.76	3.92	4.04
40	3.64	3.63	3.63	3.64	3.69	3.89	4.00
50	3.64	3.66	3.71	3.81	3.73	3.95	4.00
60	3.86	3.80	3.91	3.93	3.99	4.09	4.08

Table B.14: Expected statistical uncertainty (GeV) with 172.5 GeV input m_{t} for different $\not\!\!E_T$ cuts and $\not\!\!E_T$ significance cuts and maxMVA cut at 0.08 in the $\mu\mu$ channel.

$\not\!\!E_T/\not\!\!E_T$ sig.	2	3	4	5	6	7	8
20	4.02	3.68	3.69	3.69	3.71	3.91	3.95
30	3.82	3.67	3.61	3.71	3.71	3.88	3.96
40	3.55	3.51	3.60	3.65	3.67	3.84	3.91
50	3.61	3.63	3.71	3.72	3.72	3.93	3.97
60	3.81	3.83	3.90	3.88	3.94	4.11	4.10

REFERENCES

[1] S. Abachi *et al.* [D0 Collaboration], “Observation of the top quark,” Phys. Rev. Lett. **74**, 2632 (1995).

[2] F. Abe *et al.* [CDF Collaboration], “Observation of top quark production in $\bar{p}p$ collisions,” Phys. Rev. Lett. **74**, 2626 (1995).

[3] S. Weinberg, “A Model of Leptons,” Phys. Rev. Lett. **19**, 1264 (1967).

[4] A. Salam, “Elementary Particle Theory,” edited by N. Svarthholm (Almqvist, forlag AB, Stockholm, 1968), p. 367.

[5] S. Chatrchyan *et al.* [CMS Collaboration], “Observation of a new boson at a mass of 125 GeV with the CMS experiment at the LHC,” Phys. Lett. B **716**, 30 (2012).

[6] G. Aad *et al.* [ATLAS Collaboration], “Observation of a new particle in the search for the Standard Model Higgs boson with the ATLAS detector at the LHC,” Phys. Lett. B **716**, 1 (2012).

[7] R. K. Ellis,W. J. Stirling, B. R.Webber, “QCD and collider physics,” Cambridge Univ. Press (2003).

[8] [ALEPH and CDF and D0 and DELPHI and L3 and OPAL and SLD and LEP Electroweak Working Group and Tevatron Electroweak Working Group and SLD Electroweak and Heavy Flavour Groups Collaborations], “Precision Electroweak Measurements and Constraints on the Standard Model” (2010).

[9] [ALEPH and DELPHI and L3 and OPAL and SLD and LEP Electroweak Working Group and SLD Electroweak Group and SLD Heavy Flavour Group Collaborations], “Precision electroweak measurements on the Z resonance,” Phys. Rept. **427**, 257 (2006).

[10] P. J. Mohr, B. N. Taylor and D. B. Newell, “CODATA Recommended Values of the Fundamental Physical Constants: 2006,” Rev. Mod. Phys. **80**, 633 (2008).

[11] W. J. Marciano, “Precision electroweak measurements and the Higgs mass,” eConf C **040802**, L009 (2004).

[12] V. M. Abazov *et al.* [D0 Collaboration], “Experimental discrimination between charge 2e/3 top quark and charge 4e/3 exotic quark production scenarios,” Phys. Rev. Lett. **98**, 041801 (2007).

[13] V. M. Abazov *et al.* [D0 Collaboration], “An Improved determination of the width of the top quark,” Phys. Rev. D **85**, 091104 (2012).

[14] T. E. W. Group [CDF and D0 Collaboration], “Combination of CDF and DØ results on the mass of the top quark using up to 9.7 fb^{-1} at the Tevatron” arXiv:1407.2682 [hep-ex].

[15] N. Kidonakis and R. Vogt, “The Theoretical top quark cross section at the Tevatron and the LHC,” Phys. Rev. D **78**, 074005 (2008).

[16] M. Cacciari, S. Frixione, M. L. Mangano, P. Nason and G. Ridolfi, “Updated predictions for the total production cross sections of top and of heavier quark pairs at the Tevatron and at the LHC,” JHEP **0809**, 127 (2008).

[17] D. Choudhury, R. Godbole, R. Singh, K. Wagh, “Top production at the Tevatron/LHC and nonstandard, strongly interacting spin one particles,” Phys. Lett. B **657**, 69 (2007).

[18] V. M. Abazov *et al.* [D0 Collaboration], “Evidence for production of single top quarks,” Phys. Rev. D **78**, 012005 (2008).

[19] S. Eidelman *et al.* [Particle Data Group Collaboration], “Review of particle physics. Particle Data Group,” Phys. Lett. B **592**, 1 (2004).

[20] RunII Handbook. Fermilab Beams Division, March 2001. `http://www-bd.fnal.gov/runII/index.html`

[21] C. Schmidt and C. Curtis, ”A 50-mA Negative Hydrogen-Ion Source”, IEEE Transactions on Nuclear Science, **NS-26**, 4120 (1979).

[22] C. Curtis *et al.*, ”Linac H-Beam Operation and Uses at Fermilab”, IEEE Transactions on Nuclear Science, **NS-26**, 3760 (1979).

[23] E. Hubbard *et al.*, ”Booster synchrotron”, Fermilab Technical Report Fermilab TM-405, (1973).

[24] C. S. Mishra, “The Fermilab main injector”, In the Proceedings of Particles & Fields 92: 7th Meeting of the Division of Particles Fields of the APS (DPF 92), Batavia, Illinois, 10-14 Nov 1992, pp 1619-1621 (1992).

[25] A. Ruggiero, "The Fermilab Tevatron I Debuncher Ring", IEEE Transactions on Nuclear Science, **NS-30**, 2478 (1983).

[26] J. Griffin *et al.*, "Time and Momentum Exchange for Production and Collection of Intense Antiproton Beams at Fermilab", IEEE Transactions on Nuclear Science, **NS-30**, 2630 (1983).

[27] A. Ando, T. Collins and D. Johnson, "Design of an 8-GeV Accumulator Ring For the Fermilab Tevatron I Project", IEEE Transactions on Nuclear Science, **NS-30**, 2031 (1983).

[28] D. Mohl, G. Petrucci, L. Thorndahl and S. Van Der Meer, "Physics And Technique Of Stochastic Cooling", Phys. Rept. **58**, 73 (1980).

[29] G. Jackson, "Recycler ring conceptual design report", FERMILAB-TM-1936.

[30] Group, TeVI, "Design Report Tevatron 1 project", FERMILAB-DESIGN-1984-01

[31] S. Abachi *et al.* [D0 Collaboration], "The D0 Detector", Nucl. Instrum. Meth. A **338**, 185 (1994).

[32] V. M. Abazov *et al.* [D0 Collaboration], "The Upgraded D0 Detector", Nucl. Instrum. Meth. A **565**, 463 (2006).

[33] J. Brzezniak *et al.*, "Conceptual Design Of A 2-Tesla Superconducting Solenoid For The Fermilab D0 Detector Upgrade", FERMILAB-TM-1886;

[34] B. S. Acharya *et al.* [D0 Collaboration], "Scintillation counters for the D0 muon upgrade," Nucl. Instrum. Meth. A **401**, 45 (1997).

[35] Type 404A plastic scintillator, Bicron Corporation, 12345 Kinsman Rd, Newbury, OH 44065-9677.

[36] The D0 Algorithms Group. `http://www-d0.fnal.gov/computing/algorithms/index.html`

[37] The D0 Common Sample Group. `http://www-d0.fnal.gov/Run2Physics/cs/index.html`

[38] Trigger Modeling for RunIIb. `https://plone4.fnal.gov/P1/D0Wiki/tdaq/tsg/triggerrun2b/`

[39] The DØ TriggerMeisters' page. `http://www-d0online.fnal.gov/www/groups/tm/tm_main.html`

[40] M.L. Mangano, M. Moretti, F. Piccinini, R. Pittau, A.D. Polosa, J. High Energy Phys. 0307 (2003) 001.

[41] T. Sjöstrand, S. Mrenna, P.Z. Skands, J. High Energy Phys. 0605 (2006) 026.

[42] G. Corcella *et al.*, "HERWIG 6.5: an event generator for Hadron Emission Reactions With Interfering Gluons (including supersymmetric processes)," JHEP **0101**, 010 (2001).

[43] B. Andersson, G. Gustafson, G. Ingelman and T. Sjostrand, "Parton Fragmentation And String Dynamics," Phys. Rept. **97**, 31 (1983).

[44] B. R. Webber, "A QCD Model For Jet Fragmentation Including Soft Gluon Interference," Nucl. Phys. B **238**, 492 (1984).

[45] S. Höche et al., "Matching Parton Showers and Matrix Elements," hep-ph/0602031.

[46] J. Pumplin et al., J. High Energy Phys **207**, 012 (2002).

[47] R. Brun, F. Carminati, CERN Program Library Long Writeup W5013, 1993 (unpublished)

[48] G. Borissov, "Ordering a Chaos or ... Technical Details of AA Tracking", presented at All DØ meeting, Feb. 28, 2003. `http://wwwd0.fnal.gov/atwork/adm/d0_private/2003-02-28/adm_talk.ps`

[49] R. Duda, P. Hart, "Use of the Hough transformation to detect lines and curves in pictures", Communications of the ACM **15**, 11 1972.

[50] A. Khanov, "HTF: histogramming method for finding tracks. The algorithm description", D0 Note 3778.

[51] A. Schwartzman, C. Tully, "Primary vertex reconstruction by means of adaptive vertex fitting", D0 Note 4918.

[52] R. Fruhwirth, "Application Of Kalman Filtering To Track And Vertex Fitting," Nucl. Instrum. Meth. A **262**, 444 (1987).

[53] A. Schwartzman, M. Narain, "Probabilistic Primary Vertex Selection," D0 Note 4042.

[54] A. Schwartzman, M. Narain, "Secondary Vertex Reconstruction using the Kalman Filter," DØ note 3908.

[55] A. Schwartzman, M. Narain, "Secondary b tagging using the Kalman Filter Algorithm," DØ note 3909.

[56] A. Schwartzman, M. Narain, "*b* quark jet identification via Secondary Vertex Reconstruction," DØ note 4080.

[57] I. Anghel, C. Gerber, E. Shabalina, T. Ten, "Studies of Taggabilty versus number of Primary Vertices for p17 data," DØ note 5240.

[58] Y. Peters, H. Greenlee, A. Haas, A. Schwartzman, "Optimization of the Secondary Vertex Tagger in p17," DØ note 5265.

[59] A. Abdesselam, "Comparison of H-Matrices for electron identification in D0 Run II", D0 Note 3745.

[60] M. Aoki, "Electron Likelihood in p20", D0 Note 5675.

[61] V. M. Abazov [D0 Collaboration], "Electron and Photon Identification in the DØ Experiment," Nucl. Instrum. Methods A **750**, 78 (2014).

[62] V. M. Abazov [D0 Collaboration], "Muon reconstruction and identification with the Run II DØ detector" Nucl. Instrum. Methods A **737**, 281 (2014).

[63] G. Blazey *et al.*, "Run II Jet Physics", D0 Note 3750.

[64] E. Busato, B. Andrieu, "Jet Algorithms in D0 RunII Software: Description and User's Guide", D0 Note 4457.

[65] G. Bernardi *et al.*, "Improvements from the T42 Algorithm on Calorimeter Objects Reconstruction", D0 Note 4335.

[66] A. Harel *et al.*, "Jet ID optimization", D0 Note 4919.

[67] A. Harel, R. Wagner "Improved L1 Confirmation", D0 Note 4932.

[68] S. Calvet *et al.*, "Towards MissingET Certification and Unclustered Energy Studies", D0 Note 4927.

[69] V. M. Abazov [D0 Collaboration], "Improved *b* quark jet identification at the DØ experiment," Nucl. Instrum. Methods A **763**, 290 (2014).

[70] A. Hocker et al., "TMVA, the Toolkit for Multivariate Data Analysis with ROOT," PoS ACAT, 040 (2007).

[71] V. M. Abazov [D0 Collaboration], "Jet energy scale determination in the DØ experiment," Nucl. Instrum. Methods A **763**, 442 (2014).

[72] D. Gillberg *et al.*, "Measuring Jet Response Using the Missing Et Projection Fraction Method in photon+jet Events", D0 Note 4571 (2004).

[73] R. Kehoe, “Resolution Bias in Jet Response Measurement”, D0 Note 2052 (1994).

[74] R. Wigmans, “On The Energy Resolution Of Uranium And Other Hadron Calorimeters,” Nucl. Instrum. Meth. A **259**, 389 (1987).

[75] JES Group, “Jet Energy Scale Determination at D0 Run II (final p17 version)”, D0 Note 5382 (2007).

[76] Z. Ye *et al.*, “Correction for the MC-Data Difference in the Jet Response at D0”, D0 Note 6143 (2011).

[77] Z. Ye *et al.*, “Correction for the MC-Data Difference in the Jet Response at D0 for Run IIB”, D0 Note 6144 (2011).

[78] K. Augsten, Z. Ye, “Correction for the MC-Data Difference in the Jet Response at D0 for Run IIB,” D0 Note 6368 (2013).

[79] V. M. Abazov *et al.* [D0 Collaboration], “Precise measurement of the top-quark mass from lepton+jets events at D0,” Phys. Rev. D **84**, 032004 (2011)

[80] V. M. Abazov [D0 Collaboration], “Precision measurement of the top-quark mass in lepton+jets final states,” submitted to Phys. Rev. D, detailed documentation of Phys. Rev. Lett. **113**, 032002 (2014), arXiv:1501.07912 [hep-ex]

[81] V. M. Abazov [D0 Collaboration], “Precision measurement of the top quark mass in lepton+jets final states at DØ,” Phys. Rev. Lett. **113**, 032002 (2014).

[82] V. M. Abazov [D0 Collaboration], “Measurement of the Top Quark Mass in $p\bar{p}$ Collisions using Events with Two Leptons,” Phys. Rev. D **86**, 051103(R) (2012).

[83] P. Renkel, Y. Ilchenko, R. Kehoe, “Measuring the top quark mass in the dilepton channel with 5.3 fb^{-1}”, D0 Note 6187 (2011).

[84] E. Varnes, “Measurement of the Top Quark Mass”, FERMILAB-THESIS-1997-28;

[85] B. Abbott *et al.* [D0 Collaboration], “Measurement of the top quark mass using dilepton events. DØ Collaboration,” Phys. Rev. Lett. **80**, 2063 (1998).

[86] B. Abbott *et al.* [D0 Collaboration], “Measurement of the top quark mass in the dilepton channel,” Phys. Rev. D **60**, 052001 (1999).

[87] V. M. Abazov *et al.* [D0 Collaboration], “Direct measurement of the mass difference between top and antitop quarks,” Phys. Rev. D **84**, 052005 (2011).

[88] P. Renkel, Y. Ilchenko, R. Kehoe, "Measurement of the Top Quark Mass in $e\mu$ Final States with Neutrino Weighting in Run II at DØ," D0 Note 6104-CONF.

[89] V.M. Abazov *et al.* [D0 Collaboration], "Measurement of the top quark mass in final states with two leptons," Phys. Rev. D **80**, 092006 (2009).

[90] P. Renkel, *et al.* "Measurement of the Top Quark Mass in Dilepton Final States with Neutrino Weighting in Run II at DØ," D0 Note 6187.

[91] M. Mulders, "Ensemble testing for the Top Mass measurement", D0 Note 6144.

[92] R. J. Barlow, "Application of the Bootstrap resampling technique to Particle Physics experiments", perprint MAN-HEP-99-4 available at `http://www.hep.man.ac.uk/preprints/1999.html`

[93] F. Deliot *et al.*, "Systematic Uncertainties in Top Quark Measurements", D0 Note 6024.

[94] A. Abulencia *et al.* [CDF Collaboration], "Top quark mass measurement using the template method in the lepton + jets channel at CDF II," Phys. Rev. D **73**, 032003 (2006).

[95] P. Z. Skands and D. Wicke, "Non-perturbative QCD effects and the top mass at the Tevatron," Eur. Phys. J. C **52**, 133 (2007).

[96] P. Skands, "Tuning Monte Carlo generators: The Perugia tunes," Phys. Rev. D **82**, 074018 (2010), arXiv:1005.3457v4 (2011).

[97] S. Frixione , "Single-top hadroproduction in association with a W boson," J. High Energy Phys. **07**, 029 (2008).

[98] S. Frixione , "Single-top production in MC@NLO," J. High Energy Phys. **03**, 092 (2006).

[99] S. Frixione and B. Webber, " Matching NLO QCD computations and parton shower simulations," J. High Energy Phys. **06**, 029 (2002).

[100] M. G. Bowler, "e+ e- Production of Heavy Quarks in the String Model," Z. Phys. C **11**, 169 (1981).

[101] Y. Peters *et al.* [D0 Collaboration], "Precise tuning of the b fragmentation for the D0 Monte Carlo," FERMILAB-TM-2425-E.

[102] J. Pumplin, D. R. Stump, J. Huston, H. L. Lai, P. M. Nadolsky and W. K. Tung, "New generation of parton distributions with uncertainties from global QCD analysis," JHEP **0207**, 012 (2002).

[103] M. Arthaud *et al.*, “Muon Momentum Oversmearing for p20 Data”, D0 Note 5449.

[104] N. Makovec and J.-F. Grivaz, “Shifting, Smearing and Removing Simulated Jets”, D0 Note 4914.

[105] L. Lyons, D. Gibaut and P. Clifford, “How To Combine Correlated Estimates Of A Single Physical Quantity,” Nucl. Instrum. Meth. A **270**, 110 (1988).

[106] A. Valassi, “Combining correlated measurements of several different physical quantities,” Nucl. Instrum. Meth. A **500**, 391 (2003).

[107] [ATLAS and CDF and CMS and DØ Collaborations], “First combination of Tevatron and LHC measurements of the top-quark mass,” arXiv:1403.4427 (2014).